SYNTHESIS AND FUNCTIONALIZATION OF NANOSTRUCTURED ELECTRICALLY CONDUCTIVE FINE PARTICLE FOR ENERGY STORAGE AND CONVERSION

(エネルギー貯蔵･変換のための電気導電性ナノ構造体微粒子の合成と機能化)

By

ADITYA FARHAN ARIF

HIROSHIMA UNIVERSITY

SEPTEMBER 2017

SYNTHESIS AND FUNCTIONALIZATION OF NANOSTRUCTURED ELECTRICALLY CONDUCTIVE FINE PARTICLE FOR ENERGY STORAGE AND CONVERSION

(エネルギー貯蔵・変換のための電気導電性ナノ構造体微粒子の合成と機能化)

A Thesis submitted to
The Department of Chemical Engineering
Graduate School of Engineering
Hiroshima University

By

ADITYA FARHAN ARIF

In Partial Fulfillment of the Requirements
For the Degree of
Doctor of Engineering

Hiroshima University
September 2017

Approved by
Associate Professor Takashi Ogi
Advisor

Abstract

Fuel cells and supercapacitors emerge as alternative energy supplying devices in response to the problems related to the utilization of internal combustion engine: Fossil fuel shortage and environmental issue due to the emitted greenhouse gasses. To date, continuous improvement on these devices is still required to achieve high performance. Possible approaches for the improvement include functionalization and optimization on the electrode structure, which are commonly composed of carbon particles.

The research covered in the scope of this dissertation is aimed to investigate the structure of carbon particles suitable for the improved device's performance and their functionalization. Two methods were employed for the nanostructuration and functionalization, *i.e.* aerosol and liquid phase method. As a continuation of the carbon-related studies, this dissertation also investigates an alternative material for carbon substitute in response to the durability problem suffered by carbon. In detail, the contents of this dissertation is as the followings.

Chapter 1 summarizes the recent trend of carbon nanostructuration and functionalization, the opportunity for improvement towards highly functional carbon particles for fuel cells and supercapacitor, and the alternative material in response to the problem suffered by carbonaceous materials. This summary and problem statements lead to the motivation of the researches covered within the scope of this dissertation.

Chapter 2 discusses the effect of carbon particle morphology on the oxygen reduction reaction performance after being deposited with Pt nanoparticles. A dual polymer precursor, comprising phenolic resin and polystyrene latex (PSL), was used as the starting materials for the spray pyrolysis process. Phenolic resin to PSL ratios and PSL surface charge were varied to produce carbon particles with various morphology, i.e. dense, hollow, and porous. After Pt deposition, oxygen reduction reaction activity of the electrocatalyst was evaluated to obtain the optimum morphological structure to perform the reaction. It was found that a combination between meso- and macropores is important for a good oxygen reduction reaction activity. The results were confirmed using a computational fluid dynamic simulation.

Chapter 3 focuses on in-situ functionalization of hollow-structured carbon particles and its effects on the capacitance. 3-aminophenol was used as both nitrogen and carbon source. Polymerization of 3-aminophenol was assisted by microwave irradiation. Addition of PSL into the precursor created the hollow structure. The shell thickness was controlled by varying the

ratio between PSL and 3-aminophenol. A high nitrogen content, up to 15.62%, was observed in the synthesized hollow carbon. A combination of the nitrogen doping and hollow structure contributes to a capacitance of 16.3 F cm-3, higher than that of commercial activated carbon.

In **Chapter 4**, Magneli phases TiOx nanoparticles were synthesized from micron-sized TiO2 particles using thermal induced plasma method. The synthesized nanoparticles were heat-treated in a mildly reducing atmosphere at 550 °C for rearrangement of the crystal structure, resulting in the highly conductive TiOx nanoparticles despite comprising many TiOx phases. Durability of these nanoparticles was evaluated by performing 1000-cycle cyclic voltammetery and an accelerated corrosion test in hydrochloric acid solution. Results of this evaluation show a high stability and corrosion resistance in a strongly oxidizing environment. **Chapter 5** provides a summary of all chapters and suggestions for future research.

Contents

List of Tables

List of Figures

Chapter 1

Introduction

1.1 Electrochemical energy storage and conversion devices

The fossil fuel shortage issue and the worsening environmental problem due to the emission from internal combustion engine have led to the long pursuit for alternative energy supplying devices which are non-fossil fuel basis and environmentally friendly. The energy supplying devices working based on electrochemical process emerge as promising alternatives, mainly because of their high total efficiencies[1] and zero emittance of toxic effluent.[2] Of the electrochemistry-based energy supplying devices, fuel cells and supercapacitors have attracted notable interest in the recent decades.[3] As one of the indications, the publication number related to the advancement of these devices has been increasing within the period of 2012 to 2017. By the end of May 2017, Web of Science records about 33% increase of the publication number related to fuel cells and a 187% increase of those related to supercapacitors.

The attractiveness of these devices is on account of their versatility and a promising future. For example, fuel cells can accommodate several types of fuels and offer two options for the operating temperature, *i.e.* low temperature (approximately 70 °C) and high temperature (over 500 °C).[4] Supercapacitors, on the other hand, have a long lifecycle and are able to bridge the gap between dielectric capacitor and batteries.[5] It is also worth mentioning that fuel cells and supercapacitors can complement each other, especially for mobile application where the peak power is usually needed.[6]

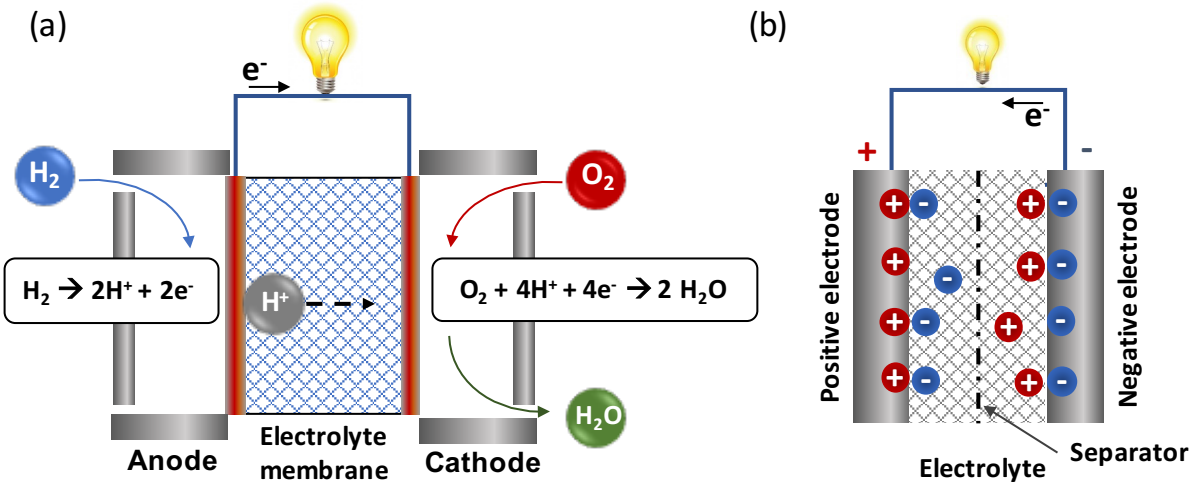

Figure 1.1 Representative scheme of (a) hydrogen fuel cell and (b) electrochemical double layer supercapacitor

Each device has its own designated function. Fuel cells are intended to be the main energy supplier as they generate electricity directly from the fuel through a set of electrochemical reactions in anode and cathode. A representative configuration of a fuel cell is depicted in **Figure 1.1(a)**. The fuel, usually hydrogen for low temperature fuel cells, enters the anode chamber to be oxidized through reaction (1). The electrons released from this reaction flow through the external electrical circuit to anode chamber. These electrons, together with protons transferred from the anode through electrolyte, are further used for the reduction of oxygen in the cathode (reaction (2)), resulting in a theoretical operating voltage of 1.23 V versus standard hydrogen electrode (SHE). These reactions happen repeatedly, causing a constant electron movement from anode to cathode, which in other words, generating constant current.

$$H_2 \rightarrow 2H^+ + 2e^- \qquad E^0 = 0\ \text{V/SHE} \qquad (1)$$

$$O_2 + 4H^+ + 4e^- \rightarrow 2H_2O \qquad E^0 = 1.23\ \text{V/SHE} \qquad (2)$$

Different from fuel cells, batteries and supercapacitors are designed for energy storage rather than energy generator. Characteristics in delivering the energy and power differentiate supercapacitors from batteries. As an inverse of batteries, supercapacitors normally deliver high power densities, implying that they are able to be rapidly charged and discharged at high current. This merit is particularly beneficial in the cases where instantaneous high power is required, for example during the acceleration of an electric vehicle. Their drawback is their low ability to store energy, *i.e.* low energy densities, as illustrated in the Ragone plot in **Figure 1.2**. This usually happens in supercapacitors that store energies in the electrochemical double layer, of which working principle is depicted in **Figure 1.1(b)**. Charging an electrochemical double layer supercapacitor will cause the protons and electrons in the electrolyte and electrodes to assemble oppositely. During the discharge, current flows from the positive to the negative electrode as the electrons move from the negative to the positive electrode. Because of this surface electrostatic charge storage mechanism, the energy storage capacity is limited by the surface area.[6]

Figure 1.2 clearly shows that none of the electrochemical energy supplying devices can match the characteristics of internal combustion engines in terms of their energy and power densities. This emphasizes the need for a continuous improvement in the performance of fuel cells and supercapacitors. So far, the improvement has been focused mainly on the development of the electrodes material.[7, 8] The concern is not only limited in the electrode

materials selection and functionalization, but also the morphological structure.[9, 10] A high surface area to volume ratio is known as the most general rule of thumb for high-performance electrodes. As a most common approach, nanoparticles are used for the electrodes to achieve high number of specific surface area. This approach is widely applied to fuel cells electrodes.

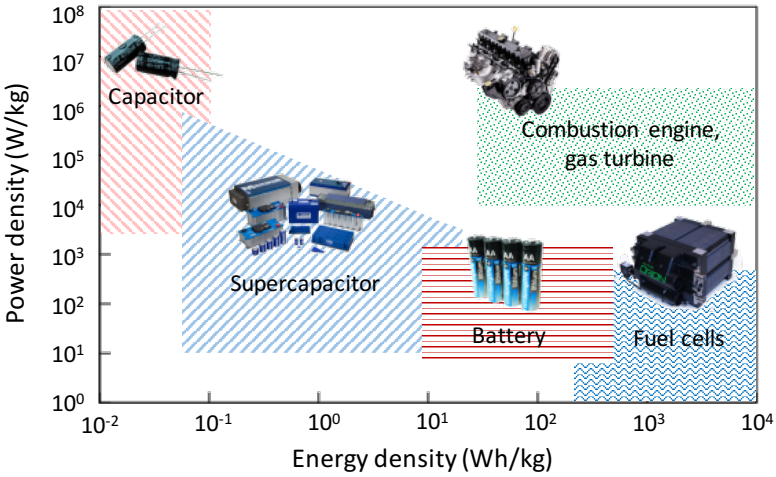

Figure 1.2. Ragone plot showing the energy storage domains of the electrochemical energy supplying devices compared to internal combustion engine and gas turbine. Adapted from Winter, et al.[2]

To add a double layer charge storage feature, nanoparticles or submicron particles with medium pore sizes (mesopores) are used in the supercapacitors. Although the preferred morphological structure of the electrodes can be different depending on the device, it is widely acknowledged that the electrode materials of fuel cells and supercapacitors should contain one or more electron-conducting species for good electron transfer.[9, 11] The electric current generated from the devices should be transferred to the external circuit without significant reduction by the Ohmic resistance of the materials.

1.2 Carbonaceous materials for fuel cells and supercapacitors electrodes

Carbon is nowadays the most popular electron-conducting material for fuel cells and supercapacitors, mainly due to its abundant stock, versatility, tunable morphology,[12] and modifiable surface functional group.[13] In fuel cells, carbon is used as electrocatalyst support. Platinum (Pt) supported on carbon (Pt/C) is by far the most effective electrocatalyst for fuel cells. Utilization of carbon reduces the required amount of platinum, hence lowering the total cost of the catalyst. It is a common knowledge that carbon as electrocatalyst support should be able to facilitate the formation of a good triple phase boundary. Consequently, morphological

structures suitable for the transport of reactant and electrolyte become essential to be evaluated. It is also worth mentioning that a good morphological structure of carbon support allows better Pt dispersion on the surface of carbon support, enabling higher electrocatalytic activity of Pt/C electrocatalyst. The drawback of the current Pt/C electrocatalyst is the poor Pt dispersion due to the non-optimized morphological structure of the carbon support. The suitable carbon particle morphology for an optimum Pt/C performance is yet to be investigated.

The role of carbon in supercapacitors is a little bit different. In addition to conducting the electrons, carbon also facilitates the charge storage within the pore structure which acts as an electrochemical double layer. The pore should be large enough for the electrolyte ions to penetrate, but small enough to obtain high surface area to volume ratio. Therefore, activated carbon which has a high conductivity and a combination between micro- and macropore has been used commercially for supercapacitor electrodes.

Despite having been used commercially as supercapacitor electrode, the charge stored in activated carbon – or in the double layer in general – is lower than that of other materials, such as metal oxides. The charge storage mechanism in metal oxides follow the principle of reduction-oxidation reaction. Discharge current is generated when metal oxides are reduced into the substoichiometric form, while charging is performed by oxidizing the substoichiometric metal oxides back into their stoichiometric form. Materials having this charge storage mechanism are called “pseudocapacitive”. In general, pseudocapacitance is higher than the electrochemical double layer capacitance. The drawback of pseudocapacitive charge storage is the cyclic durability. Nevertheless, pseudocapacitive charge storage mechanism can be added to carbon through surface functionalization. One of the popular approaches is by doping heteroatoms into carbon structure. Introduction of these atoms, for example nitrogen (N) or boron (B), allows similar charge mechanism to that found in metal oxides.

1.3 Carbon nanostructuration and functionalization strategies

1.3.1 Nanostructuration of carbon particles

Nanostructuration refers to the creation of structure in the intermediate between molecular and macroscopic scale. Nanostructuration of submicron particles is nowadays seen as a promising approach towards high performance particles while minimizing the disadvantages of nanoparticles, including difficulties in handling and potential health and environmental risk. Nanostructuration of carbon is commonly performed using two routes, *i.e.* aerosol route and liquid phase route.

1.3.1.1 Aerosol method

Aerosol method offers a rapid and controllable synthesis and nanostructuration of particles. The aerosol method allows scalable synthesis of functionalized, ultrafine particles with particular physical and chemical properties from molecular precursors.[14] Particles are produced by either a droplet-to-particle or a gas-to-particle conversion process. Spray drying is one of the droplet-to-particle methods for a wide range of applications, *e.g.* pharmaceuticals, foods, ceramics or catalysts.[15, 16] In spray drying, structured particles are produced from a particle suspension or a colloidal mixture. This precursor is atomized to form ultrafine droplets whose volumes are mostly occupied by solvent. The solvent is then evaporated by heating, causing the remaining components to precipitate after the mixture reaches a super-saturated state, as shown in **Figure 1.3(a)**. This whole process can be carried out in several seconds. The produced particles may exhibit a range of sizes and morphologies according to the characteristics of precursor, the size of the droplets and other operating conditions. Several works have been done in nanostructuring carbon and its composite using spray drying with carbon nanoparticles or flakes as the starting material.[17, 18] **Figures 1.4(a) to (c)** show several materials, including carbon, of which nanostructures are tailored by spray drying.

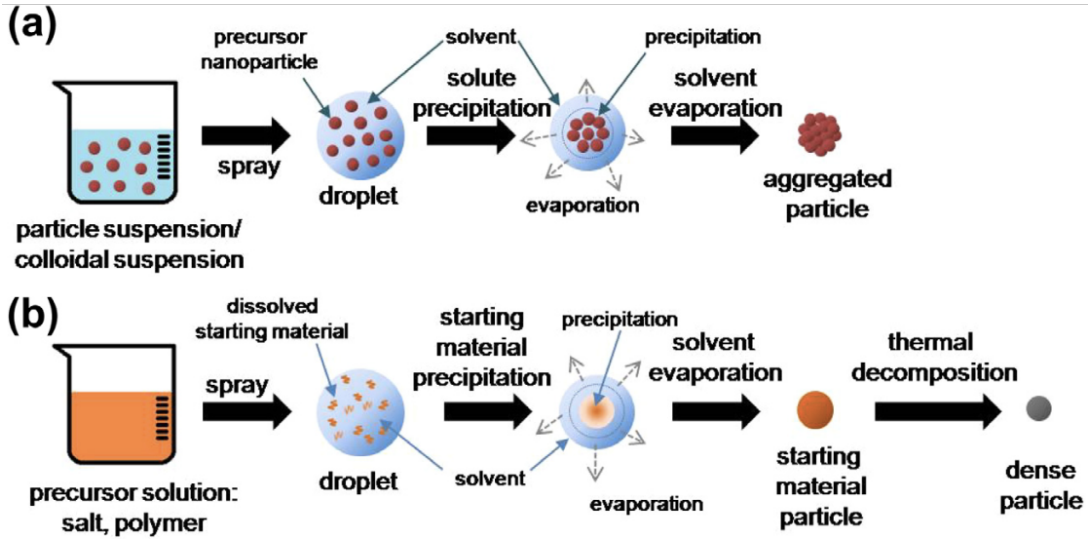

Figure 1.3. Illustration of particle formation in (a) spray drying and (b) spray pyrolysis. Reproduced from Arif, et al.[19]

Ultrafine particles with a narrow size-distribution and controllable morphology can also be synthesized by spray pyrolysis. Although the basic principle is similar to that for spray drying, the presence of chemical decomposition at elevated temperatures differentiates spray

pyrolysis, as illustrated in **Figure 1.3(b)**. Synthesis of nanostructured particles using spray pyrolysis is more flexible than using spray drying because of the wider range of precursor, for example polymer or salts. Phenolic resin is one of the polymers that have been efficaciously used for the synthesis of carbon particles using this method. Involvement of pyrolysis process also enables the synthesis of a wider range of morphology (**Figures 1.4(d) to (f)**).

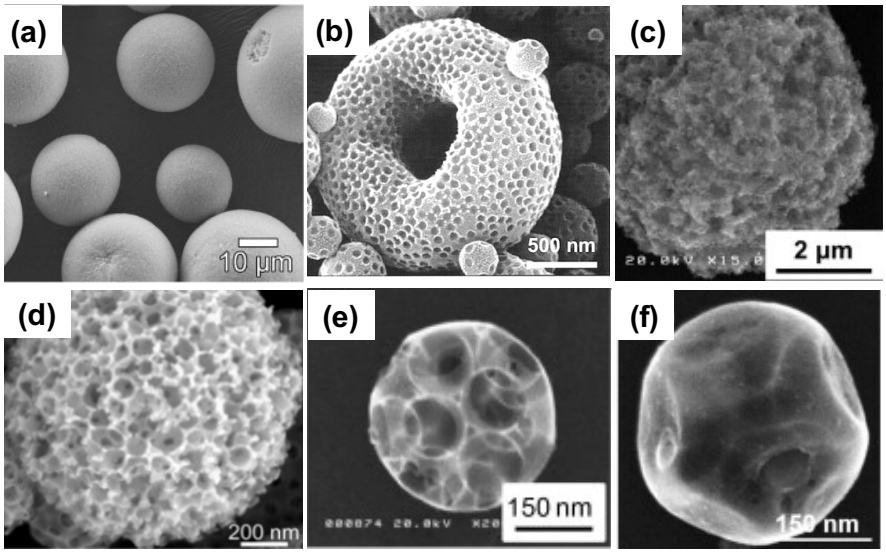

Figure 1.4. Various nanostructures prepared by spray drying: (a) dense titanate[20], (b) doughnut SiO_2 [21], and (c) carbon aggregates[17]. A wider range of the tailored morphology is provided by spray pyrolysis: (d) mesoporous MoS_2[22], (e) macroporous carbon[19], and (f) hollow carbon[23].

Both spray drying and spray pyrolysis are able to synthesize porous carbon particles by involving template.[17, 24] Salts[25] and metal oxides such as silica[22] are the common templates for the pore formation that have been proven to be effective. The shortcoming of these templates is the requirement for post-synthesis treatment for template removal. Especially for metal oxides, this removal involves strong acids such as hydrogen fluoride. Some researchers also investigate the opportunity of creating nanostructures in the absence of template. In such case, the pore is generated from the gasses released during precursor decomposition.[26] However, the pore formed using template-free method is usually limited to micro- and mesopores. Another approach to synthesize particles with hierarchical porous structure is using thermally decomposing template. Several particles with hierarchical porous structure were synthesized using polystyrene latex (PSL) template which decomposes at approximately 400 °C.[27-29] PSL has previously been used for a controlled nanostructuration of carbon particles from phenolic resin.[23] This method is promising to be further developed,

especially in the aim to observe the effect of fuel cells electrocatalyst support's morphology on the electrocatalyst activity.

1.3.1.2. Liquid phase method

Liquid phase method has been very popular for the synthesis of various types of nanoparticle, including metals[30, 31], metal oxide[32, 33], and carbon.[34, 35] Most of the liquid phase synthesis route uses hydrothermal process. In principle, hydrothermal synthesis process applies high pressure and high temperature to the precursor solution confined in a hydrothermal reactor. In the discourse of the synthesis of carbon particles, hydrothermal process is very effective in making monodisperse particles from various precursors.[36-38] The drawback of this process is the extensive synthesis time. In response to this problem, some researchers evaluate the effectiveness of microwave-assisted hydrothermal process to accelerate the synthesis time without downgrading the particle quality. The homogeneous and specific heating induced by microwave irradiation has been proven effective to shorten the reaction time in the one-pot synthesis of various metal[39-41], metal oxide[42, 43], and polymer nanoparticles.[44, 45] In the carbon particle synthesis, microwave-assisted hydrothermal process may be beneficial particularly when the synthesis starts from polymerization of carbon precursor monomer. This meticulous concern is yet to be investigated.

1.3.2 Functionalization of carbon particles

Particles functionalization refers to a process to tune the particle properties or to add a minor component in order to add certain functions or characteristics. Specific for fuel cells electrocatalyst and supercapacitors, functionalization of carbon particles usually focuses on the deposition of Pt nanoparticles and insertion or doping of nitrogen atoms, respectively. As mentioned earlier, Pt is the essential part of the fuel cell's electrocatalyst. Meanwhile, doping nitrogen atoms into the carbon structure gives an additional charge storage mechanism which is based on redox reactions, *i.e.* pseudocapacitive effect, which is usually found in metal oxides-based supercapacitors. The presence of free electrons in the doped nitrogen atom, especially in the pyridinic- and pyrrolic-type nitrogen, induces electron transfers between the electrode and the electrolyte which ressemble redox reactions. Therefore, doping nitrogen atoms into carbon is expected to improve the capacitance without the need of adding metal oxides into the electrode.

In general, functionalization of carbon particles can be performed either *ex-situ* or *in-situ*. The *ex-situ* functionalization method is a two-step process, consisting of the synthesis of

carbon particles and a subsequent functionalization. In the *in-situ* functionalization, the functions to be added f have been incorporated in the precursor. The latter method reduces the number of the synthesis step, but its effectiveness depends on the functionalization type.

Deposition of Pt nanoparticles is usually performed *ex-situ* by reduction of platinum precursor, for example chloroplatinic acid (H_2PtCl_6), using reducing agent such as sodium borohydride.[17, 46] Other Pt nanoparticles deposition methods are described in **Table 1.1**. Having been proven effective, most of these methods either employ dangerous reducing agent (*e.g.* pure H_2) or are time-extensive. A good approach to deposit Pt nanoparticles was recently introduced by Arutanti, et al., who used flame spray pyrolysis for *in-situ* Pt deposition on WO_3 particles. Although this method is extremely rapid and simple, some of Pt nanoparticles were trapped inside the structure of WO_3. While this is acceptable in the applications that use Pt as an electron trap, *e.g.* photocatalysis, it is unfavorable in the fields of electrocatalysis. Another improvement from the time-extensive methods for Pt deposition is the employment of microwave irradiation to accelerate the reduction of Pt ions and to reduce the required reduction temperature.[41, 47]

Table 1.1. Examples of the common Pt deposition method

No	Pt deposition method	Reference
1	Impregnation, Gas phase reduction by pure H_2 at 200 to 500 °C	[48, 49]
2	Precipitation, Chemical reduction by KBH_4 for 2 hours	[48]
3	Atomic layer deposition	[50]
4	In situ, flame spray pyrolysis of H_2PtCl_6	[51]
5	Evaporation-crystallization after 5-10 hours immersion in H_2PtCl_6	[49]

Doping of nitrogen atoms into carbon particle structure can be performed either *ex-situ* or *in-situ*. In the *ex-situ* method, carbon is exposed to a nitrogen source, usually ammonia (NH_3). NH_3 dissociates into nitrogen and hydrogen with some nitrogen radicals as intermediate. These radicals are small enough to penetrate carbon structure and create bonds with carbon atoms. However, this method requires high temperature to enable the dissociation of NH_3.[52] Another drawback is the instability of the bonds between nitrogen and carbon because this doping method results in the graphitic-type nitrogen with low binding energy.

While *ex-situ* doping requires an additional step after the carbon synthesis, *in-situ* doping offers simple one-step doping along with carbon synthesis. In principle, incorporation of nitrogen atoms is done by selecting nitrogen-containing compounds as carbon precursor, for example polyaniline[53, 54], melamine[55, 56], and 3-aminophenol[37]. The advantages of *in-situ* doping are the synthesis simplicity and the opportunity to control the type of nitrogen functional group in the synthesized carbon particle. As previously mentioned, pyridinic- and pyrrolic-type nitrogen are preferred to induce the pseudocapacitive charge storage.

1.4 Beyond carbon

Having demonstrated excellent performance and versatility as electrical-conducting material carbon is still facing a durability issue. From the electrochemical thermodynamic point of view, oxidation of carbon (also referred to as carbon corrosion) is possible at a standard potential, E^0, of 0.207 V vs. SHE. Indeed, this value is within the operational voltage of fuel cells' cathode according to reaction (2) and the charge-discharge voltage of supercapacitors. Although the carbon oxidation reaction is thermodynamically possible at 0.207 V vs. SHE (reaction (3)), the kinetic rate is sluggish up to approximately 1 V vs. SHE.[57, 58] This implies that carbon is oxidized at a slow rate during the normal operation of fuel cells and supercapacitors.

$$C + 2H_2O \rightarrow CO_2 + 4H^+ + 4e^- \qquad E^0 = 0.207\ \text{V/SHE} \qquad (3)$$

The oxidation rate of carbon in fuel cells, however, escalates significantly under H_2 starvation. This circumstance occurs in the start-stop of fuel cells and blockage of the anode by condensed water. In the usual state where H_2 and O_2 fills the anode and cathode, respectively, reaction (1) and (2) takes place in the respective chamber. In the event of H_2 starvation, reaction (2) takes place in anode. To get the protons, reaction (2) induces reaction (3) and oxygen evolution reaction (reaction (4)).

$$2H_2O \rightarrow O_2 + 4H^+ + 4e^- \qquad E^0 = 1.23\ \text{V/SHE} \qquad (4)$$

This mechanism is widely accepted and has been proven experimentally.[59-61] The actual potential during this circumstance can reach up to 1.4 V vs. reversible hydrogen electrode[61] or 1.75 vs. internal reference electrode.[62] At these potentials, oxidation of carbon becomes rapid and followed by Pt growth and dissolution.

In response to carbon corrosion problem, several studies have been conducted to strengthen the structure of the support. One of the approaches is using graphene instead of amorphous or graphitic carbon. The strong covalent bond between the C atoms in graphene provides an improvement in the durability.[63] Whereas having the highest durability, single

layer graphene is very difficult to make and to disperse, not to mention the difficulties in Pt immobilization on graphene surface. Utilization of graphene will not eliminate the risk of carbon corrosion from the thermodynamics point of view. Based on this viewpoint, some alternative non-carbonaceous materials have been investigated, such as TiN[64], TiO_2[65], SnO_2[66], and S-ZnO_2[67]. However, these materials have low electrical conductivity as their major drawback. This downside highly affects the performance by decreasing the electrochemical active surface area.

As the antithesis of the metal oxides, Magneli phases TiO_x demonstrate superior electrical conductivity up to the values comparable to that of graphite. Magneli phase TiO_x is a substoichiometric titanium oxide having a chemical structure of Ti_nO_{2n-1}. The oxygen deficiencies lead to a formation of crystallographic shear on (121) plane of rutile structure for the value of *n* between 3 and 10.[68] Compared to the stoichiometric rutile TiO_2, Magneli phases have narrow band gaps due to the delocalization of some electrons in *d* orbital, making them appropriate for visible-light absorption.[69] In light of this characteristic, Magneli phases TiO_x have been widely used for photocatalysis under visible light.[70, 71]

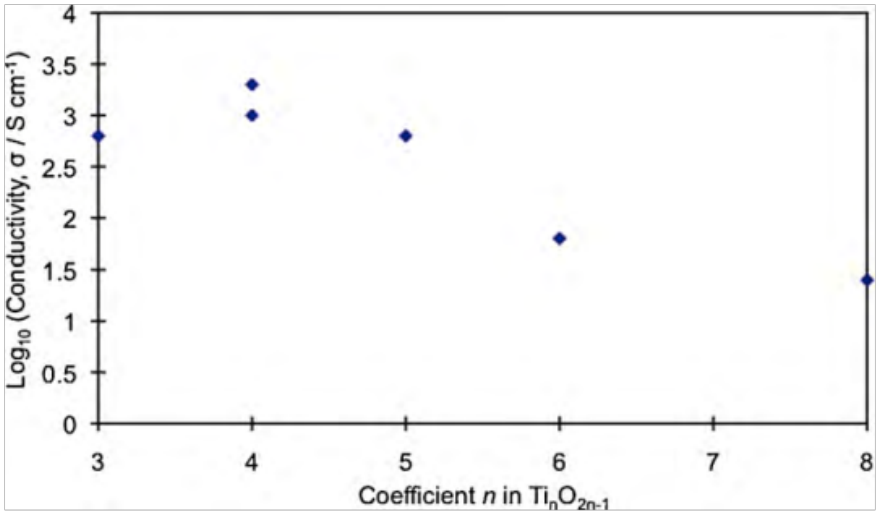

Figure 1.5. Summary of electron conductivity of Magneli phases TiO_x [72]

The formed crystallographic shear structure acts as a good electron pathway. This shear plane acts as an electron pathway. The electrical conductivity of this material depends on the value of *n*, as summarized in **Figure 1.5**. The electron mobility of Magneli phase TiO_x is reported to be as high as graphite with Ti_4O_7 as the most electrically conductive phase.[72] The conductivity of Ti_4O_7 is more than 1000 S cm^{-1}, which is even higher than that of graphitized carbon (727 S cm^{-1}).[73] In light of this, several investigations have been conducted to evaluate the possibility of using Magneli phase TiO_x as a replacement of carbon.[74-76] The challenge

for further improvement of this material is to synthesize nano-sized Magneli phase TiO_x without losing the benefit of its unusual crystallographic structure.

1.5 Objectives and outline of dissertation

This dissertation is intended to address the following objectives: (1) to improve the performance of carbon particle as electrocatalyst support and supercapacitor electrode through nanostructuration and functionalization by spray pyrolysis and microwave-assisted hydrothermal method and (2) to synthesize Magneli phases nanoparticles and to evaluate their electrochemical stability as a pathway towards their utilization as carbon substitutes. This dissertation comprises six chapters, of which content is described briefly as follows.

Chapter 1 summarizes the recent trend of carbon nanostructuration and functionalization, the opportunity for improvement towards highly functional carbon particles for fuel cells and supercapacitor, and the alternative material in response to the problem suffered by carbonaceous materials. This summary and problem statements lead to the motivation of the researches covered within the scope of this dissertation. **Chapter 2** discusses the effect of carbon particle morphology on the oxygen reduction reaction performance after being deposited with Pt nanoparticles. A dual polymer precursor, comprising phenolic resin and PSL, was used as the starting materials for the spray pyrolysis process. Phenolic resin to PSL ratios and PSL surface charge were varied to produce carbon particles with various morphology, *i.e.* dense, hollow, and porous. After Pt deposition, oxygen reduction reaction activity of the electrocatalyst was evaluated to obtain the optimum morphological structure to perform the reaction. It was found that a combination between meso- and macropores is important for a good oxygen reduction reaction activity. The results were confirmed using a computational fluid dynamic simulation.

In-situ functionalization of hollow-structured carbon particles and the effect of functionalization and nanostructuration on the capacitance is discussed in **Chapter 3**. 3-aminophenol was used as both nitrogen and carbon source. Polymerization of 3-aminophenol was assisted by microwave irradiation. Addition of PSL into the precursor created the hollow structure. The shell thickness was controlled by varying the ratio between PSL and 3-aminophenol. A high nitrogen content, up to 15.62%, was observed in the synthesized hollow carbon. A combination of the nitrogen doping and hollow structure contributes to a capacitance of 16.3 F cm^{-3}, higher than that of commercial activated carbon. In **Chapter 4**, Magneli phases TiO_x nanoparticles were synthesized from micron-sized TiO_2 particles using thermal induced plasma method. The synthesized nanoparticles were heat-treated in a mildly reducing

atmosphere at 550 °C for rearrangement of the crystal structure, resulting in the highly conductive TiO_x nanoparticles despite comprising many TiO_x phases. Durability of these nanoparticles was evaluated by performing 1000-cycle cyclic voltammetery and an accelerated corrosion test in hydrochloric acid solution. Results of this evaluation show a high stability and corrosion resistant in a strongly oxidizing environment. **Chapter 5** provides a summary of all chapters and insights for future research.

1.6 References

[1] Steele, B.C. and A. Heinzel, *Materials for fuel-cell technologies.* Nature, 2001. **414**(6861): p. 345-352.

[2] Winter, M. and R.J. Brodd, *What Are Batteries, Fuel Cells, and Supercapacitors?(Chem. Rev. 2003, 104, 4245− 4269. Published on the Web 09/28/2004.).* Chemical Reviews, 2005. **105**(3): p. 1021-1021.

[3] Salunkhe, R.R., et al., *Asymmetric supercapacitors using 3D nanoporous carbon and cobalt oxide electrodes synthesized from a single metal–organic framework.* ACS nano, 2015. **9**(6): p. 6288-6296.

[4] O'hayre, R., et al., *Fuel cell fundamentals*. 2016: John Wiley & Sons.

[5] Wang, G., L. Zhang, and J. Zhang, *A review of electrode materials for electrochemical supercapacitors.* Chemical Society Reviews, 2012. **41**(2): p. 797-828.

[6] Largeot, C., et al., *Relation between the ion size and pore size for an electric double-layer capacitor.* Journal of the American Chemical Society, 2008. **130**(9): p. 2730-2731.

[7] Kandalkar, S., et al., *Chemical synthesis of cobalt oxide thin film electrode for supercapacitor application.* Synthetic Metals, 2010. **160**(11): p. 1299-1302.

[8] Aricò, A.S., et al., *Nanostructured materials for advanced energy conversion and storage devices.* Nature materials, 2005. **4**(5): p. 366-377.

[9] Sharma, S. and B.G. Pollet, *Support materials for PEMFC and DMFC electrocatalysts—a review.* Journal of Power Sources, 2012. **208**: p. 96-119.

[10] Zhang, L.L. and X. Zhao, *Carbon-based materials as supercapacitor electrodes.* Chemical Society Reviews, 2009. **38**(9): p. 2520-2531.

[11] Zhi, M., et al., *Nanostructured carbon–metal oxide composite electrodes for supercapacitors: a review.* Nanoscale, 2013. **5**(1): p. 72-88.

[12] Bhattacharjya, D., et al., *High performance supercapacitor prepared from hollow mesoporous carbon capsules with hierarchical nanoarchitecture.* Journal of Power Sources, 2013. **244**: p. 799-805.

[13] Stein, A., Z. Wang, and M.A. Fierke, *Functionalization of porous carbon materials with designed pore architecture.* Advanced Materials, 2009. **21**(3): p. 265-293.

[14] Suh, W.H. and K.S. Suslick, *Magnetic and porous nanospheres from ultrasonic spray pyrolysis.* Journal of the American Chemical Society, 2005. **127**(34): p. 12007-12010.

[15] Ogi, T., A.B.D. Nandiyanto, and K. Okuyama, *Nanostructuring strategies in functional fine-particle synthesis towards resource and energy saving applications.* Advanced Powder Technology, 2014. **25**(1): p. 3-17.

[16] Vehring, R., W.R. Foss, and D. Lechuga-Ballesteros, *Particle formation in spray drying.* Journal of Aerosol Science, 2007. **38**(7): p. 728-746.

[17] Balgis, R., et al., *Ultrahigh oxygen reduction activity of Pt/nitrogen-doped porous carbon microspheres prepared via spray-drying.* Journal of Power Sources, 2013. **229**: p. 58-64.

[18] Li, M., et al., *Facile spray-drying/pyrolysis synthesis of core–shell structure graphite/silicon-porous carbon composite as a superior anode for Li-ion batteries.* Journal of Power Sources, 2014. **248**: p. 721-728.

[19] Arif, A.F., et al., *Experimental and theoretical approach to evaluation of nanostructured carbon particles derived from phenolic resin via spray pyrolysis.* Chemical Engineering Journal, 2015. **271**: p. 79-86.

[20] Faure, B., et al., *Spray drying of TiO2 nanoparticles into redispersible granules.* Powder Technology, 2010. **203**(2): p. 384-388.

[21] Iskandar, F., a. Mikrajuddin, and K. Okuyama, *In situ production of spherical silica particles containing self-organized mesopores.* Nano Letters, 2001. **1**(5): p. 231-234.

[22] Skrabalak, S.E. and K.S. Suslick, *Porous MoS2 synthesized by ultrasonic spray pyrolysis.* Journal of the American Chemical Society, 2005. **127**(28): p. 9990-9991.

[23] Balgis, R., et al., *Morphology control of hierarchical porous carbon particles from phenolic resin and polystyrene latex template via aerosol process.* Carbon, 2015. **84**: p. 281-289.

[24] Balgis, R., et al., *Nanostructured design of electrocatalyst support materials for high-performance PEM fuel cell application.* Journal of Power Sources, 2012. **203**: p. 26-33.

[25] Bang, J.H., et al., *Porous carbon supports prepared by ultrasonic spray pyrolysis for direct methanol fuel cell electrodes.* The Journal of Physical Chemistry C, 2007. **111**(29): p. 10959-10964.

[26] Fortunato, M.E., M. Rostam-Abadi, and K.S. Suslick, *Nanostructured carbons prepared by ultrasonic spray pyrolysis.* Chemistry of Materials, 2010. **22**(5): p. 1610-1612.

[27] Iskandar, F., et al., *Production of morphology-controllable porous hyaluronic acid particles using a spray-drying method.* Acta biomaterialia, 2009. **5**(4): p. 1027-1034.

[28] Iskandar, F., et al., *Enhanced photocatalytic performance of brookite TiO2 macroporous particles prepared by spray drying with colloidal templating.* Advanced materials, 2007. **19**(10): p. 1408-1412.

[29] Okuyama, K., et al., *Preparation of functional nanostructured particles by spray drying.* Advanced Powder Technology, 2006. **17**(6): p. 587-611.

[30] Panigrahi, S., et al., *General method of synthesis for metal nanoparticles.* Journal of Nanoparticle Research, 2004. **6**(4): p. 411-414.

[31] Mirkhalaf, F., J. Paprotny, and D.J. Schiffrin, *Synthesis of metal nanoparticles stabilized by metal− carbon bonds.* Journal of the American Chemical Society, 2006. **128**(23): p. 7400-7401.

[32] Titirici, M.-M., M. Antonietti, and A. Thomas, *A generalized synthesis of metal oxide hollow spheres using a hydrothermal approach.* Chemistry of Materials, 2006. **18**(16): p. 3808-3812.

[33] Hayashi, H. and Y. Hakuta, *Hydrothermal synthesis of metal oxide nanoparticles in supercritical water.* Materials, 2010. **3**(7): p. 3794-3817.

[34] Manafi, S., H. Nadali, and H.R. Irani, *Low temperature synthesis of multi-walled carbon nanotubes via a sonochemical/hydrothermal method.* Materials Letters, 2008. **62**(26): p. 4175-4176.

[35] Sevilla, M. and A.B. Fuertes, *The production of carbon materials by hydrothermal carbonization of cellulose.* Carbon, 2009. **47**(9): p. 2281-2289.

[36] Titirici, M.-M., M. Antonietti, and N. Baccile, *Hydrothermal carbon from biomass: a comparison of the local structure from poly- to monosaccharides and pentoses/hexoses.* Green Chemistry, 2008. **10**(11): p. 1204-1212.

[37] Zhao, J., et al., *A template-free and surfactant-free method for high-yield synthesis of highly monodisperse 3-aminophenol–formaldehyde resin and carbon nano/microspheres.* Macromolecules, 2012. **46**(1): p. 140-145.

[38] Zheng, M., et al., *An easy catalyst-free hydrothermal method to prepare monodisperse carbon microspheres on a large scale.* The Journal of Physical Chemistry C, 2009. **113**(19): p. 8455-8459.

[39] Vollmer, C., et al., *Microwave Irradiation for the Facile Synthesis of Transition-Metal Nanoparticles (NPs) in Ionic Liquids (ILs) from Metal–Carbonyl Precursors and Ru-, Rh-, and Ir-NP/IL Dispersions as Biphasic Liquid–Liquid Hydrogenation Nanocatalysts for Cyclohexene.* Chemistry–A European Journal, 2010. **16**(12): p. 3849-3858.

[40] Jasuja, K., et al., *Microwave-reduced uncapped metal nanoparticles on graphene: tuning catalytic, electrical, and Raman properties.* The Journal of Physical Chemistry Letters, 2010. **1**(12): p. 1853-1860.

[41] Komarneni, S., et al., *Microwave− polyol process for Pt and Ag nanoparticles.* Langmuir, 2002. **18**(15): p. 5959-5962.

[42] Bilecka, I., I. Djerdj, and M. Niederberger, *One-minute synthesis of crystalline binary and ternary metal oxide nanoparticles.* Chemical Communications, 2008(7): p. 886-888.

[43] Lin, Y., et al., *Instantaneous formation of metal and metal oxide nanoparticles on carbon nanotubes and graphene via solvent-free microwave heating.* ACS applied materials & interfaces, 2011. **3**(5): p. 1652-1664.

[44] Bao, J. and A. Zhang, *Poly (methyl methacrylate) nanoparticles prepared through microwave emulsion polymerization.* Journal of applied polymer science, 2004. **93**(6): p. 2815-2820.

[45] An, Z., et al., *One-step microwave preparation of well-defined and functionalized polymeric nanoparticles.* Journal of the American Chemical Society, 2006. **128**(47): p. 15054-15055.

[46] Guo, J., et al., *Preparation and the physical/electrochemical properties of a Pt/C nanocatalyst stabilized by citric acid for polymer electrolyte fuel cells.* Electrochimica Acta, 2005. **50**(10): p. 1973-1983.

[47] Liu, Z., et al., *Carbon-supported Pt nanoparticles as catalysts for proton exchange membrane fuel cells.* Journal of Power Sources, 2005. **139**(1): p. 73-78.

[48] Li, X. and I.-M. Hsing, *The effect of the Pt deposition method and the support on Pt dispersion on carbon nanotubes.* Electrochimica acta, 2006. **51**(25): p. 5250-5258.

[49] Uzio, D., S. Miachon, and J.-A. Dalmon, *Controlled Pt deposition in membrane mesoporous top layers.* Catalysis Today, 2003. **82**(1): p. 67-74.

[50] Zhou, Y., et al., *Optimal preparation of Pt/TiO2 photocatalysts using atomic layer deposition.* Applied Catalysis B: Environmental, 2010. **101**(1): p. 54-60.

[51] Arutanti, O., et al., *Tailored synthesis of macroporous Pt/WO3 photocatalyst with nanoaggregates via flame assisted spray pyrolysis.* AIChE Journal, 2016. **62**(11): p. 3864-3873.

[52] Li, X., et al., *Simultaneous nitrogen doping and reduction of graphene oxide.* Journal of the American Chemical Society, 2009. **131**(43): p. 15939-15944.

[53] Tan, Y., et al., *Facile Synthesis of Manganese-Oxide-Containing Mesoporous Nitrogen-Doped Carbon for Efficient Oxygen Reduction.* Advanced Functional Materials, 2012. **22**(21): p. 4584-4591.

[54] Long, C., et al., *Nitrogen-Doped Carbon Networks for High Energy Density Supercapacitors Derived from Polyaniline Coated Bacterial Cellulose.* Advanced Functional Materials, 2014. **24**(25): p. 3953-3961.

[55] Arif, A.F., et al., *Synthesis of nitrogen-functionalized macroporous carbon particles via spray pyrolysis of melamine-resin.* RSC Advances, 2016. **6**(86): p. 83421-83428.

[56] Sheng, Z.-H., et al., *Catalyst-free synthesis of nitrogen-doped graphene via thermal annealing graphite oxide with melamine and its excellent electrocatalysis.* ACS nano, 2011. **5**(6): p. 4350-4358.

[57] Avasarala, B., R. Moore, and P. Haldar, *Surface oxidation of carbon supports due to potential cycling under PEM fuel cell conditions.* Electrochimica Acta, 2010. **55**(16): p. 4765-4771.

[58] Engl, T., L. Gubler, and T.J. Schmidt, *Think Different! Carbon Corrosion Mitigation Strategy in High Temperature PEFC: A Rapid Aging Study.* Journal of The Electrochemical Society, 2015. **162**(3): p. F291-F297.

[59] Kreitmeier, S., A. Wokaun, and F.N. Büchi, *Local catalyst support degradation during polymer electrolyte fuel cell start-up and shutdown.* Journal of The Electrochemical Society, 2012. **159**(11): p. F787-F793.

[60] Gu, W., et al., *Modeling of membrane-electrode-assembly degradation in proton-exchange-membrane fuel cells–local H2 starvation and start–stop induced carbon-support corrosion*, in *Modeling and diagnostics of polymer electrolyte fuel cells*. 2009, Springer. p. 45-87.

[61] Young, A., et al., *A Semi-Empirical Two Step Carbon Corrosion Reaction Model in PEM Fuel Cells.* Journal of The Electrochemical Society, 2013. **160**(4): p. F381-F388.

[62] Shen, Q., et al., *Study on the processes of start-up and shutdown in proton exchange membrane fuel cells.* Journal of Power Sources, 2009. **189**(2): p. 1114-1119.

[63] Shao, Y., et al., *Highly durable graphene nanoplatelets supported Pt nanocatalysts for oxygen reduction.* Journal of Power Sources, 2010. **195**(15): p. 4600-4605.

[64] Ogi, T., et al., *Influence of formic acid on electrochemical properties of high-porosity Pt/TiN nanoparticle aggregates.* AIChE Journal, 2013. **59**(8): p. 2753-2760.

[65] Savych, I., et al., *On the effect of non-carbon nanostructured supports on the stability of Pt nanoparticles during voltage cycling: a study of TiO 2 nanofibres.* Journal of Power Sources, 2014. **257**: p. 147-155.

[66] Saha, M.S., et al., *High electrocatalytic activity of platinum nanoparticles on SnO2 nanowire-based electrodes.* Electrochemical and solid-state letters, 2007. **10**(8): p. B130-B133.

[67] Suzuki, Y., et al., *Sulfated-zirconia as a support of Pt catalyst for polymer electrolyte fuel cells.* Electrochemical and solid-state letters, 2007. **10**(7): p. B105-B107.

[68] Baumard, J., D. Panis, and A. Anthony, *A study of Ti O system between Ti3O5 and TiO2 at high temperature by means of electrical resistivity.* Journal of Solid State Chemistry, 1977. **20**(1): p. 43-51.

[69] Niu, M., et al., *Bandgap engineering of Magnéli phase TinO2n− 1: Electron-hole self-compensation.* The Journal of chemical physics, 2015. **143**(5): p. 054701.

[70] Liborio, L. and N. Harrison, *Thermodynamics of oxygen defective Magnéli phases in rutile: A first-principles study.* Physical Review B, 2008. **77**(10): p. 104104.

[71] Toyoda, M., et al., *Preparation of carbon-coated Magneli phases TinO2n−1 and their photocatalytic activity under visible light.* Applied Catalysis B: Environmental, 2009. **88**(1–2): p. 160-164.

[72] Walsh, F. and R. Wills, *The continuing development of Magnéli phase titanium sub-oxides and Ebonex® electrodes.* Electrochimica Acta, 2010. **55**(22): p. 6342-6351.

[73] Li, X., et al., *Magneli phase Ti 4 O 7 electrode for oxygen reduction reaction and its implication for zinc-air rechargeable batteries.* Electrochimica Acta, 2010. **55**(20): p. 5891-5898.

[74] Ioroi, T., et al., *Formation of electro-conductive titanium oxide fine particles by pulsed UV laser irradiation.* Physical Chemistry Chemical Physics, 2010. **12**(27): p. 7529-7535.

[75] Portehault, D., et al., *Facile general route toward tunable magnéli nanostructures and their use as thermoelectric metal oxide/carbon nanocomposites.* ACS nano, 2011. **5**(11): p. 9052-9061.

[76] Ioroi, T., et al., *Stability of corrosion-resistant Magnéli-phase Ti4O7-supported PEMFC catalysts at high potentials.* Journal of the Electrochemical Society, 2008. **155**(4): p. B321-B326.

Chapter 2

Effect of carbon nanostructures on the oxygen reduction reaction activity of Pt/C electrocatalyst

2.1 Introduction

In response to the needs of modern society and emerging environmental concerns, it is essential to develop renewable, low-cost, and environmentally friendly energy-supplying systems. Proton exchange membrane fuel cells (PEMFCs) are potential candidates, and are continuously being developed and improved.[1-5] One of the factors to be considered in the development of PEMFCs is the electrocatalyst, because it has a significant role in determining the PEMFC performance.[6, 7] Innovations in electrocatalyst materials such as the introduction of various catalyst supports are the key to developing new generations of industrially applicable high-performance electrocatalysts.[8, 9] Carbon nanoparticles (NPs) with high specific surface areas, such as Vulcan carbon, have been widely used as catalyst supports. They significantly reduce the required amount of Pt and improve the performance of the electrocatalyst.[10] The presence of carbon NPs may inhibit rapid agglomeration of Pt NPs under the harsh acid conditions in PEMFCs.

Carbon NPs naturally agglomerate over time. This has disadvantages in electrocatalytic applications because it reduces the amount of active Pt NP sites, inhibits gas flow through a packed catalyst, and reduces the durability of the electrocatalyst. Nanostructuration of carbon particles into three-dimensionally ordered nanostructured particles is one of the most effective approaches in catalyst support development, because the architectural advantages that allow efficient transport phenomena in the PEMFC improve the electrocatalytic performance and durability at low Pt loadings.[11]

The preceding studies prepared several ordered three-dimensional nanostructured materials consisting of Pt deposited on the surfaces of carbon particles (Pt/C) via spray drying, using carbon NPs as the host materials and polystyrene latex (PSL) as a template.[6, 12, 13] The electrocatalytic performance of the Pt/C catalyst improved when the morphology of the carbon particles was changed from dense to hollow.[6] The performance was even higher when

microflower-like porous Pt/C was used.[12, 13] The presence of pores on the carbon particle surfaces and the pore size influence the number of active Pt sites and the hydrodynamics through the packed catalyst. Well-ordered macroporous carbon particles cannot be prepared using the spray-drying method and carbon NPs, because the hydrophobic nature of carbon NPs is not amenable to formation of homogeneous mixtures with PSL particles.[14] Organic materials and polymers that can be converted to carbon, such as phenolic resin, are suitable for the production of carbon particles with well-ordered structures.[15] Moreover, the synthesis of carbon from phenolic resin is suitable for industrial applications because of the high production yield and inexpensive raw material.[16] Functionalization of phenolic resin for the synthesis of three-dimensionally ordered carbon particles for catalyst supports is also promising, because the aromatic structures may give high electronic conductivity. However, the morphology that is appropriate for a catalyst support still needs to be determined.

This study investigated how nanostructuration of a catalyst support determines the Pt deposition behavior and catalytic activity of the Pt/C catalyst. The effects of various morphologies and pores sizes of catalyst supports on the catalytic activity were deeply evaluated, because, to date, only three-dimensional carbon particles with nano- to meso-sized pores have been evaluated.[17, 18] This study finally determined the best catalyst support structure for achieving higher Pt catalytic activity. A fluid dynamic approach was also used as a simple but effective tool to explain the correlation between the structure of the catalyst support and the catalytic activity. We clarified how transport phenomena affect the catalytic activity, in terms of electrochemical kinetics. The catalytic activity was qualitatively estimated by observing the flow pattern of the reactant through the catalyst support during activity tests.

2.2 Experimental

2.1.1 Preparation of Pt/C electrocatalysts via hybrid aerosol and microwave (MW)-assisted colloidal processes

Nanostructured NPs with various morphologies were prepared from an aqueous solution containing 0.25 wt% phenolic resin (Sumitomo Bakelite Co., Ltd., Tokyo, Japan) and PSL particles of various sizes and with various charges, using a spray method, as described in our earlier report.[19] A tubular furnace consisting of four stacked temperature zones set at 150, 300, 1000, and 1000 °C was used. N_2 gas was used to carry droplets through the furnace at controlled flow rates of 0.8 L min^{-1}, as shown in **Figure 2.1(a)**. Positively and negatively charged PSL particles were used to control self-assembly of the phenolic resin and charged

PSL particles. Hollow and porous carbon particles were obtained by fixing the mass ratio of phenolic resin to PSL particles (~230 nm in diameter) at 0.63, because this is a sufficient mass ratio to obtain completely hollow and well-structured carbon particles, as found in our previous study.[19] PSL particles of three different sizes (i.e., ~100, ~230, and ~300 nm) were used to adjust the pore sizes of the carbon particles.

Pt NP deposition was performed using an MW-assisted colloidal process, as shown in **Figure 2.1(b)**. The nanostructured carbon particles (10 mg) were dispersed in ethylene glycol (EG; 20 mL) by ultrasonication for 2 min. Chloroplatinic acid was added and the solution was ultrasonicated for 30 min. The solution was subjected to MW heating for 2 min in an MW-assisted organic synthesis Initiator^{+} (Biotage, Uppsala, Sweden) operated at 150 °C. The solution was cooled to room temperature, and the product was continuously washed with ultrapure water (300 mL) at 80 °C to remove excess EG. The product was dried in a vacuum furnace at 80 °C for 30 min and reheated at 200 °C for 1 h in air.

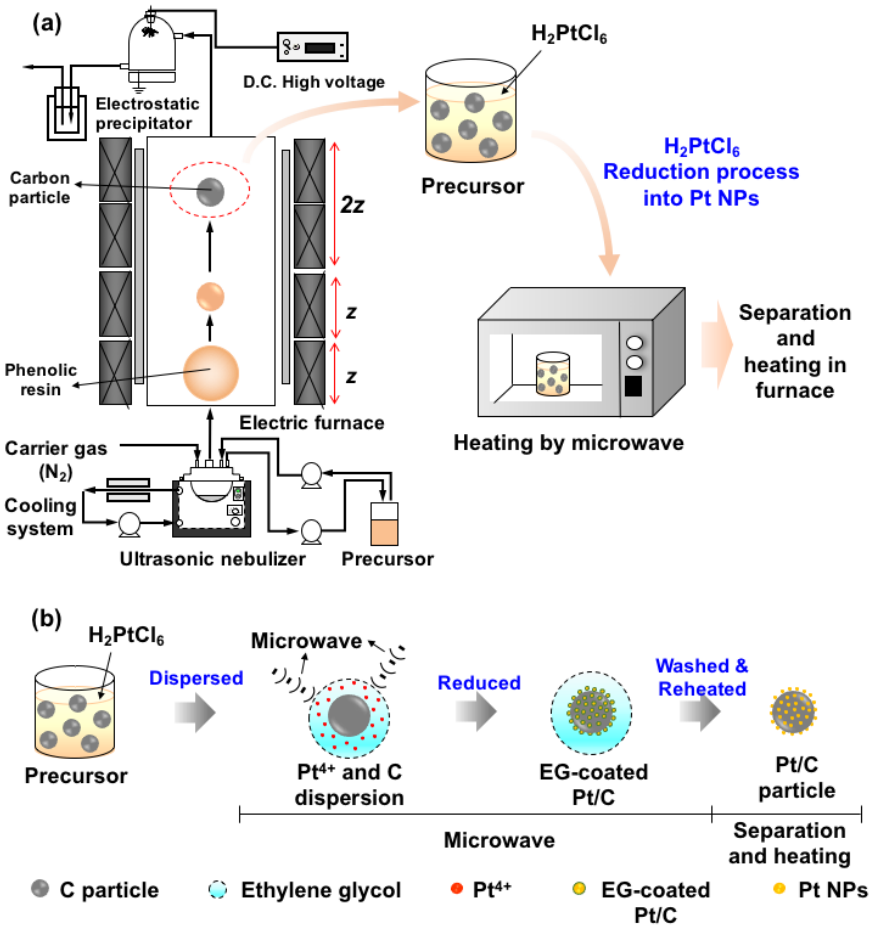

Figure 2.1. Schematics of (a) experimental setup and (b) Pt NP deposition process via EG-assisted MW method

2.2.2 Materials characterization

The zeta potentials and PSL particle sizes (D_p) of aqueous solutions containing either phenolic resin, PSL, or both were determined using a zetasizer (Zetasizer Nano ZSP, Malvern Instruments Ltd., Malvern, UK). The catalyst morphology was observed using field-emission scanning electron microscopy (SEM; S-5000, 20 kV, Hitachi High-Tech. Corp., Tokyo, Japan) and transmission electron microscopy (TEM; JEM-2010, 200 kV, JEOL Ltd., Tokyo, Japan). The amount of Pt in the catalyst was determined using inductively coupled plasma mass spectrometry (SPS-3000, Seiko Instrument Inc., Chiba, Japan). The crystal structures of the Pt/C particles were determined using X-ray diffraction (XRD; D2 PHASER, Bruker Corp., Billerica, MA, USA). The surface areas of the nanostructured carbon particles were determined quantitatively by N_2 adsorption–desorption (BELSORP-max, BEL Japan, Inc., Osaka, Japan), using the Brunauer–Emmett–Teller (BET) method.

2.2.3 Electrochemical characterization

Electrochemical characterization was performed using cyclic voltammetry (CV) and a rotating disk electrode (HR-301, Hokuto Denko Corp., Tokyo, Japan), as shown in **Figure 2.2(a)**. A reversible hydrogen electrode was used as the reference electrode for these measurements. A catalyst ink was prepared by dispersing Pt/C catalyst (3.8 g) in a mixture of ultrapure water (3.8 mL) and isopropanol (1.2 mL; Cica-reagent, Kanto Chemical Co. Inc., Tokyo, Japan). A Nafion® dispersion (5 wt%, 20 μL; Wako Pure Chemical Industries Ltd., Osaka, Japan) was added, and the mixture was placed in an ice bath and sonicated for about 30 min. Catalyst ink (10 μL) was transferred to a polished glassy carbon disk and allowed to dry, to form a thin catalyst film. The amount of Pt on the glassy carbon was 5.8 μg-Pt cm^{-2}. The electrochemical measurement steps and conditions used were described in earlier publication.[6]

2.2.4 Model of fluid flow through nanostructured Pt/C catalyst

A computational simulation was conducted to illustrate the theoretical flow pattern of dissolved oxygen inside the catalyst layer during oxygen reduction reaction (ORR) activity tests. The simulation was performed in two steps. The first step was calculation of the electrolyte velocity on the surface of the catalyst layer, using FlexPDE 6.0. The test chamber, of radius R, was simplified and modeled using cylindrical coordinates, i.e., r, θ, and z, as shown in **Figure 2.2(b)**. Rotation of the electrode caused an axisymmetric swirling flow inside

the test chamber. In this particular case, the flow pattern in one half of the chamber can be assumed to be the same as that in the other half, therefore only half of the chamber was simulated, as shown in **Figure 2.2(c)**. The effects of oxygen diffusion were assumed to be insignificant compared with those of forced convection by electrode rotation. The movement of dissolved oxygen was therefore mainly driven by the rotational force. Eqs. (1)–(3) were applied for swirling flow at a steady state, according to FlexPDE.

Axial momentum equation

$$\rho\left(v_r\frac{\partial v_z}{\partial r}+v_z\frac{\partial v_z}{\partial z}\right)=-\frac{\partial p}{\partial z}+\mu\left[\frac{\partial^2 v_z}{\partial r^2}+\frac{\partial^2 v_z}{\partial z^2}\right]+L_z \tag{1}$$

Radial momentum equation

$$\rho\left(v_r\frac{\partial v_r}{\partial r}+v_z\frac{\partial v_r}{\partial z}-\frac{v_\theta^2}{r}\right)+\frac{\partial p}{\partial r}=\mu\left[\frac{\partial^2 v_r}{\partial r^2}+\frac{\partial^2 v_r}{\partial z^2}-\frac{v_r}{r^2}\right]+L_r \tag{2}$$

Circumferential momentum equation

$$\rho\left(v_r\frac{\partial v_\theta}{\partial r}+v_z\frac{\partial v_\theta}{\partial z}-\frac{v_r v_\theta}{r}\right)=\mu\left[\frac{\partial^2 v_\theta}{\partial r^2}+\frac{\partial^2 v_\theta}{\partial z^2}-\frac{v_\theta}{r^2}\right]+L_\theta \tag{3}$$

ρ, μ, v, p, r, and L are the mass density, viscosity, velocity, pressure, distance from the center of the cylinder in the radial direction, and angular momentum, respectively. Subscript letters indicate the directions of the variables in cylindrical coordinates.

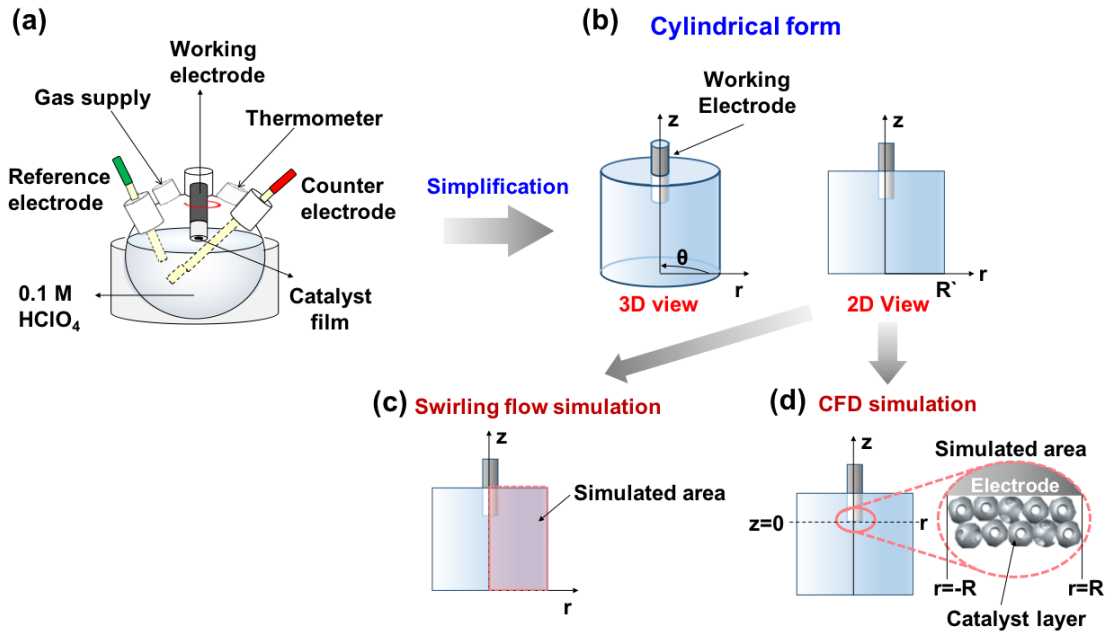

Figure 2.2. Schematics of (a) ORR activity test, (b) simplified ORR test chamber for fluid flow simulation, (c) simulated area for swirling flow simulation, and (d) simulated area for CFD simulation

The angular momentum represents the force caused by electrode rotation at an angular velocity ω, as defined in Eqs. (4)–(6).

$$L_z = mr\omega^2 v_z \tag{4}$$

$$L_r = mr\omega^2 v_r \tag{5}$$

$$L_\theta = mr\omega^2 v_\theta \tag{6}$$

There was no slip between the electrolyte and the wall of the test chamber, therefore v_r, v_z, and v_θ equal zero at $r = R$. The axial, radial, and circumferential velocities are assumed to be constant in the θ direction.

In the second step, the velocity distribution inside the catalyst layer was simulated using Autodesk Simulation CFD 2015. The catalyst layer was simplified to a cross-sectional view of 10 magnified catalyst particles randomly packed in two layers, as shown in Figure 2(d), for better visualization of the channels between catalyst particles. The building geometry was developed and meshed using AutoCAD 2015. Three sets of catalyst were prepared and simulated separately, i.e., one set of hollow catalyst and two sets of porous catalysts. The pore:particle diameter ratios of the porous catalyst sets were 0.3 and 0.5, respectively. The predicted velocity at the electrode surface obtained in the first step of the simulation was used as the inlet boundary for Eqs. (7)–(9).

Axial momentum equation

$$\rho\left(\frac{\partial v_z}{\partial t} + v_r\frac{\partial v_z}{\partial r} + v_z\frac{\partial v_z}{\partial z}\right) = -\frac{\partial p}{\partial z} + \mu\left[\frac{1}{r}\frac{\partial}{\partial r}\left(r\frac{\partial v_z}{\partial r}\right) + \frac{\partial^2 v_z}{\partial z^2} + \right] + \rho g_z \tag{7}$$

Radial momentum equation

$$\rho\left(\frac{\partial v_r}{\partial t} + v_r\frac{\partial v_r}{\partial r} + v_z\frac{\partial v_r}{\partial z} - \frac{v_\theta^2}{r}\right) = -\frac{\partial p}{\partial r} + \mu\left[\frac{\partial}{\partial r}\left(\frac{1}{r}\frac{\partial}{\partial r}(rv_r)\right) + \frac{\partial^2 v_r}{\partial z^2}\right] + \rho g_r \tag{8}$$

Circumferential momentum equation

$$\rho\left(\frac{\partial v_\theta}{\partial t} + v_r\frac{\partial v_\theta}{\partial r} + v_z\frac{\partial v_\theta}{\partial z} - \frac{v_r v_\theta}{r}\right) = \mu\left[\frac{\partial}{\partial r}\left(\frac{1}{r}\frac{\partial}{\partial r}(rv_\theta)\right) + \frac{\partial^2 v_\theta}{\partial z^2}\right] + \rho g_\theta \tag{9}$$

Oxygen diffusion in the electrolyte obeyed Fick's law. The continuity equation, Eq. (10), was used to simulate the oxygen transport.

$$\rho\left(\frac{\partial X}{\partial t}+v_r\frac{\partial X}{\partial r}+\frac{v_\theta}{r}\frac{\partial X}{\partial \theta}+v_z\frac{\partial X}{\partial z}\right) = \rho D_{O_2}\left[\frac{1}{r}\frac{\partial}{\partial r}\left(r\frac{\partial X}{\partial r}\right)+\frac{1}{r^2}\frac{\partial^2 X}{\partial \theta^2}+\frac{\partial^2 X}{\partial z^2}\right] \quad (10)$$

Where X, ρ, and D_{O_2} are the mass fraction, mass density, and diffusivity of oxygen, respectively. Oxygen was supplied to the catalyst at a constant concentration and the pressure at r = R and r = -R were set as atmospheric. The dissolved oxygen concentration at the inlet boundary was calculated based on Henry's law. It was assumed that the Pt particle size was homogeneous in all cases.

2.3 Results and Discussions

2.3.1 Nanostructuration of carbon particles for catalyst support

Spray pyrolysis of an aqueous solution containing phenolic resin resulted in the formation of dense spherical carbon particles. The morphology of the carbon particles was tuned by adding controllable charged PSL particles as a template. The addition of positively charged PSL created an attractive force with the negatively charged phenolic resin, and PSL–phenolic resin with a core–shell structure was formed. The addition of negatively charged PSL created a repulsive force with the negatively charged phenolic resin, which made both particles move independently in the droplets.[14] **Figure 2.3** shows the various carbon particle morphologies after nanostructuration. Spray pyrolysis of the phenolic resin gave spherical dense carbon particles, as shown in **Figure 2.3(a)**. The addition of positively and negatively charged PSL particles resulted in hollow and porous carbon particles, as shown in **Figure 2.3(b)** and **(c)**, respectively; this is consistent with our previous work.[14, 19] The morphologies of the obtained carbon particles were confirmed using TEM. Figure 3(c) shows the formation of a completely spherical and dense morphology. Macropores covered by thin shells of carbon are clearly observed in Figure 3(d); this confirms the formation of a hollow morphology. Figure 3(e) shows the formation of macropores inside and on the surfaces of carbon particles.

The structural properties of the obtained carbon particles were evaluated using N_2 adsorption–desorption measurements; the isotherm curves are shown in **Figure 2.3(f)**. The isotherm curves show an initial rapid rise in the adsorbed gas volume with increasing relative pressure, followed by a slow increase, i.e., type II isotherm curves. The inset in **Figure 2.3(f)** shows the inflection point corresponding to both completion of monolayer coverage and pore filling by capillary condensation. It can be seen that dense carbon particle adsorbed the highest

volume of N_2, followed by hollow and porous carbon particles, respectively, indicating that the dense carbon particles had larger amounts of micropores than did the hollow and porous carbon particles. The isotherm curve of the dense carbon particles shows no hysteresis, whereas that of the hollow carbon particles shows type C hysteresis, which was identified by de Boer as indicating a mixture of tapered or wedge-shaped pores with open ends.[20] In contrast, the porous carbon curve shows type A hysteresis, which is principally caused by cylindrical pores open at both ends.[20] The specific surface areas (S_{BET}) of the particles were calculated to be 490.7, 95.8, and 69.9 $m^2\ g^{-1}$ for dense, hollow, and porous carbon particles, respectively.

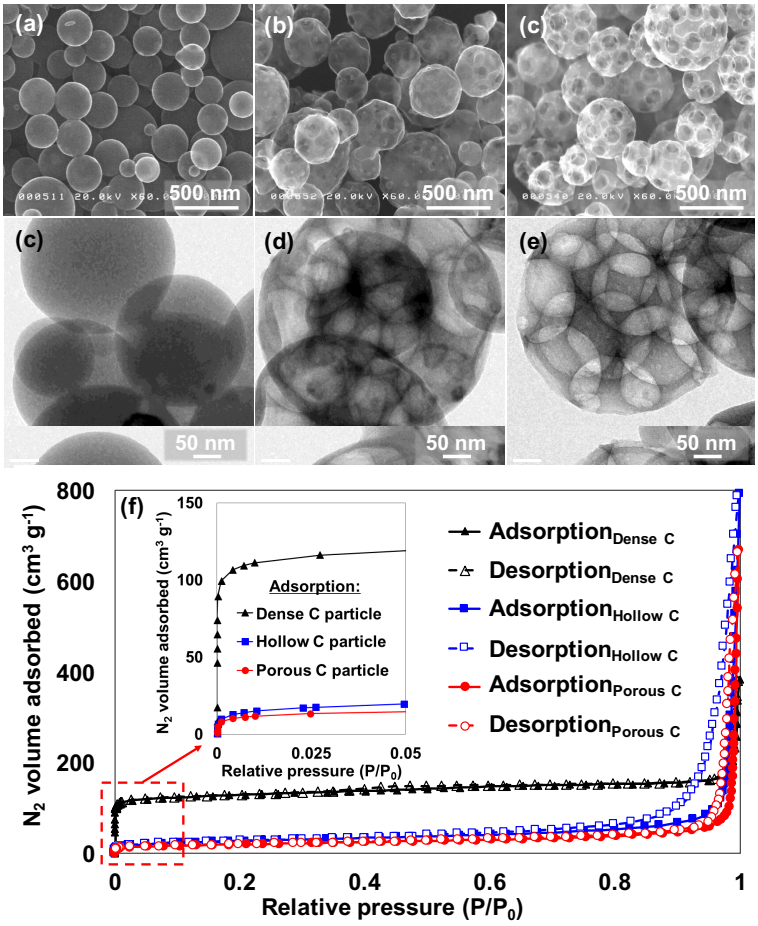

Figure 2.3. SEM and TEM images of (a, c) dense, (b, d) hollow, and (c, e) porous carbon particles; (f) N2 adsorption–desorption isotherm curves of nanostructured carbon particles

2.3.2 Morphologies and crystallinities of nanostructured Pt/C catalysts

The aim of this work was to investigate the effects of structural engineering of the catalyst support on the activity of the Pt catalyst. The configuration of the catalyst support structure is critical for effective gas/water diffusion and proton/electron transport to and from the catalytic

sites without sacrificing sites for Pt deposition. In this study, carbon particles with three different morphologies, namely dense, hollow, and porous, were used. They were synthesized using an aerosol spray pyrolysis process, as described elsewhere.[19]

Functionalization of the nanostructured carbon particles was performed by Pt deposition (~15 wt%) on the nanostructured carbon surfaces, with mediation by EG, using an MW method, as shown in **Figure 2.1(b)**. Pt^{4+} from chloroplatinic acid and nanostructured carbon particles were dispersed in EG, which acted as a solvent, a binder, and a Pt-ion reducing agent. The Pt ions were well dispersed in EG; after reduction, they were deposited on the surfaces of the nanostructured carbon particles. The MWs transferred heat evenly into the precursor up to 150 °C, which can accelerate reduction of Pt. The entire surface of the nanostructured carbon particle soon became well decorated with uniform-sized Pt NPs. The growth of Pt NPs was restrained by the presence of EG as a binder. The EG that remained on the surfaces of the Pt NPs was removed using high-temperature ultrapure water, so that it did not affect the Pt/C catalyst.

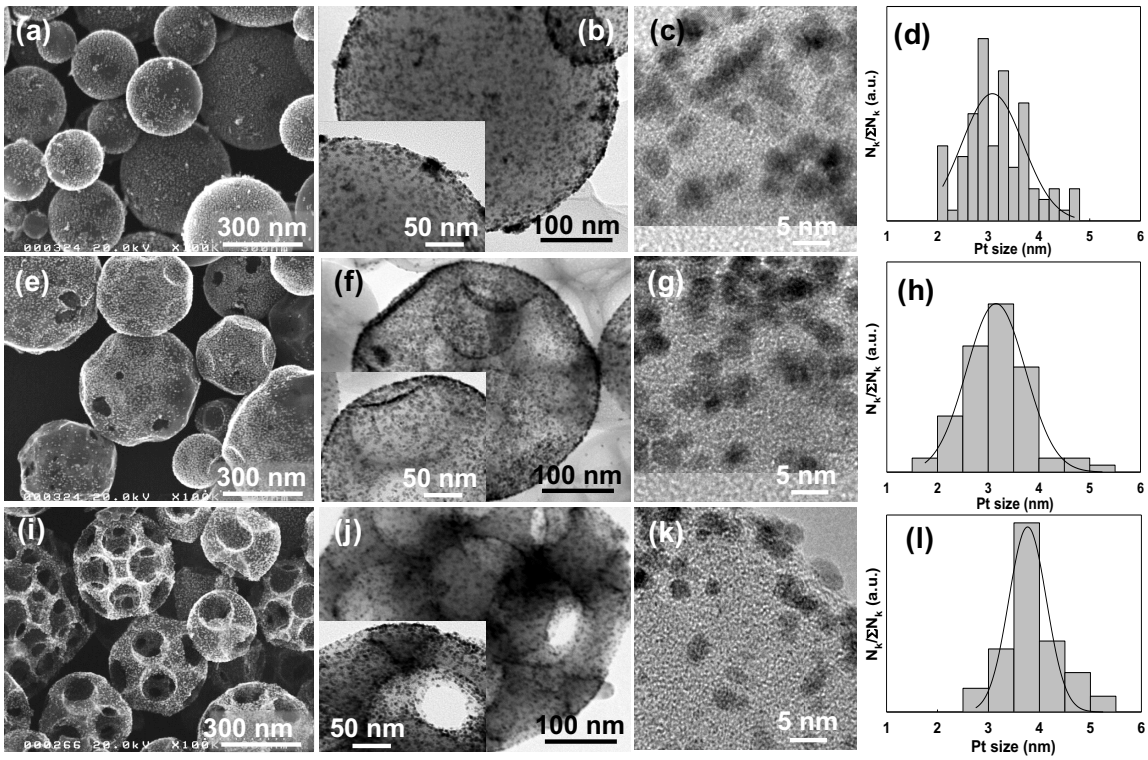

Figure 2.4. SEM, TEM, and high-resolution TEM images and histogram of Pt NP size distributions for (a–d) Pt/Cdense, (e–h) Pt/Chollow, and (i–l) Pt/Cporous catalysts

Figure 2.4 shows SEM and TEM images of the nanostructured Pt/C catalysts. The figure shows that Pt NPs were deposited on the surfaces of the dense and hollow carbon particles. The Pt NPs were well dispersed, although some Pt agglomeration was observed, as shown in **Figure 2.4(a–g)**. The TEM images in **Figure 2.4(b)** confirm the formation of Pt islands in some parts of the dense carbon particles. Less Pt agglomeration was observed on the hollow carbon particles, as shown in **Figure 2.4(f)**, and use of the porous carbon particles led to agglomeration-free Pt NPs, as shown by the SEM and TEM images in **Figure 2.4(i)** and **(j)**.

The high-resolution TEM images in the insets of **Figure 2.4(b), (f), and (j)** indicate that Pt NPs were also deposited on the inner surfaces of the porous carbon particles, and even in cavities. The open macropores on the carbon particle surfaces probably provide paths for Pt NPs to pass through the exterior and become deposited on the inner surfaces of the carbon particles. Furthermore, the wettability, which can create tension on the pore surfaces, is inversely proportional to the pore size. Dense carbon particles with only micro- and meso-pores on their surfaces showed the highest rejection on their pores surfaces. The freshly reduced Pt NPs could not penetrate into the pores, either because the pore size was smaller than the Pt size or the barriers formed on the pore surfaces obstructed the entrances. Similar phenomena were also observed for the hollow carbon particles. However, once the Pt NPs were able to penetrate the surface barriers, it was possible for the Pt NPs to be dispersed on the surfaces of the inner pores, which were larger. In contrast to the micro- and meso-pores, rejection on the macropore surfaces was much lower. The Pt NPs were therefore able to penetrate easily into the pores and cavities, as a result of EG flow. Histograms of the size distributions of the Pt NPs on the surfaces of dense, hollow, and porous carbon particles are shown in **Figure 2.4(d), (h), and (l)**, respectively, and the average sizes are about 3.2, 3.2, and 3.9 nm, respectively.

To deepen our understanding of the effects of Pt NP deposition on the surfaces of porous carbon particles, three pore sizes, i.e., 85, 120, and 165 nm, were examined. **Figure 2.5** shows that Pt NP dispersion improved with increasing pore size. The Pt NPs were agglomerated and localized on some of the carbon particles with a pore size of 85 nm, as shown in **Figure 2.5(b)**, but well dispersed on the surfaces of carbon particles with pore sizes of 120 and 165 nm [**Figure 2.5(f) and (j)**, respectively]. These results emphasize that Pt NP dispersion is affected not only by the morphology, but also by the pore size of the catalyst support. The Pt NP sizes calculated from the high-resolution TEM images for more than 250 NPs were about 4.7, 3.9, and 3.9 nm for Pt/C with pore sizes of 85, 120, and 165 nm, respectively; the histograms are shown in Figure **2.5(d), (h), and (l)**, respectively.

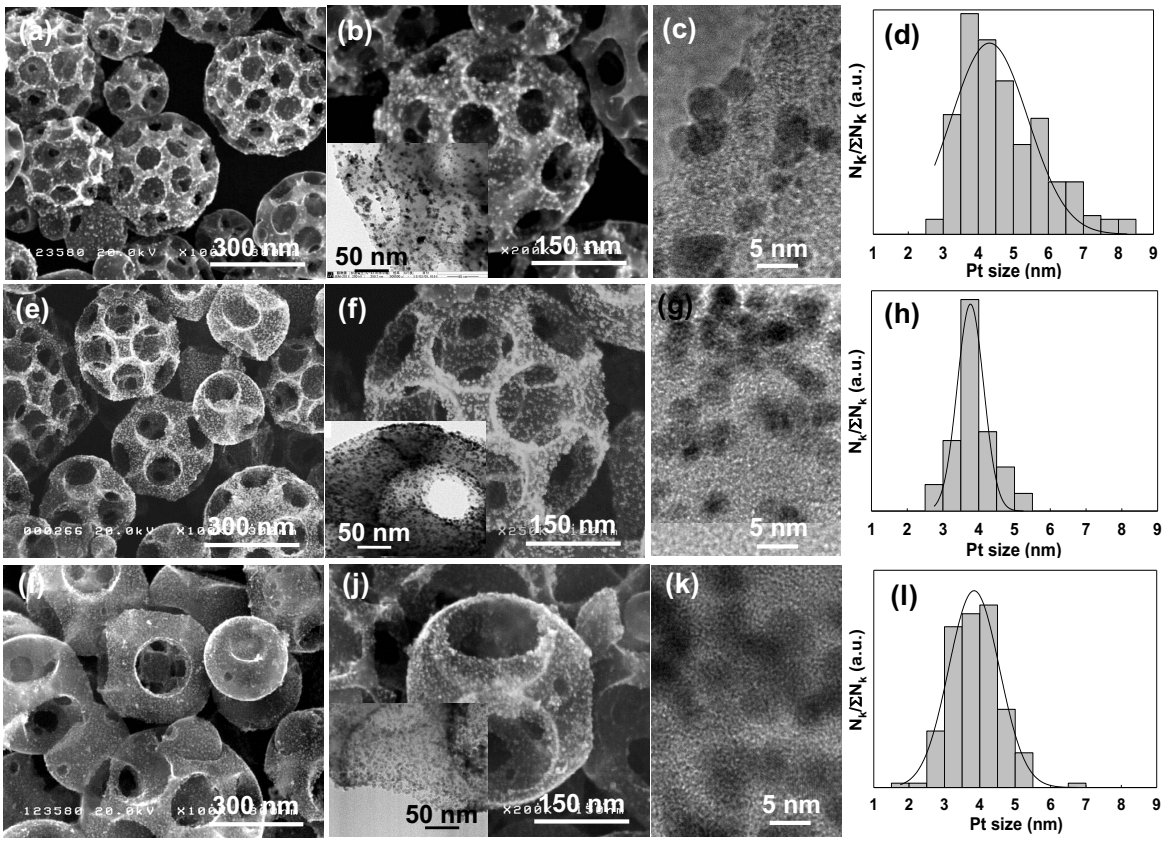

Figure 2.5. SEM, TEM, and high-resolution TEM images and histogram of Pt NP size distributions for Pt/Cporous catalysts with pore sizes of (a–d) 85 nm, (e–h) 120 nm, and (i–l) 165 nm

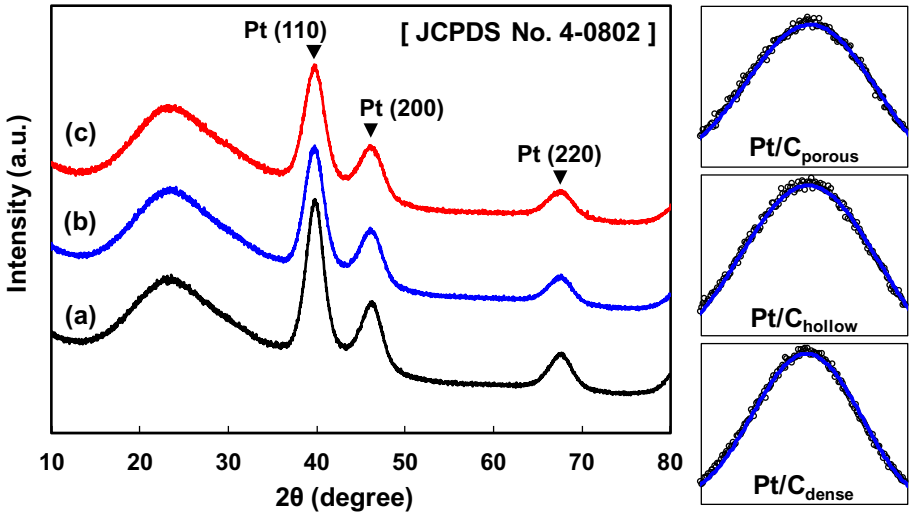

Figure 2.6. XRD patterns of Pt/C catalysts: (a) dense, (b)hollow, and (c) porous, with pore sizes of 120 nm

The XRD patterns of the dense, hollow, and porous Pt/C particles are shown in **Figure 2.6**. A broad peak at around 2θ 25°, corresponding to the diffraction of carbon black, is observed in all the XRD patterns. Pt diffraction peaks are clearly observed for all particles, at 2θ 39°, 46°, and 68°, corresponding to the (111), (200), and (220) crystal planes, respectively (JCPDS card No. 4-0802). The crystallite sizes of the Pt NPs, calculated using the Scherrer equation, were 2.5, 2.3, and 2.2 for dense, hollow, and porous Pt/C, respectively. The crystallite sizes of the Pt NPs were slightly smaller than the diameters calculated from the TEM images. This indicates aggregation of Pt crystals, although some Pt particles grew individually.

2.3.3 Electrocatalytic activities of nanostructured Pt/C catalysts

The electrochemical characteristics of the prepared Pt/C catalysts were investigated based on CV and ORR polarization curves obtained under the same measurement conditions.

Figure 2.7(a) shows the CV adsorption–desorption characteristics of the dense, hollow, and porous Pt/C catalysts. For the prepared Pt/C catalysts, a weak hydrogen ion adsorption peak in the potential range of 0.31–0.13 V and a strong adsorption peak located between 0.13 and 0.02 V were observed during reverse potential scanning, and were assigned to weakly and strongly bonded hydrogen atoms, respectively. Pt/C_{hollow}, and Pt/C_{porous} show the typical voltammograms of Pt/C, however Pt/C_{dense} has a very broad peak at a potential range of 0.7–0.4 V showing that it has a high pseudo-capacitance. The electrochemical surface area (ECSA) of Pt in the working electrode was calculated using the hydrogen adsorption charge ($Q_{H\text{-}adsorption}$) limited by the minimum potential, which was selected to be just above the potential of H_2 generation (between 0.3 and ~0.06 V for dense Pt/C; and 0.4 and ~0.06 V for hollow and porous Pt/C). The corresponding desorption peaks were observed during the reverse potential scan. The average of calculated ECSAs were 53.4, 72.8, and 107.4 $m^2\ g^{-1}$-Pt for the Pt/C_{dense}, Pt/C_{hollow}, and Pt/C_{porous} catalysts, respectively. The ECSA value of the Pt/C_{dense} catalyst was lower than that of Pt/C_{hollow}, and that of the Pt/C_{porous} catalyst was highest, almost twice those of the other catalysts. In addition to the effect of Pt agglomeration, which is probably not the major factor, this ECSA value might be affected by the distance between Pt NPs. The external surface area calculated from N_2 adsorption desorption analysis were about 15.4, 64.4, and 41.3 $m^2\ g^{-1}$ for dense, hollow, and porous carbon particles, respectively. Dense carbon particle has the smallest active site for Pt NPs to deposit and make the distance between Pt NPs becomes shorter than those on hollow and porous carbon. Therefore, only Pt surfaces that do not face

each other were active. Hollow carbon particle has the highest external surface area but the interconnected bimodal pore system of the porous structure may lengthen the distance among Pt NPs and suppressed the possibility of Pt migration which would increase the Pt NP active surface area.

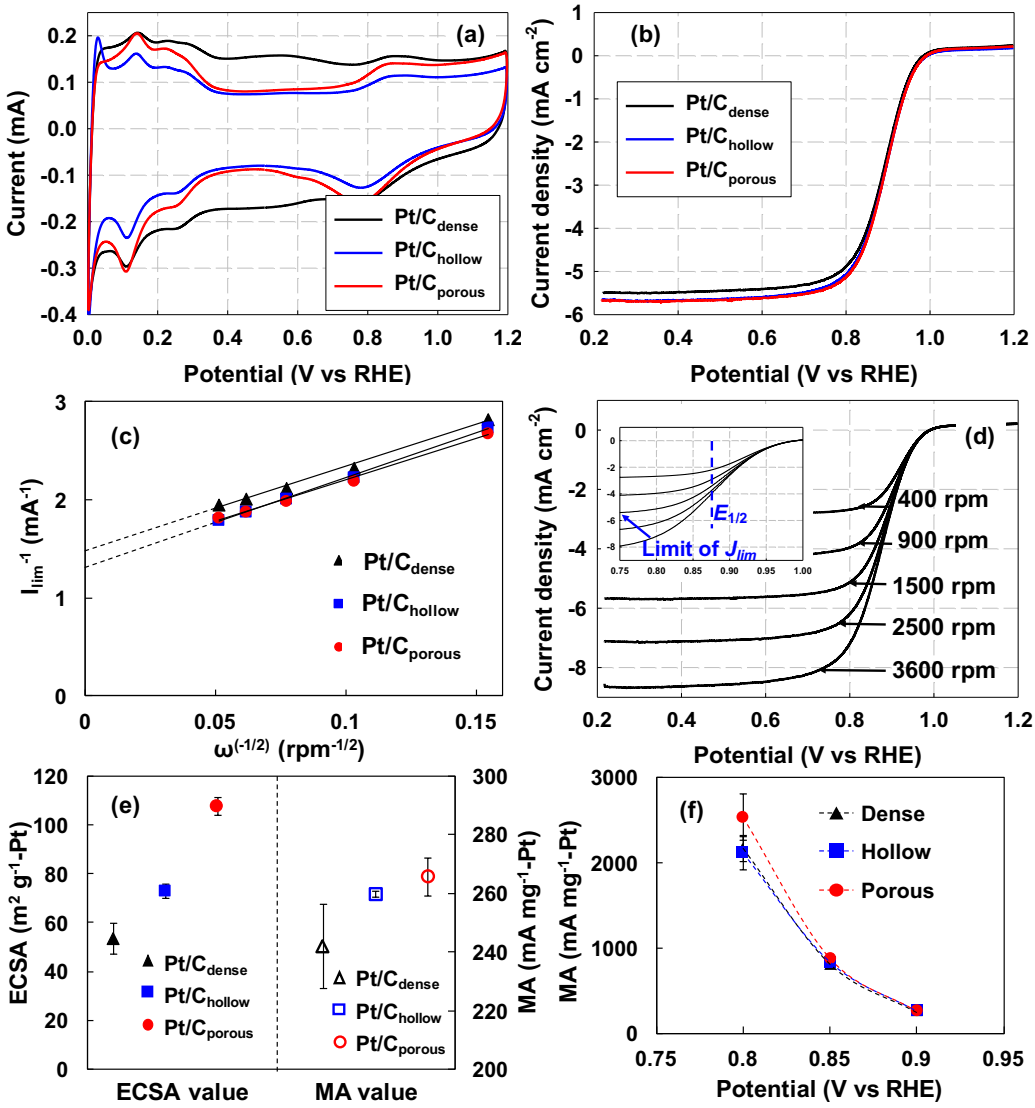

Figure 2.7. (a) CV of Pt/C_{dense}, Pt/C_{hollow}, and Pt/C_{porous} catalysts after 50 cycles in oxygen-free 0.1 M $HClO_4$ (cycling between 0 and 1.2 V at sweep rate of 50 mV s^{-1}), (b) comparison of ORR polarization curves of Pt/C_{dense}, Pt/C_{hollow}, and Pt/C_{porous} catalysts at rotation rate of 1600 rpm after 50 cycles in oxygen-saturated 0.1 M $HClO_4$ at sweep rate of 10 mV s^{-1}, (c) Koutecký–Levich plots for Pt/C_{dense}, Pt/C_{hollow}, and Pt/C_{porous} catalysts at various rotation rates and potential of 0.9 V, (d) ORR polarization curves of Pt/C_{porous} catalysts at different rotation rates, (e) ECSA and MA values at E = 0.9 V, and (f) MA values at various E

Typical oxygen reduction polarization curves for the Pt/C_{dense}, Pt/C_{hollow}, and Pt/C_{porous} catalysts, recorded after 50 CV cycles at a rotation speed of 1600 rpm, are shown in **Figure 2.7(b)**. At an electrode angular speed of 1600 rpm, the diffusion-limiting current density for materials that support direct four-electron transfer, i.e., Pt-based electrodes, usually ranges between −5 and −6 mA cm^{-2}, and can be reached by those three morphologies of the Pt/C catalysts. The ORR activity tests were performed at different rotation speeds (i.e., 400, 900, 1600, 2500, and 3600 rpm) to obtain Koutecký–Levich plots, shown in **Figure 2.7(c)**. The number of electrons involved in the ORR was calculated using the Koutecký–Levich equation[23]; four electrons were involved for all morphology of the Pt/C catalysts. **Figure 2.7(d)** shows the ORR curves of Pt/C porous catalyst at various rotation speeds. The inset of **Figure 7(d)** shows that half-wave potential ($E_{1/2}$, the point half way between zero current and the diffusion-limited current density plateau J_{lim}) was around 0.88 V. Therefore, the target potential for calculation of the mass activities was determined at slightly higher than $E_{1/2}$, at E = 0.9 V. The Pt mass activity (MA) values were calculated by normalizing the Pt loading on the disk electrode. The Pt/C_{porous} catalyst showed the highest mass activity about 265.6 mA mg^{-1}-Pt, followed by Pt/C_{hollow} and Pt/C_{dense} which were about 259.5 and 241 mA mg^{-1}-Pt, respectively. The summary of electrocatalytic activities (ECSA and MA) were shown in **Figure 2.7(e)**. Pt/C_{dense} catalyst has the smallest MA which can be attributed to partial blocking of active catalytic sites, probably by microbubbles formed by cavitation during the ORR activity test. As previously mentioned, the Pt/C_{dense} catalyst had only micro- and meso-pores. The microbubbles probably blocked some of the micropores, which would significantly affect the hydrodynamics of the Pt/C_{dense} catalyst. The microbubbles remained unbroken because of the strong convective force in the axial direction at high angular velocities. In addition, low charge transfer as a result of the low overpotential (η) is suspected to contribute to microbubble preservation.

Mass activity of prepared samples was calculated at E, 0.8, 0.85, and 0.9 V as shown in **Figure 2.7(f)**. It is shown that Pt/C_{porous} catalyst has the highest value at all E. These results suggest that the morphology of the carbon catalyst support plays a crucial role in the electrocatalytic performance. The relationship between the carbon morphology and active catalytic sites can be explained based on a fluid flow model, as discussed in section 2.3.5.

2.3.4 Effects of Pt/C catalyst pore size on electrocatalytic activity

Understanding that a porous morphology improves the catalytic performance is important, but knowing the most appropriate pore size for achieving a superior catalytic performance is also vital. Based on this idea, the electrocatalytic activities of Pt/C catalysts with pore sizes of 85, 120, and 165 nm were evaluated. **Figure 2.8(a)** shows the CV adsorption–desorption characteristics of three porous Pt/C catalysts. It should be noted that broad peaks were observed between 0.3 and 0.7 V in both the forward and reverse potential scans for the catalyst with a pore size of 85 and 165 nm, probably because of unpredictable pore formation inside the carbon particles. It was difficult for Pt to reach and be deposited on these pores, but they actively stored charge, resulting in a high pseudo-capacitance.

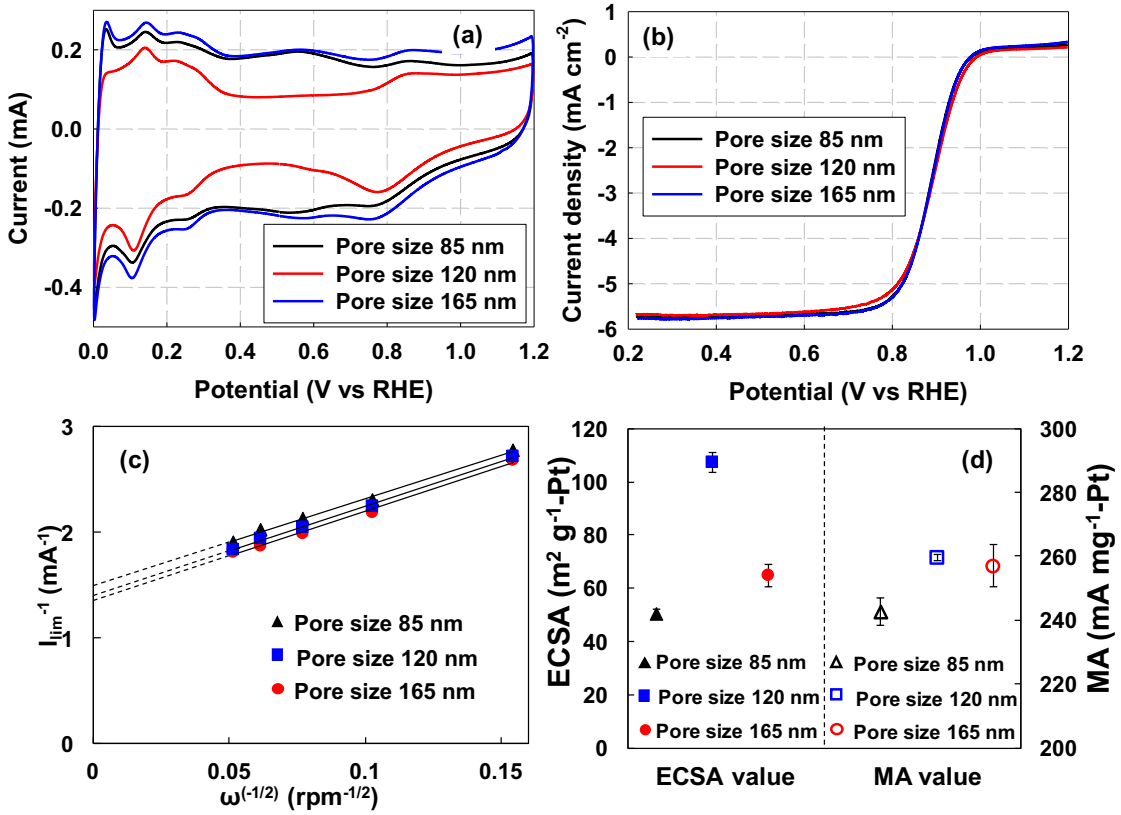

Figure 2.8. (a) CV of Pt/C_{porous} catalysts with pore sizes of 85, 120, and 165 nm after 50 cycles under the same measurement conditions as in Figure 7, (b) comparison of ORR polarization curves of Pt/C_{porous} catalysts with pore sizes of 85, 120, and 165 nm at a rotation rate of 1600 rpm after 50 cycles, (c) Koutecký–Levich plots of Pt/C_{porous} catalysts with pore sizes of 85, 120, and 165 nm at various rotation rates and potential of 0.9 V, and (d) ECSA and MA values of Pt/C_{porous} catalysts with pore sizes of 85, 120, and 165 nm at E = 0.9 V.

Among these curves, that for Pt/C with a pore size of 120 nm shows the clearest and greatest Pt–H adsorption and H_2 evolution peaks. The ECSA was calculated to be 50.3, 107.4, and 64.6 m^2 g^{-1}-Pt for pore sizes of 85, 120, and 165, respectively. The highest ECSA was obtained at a pore size of 120 nm, showing that appropriate contacts among the gas fuel, catalyst, and membrane were obtained at this pore size. The ECSA value of Pt/C with a pore size of 85 nm was extremely low, even lower than that of dense Pt/C, probably because the carbon support predominantly acted as a charge store.

Figure 2.8(b) shows the oxygen reduction polarization curves after 50 CV cycles at a rotation speed of 1600 rpm. All three catalysts show similar diffusion-limited current density plateaus. The Koutecký–Levich plots of catalysts which show similar slope are shown in **Figure 2.8(c)** and were used to calculate the mass and specific activities. The mass activity values quantified at E = 0.9 V for pore sizes of 85, 120, and 165 nm were about 242.6, 259.5, and 256.9 mA mg^{-1}-Pt, respectively. Even though the mass activity of different pores are not much different, but the ECSA are totally different as summarized in **Figure 2.8(d)**. It shows that at a certain size of pores, overall electocatalytic activity can be optimized by optimizing the amount of active Pt catalyst as well as minimize the pseudo capacitance ability.

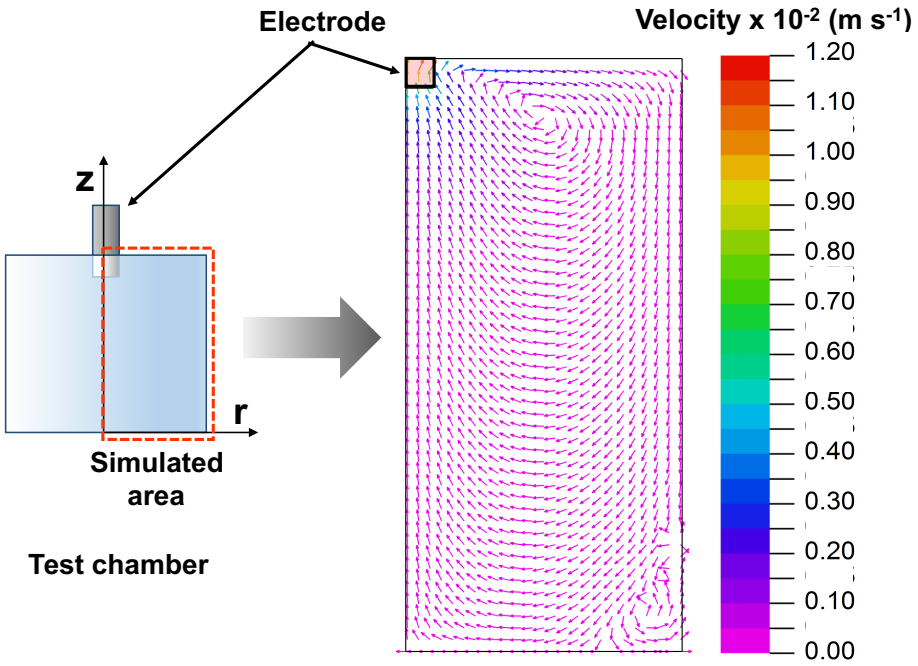

Figure 2.9. Swirl flow pattern in cross-sectional view of half of ORR activity test chamber. This image is reproduced from the FlexPDE 6.0 simulation.

2.3.5 Model of fluid flow around nanostructured Pt/C catalyst

The flow pattern inside the catalyst layer at an electrode angular velocity of 3600 rpm was determined using FlexPDE. At this electrode velocity, the velocity of the fluid entering the catalyst layer was 6×10^{-3} m s^{-1}. Rotation of the electrode resulted in a swirling flow pattern in the test chamber, as shown in **Figure 2.9** for half of the test chamber. The oxygen fraction in the catalyst layer was calculated to be 4.4×10^{-5}, based on Henry's law. The flow pattern and oxygen concentration were used for computational fluid dynamic (CFD) simulation using Autodesk CFD 2015 to show the effects of the pore size on the velocity and oxygen concentration distribution between particles in the catalyst layer. A concentration fraction of 1.0 was set in the CFD simulation to represent an oxygen concentration of 4.4×10^{-5}. The analysis was based on the assumption that Pt NPs of the same size are well distributed on the catalyst support. The ability of the Pt catalyst to adsorb oxygenated species was therefore assumed to be homogenous.[3] The CFD simulation results for various nanostructures are shown in **Figure 2.10(a)–(f)**. The velocity and oxygen concentration profiles are represented by color gradients.

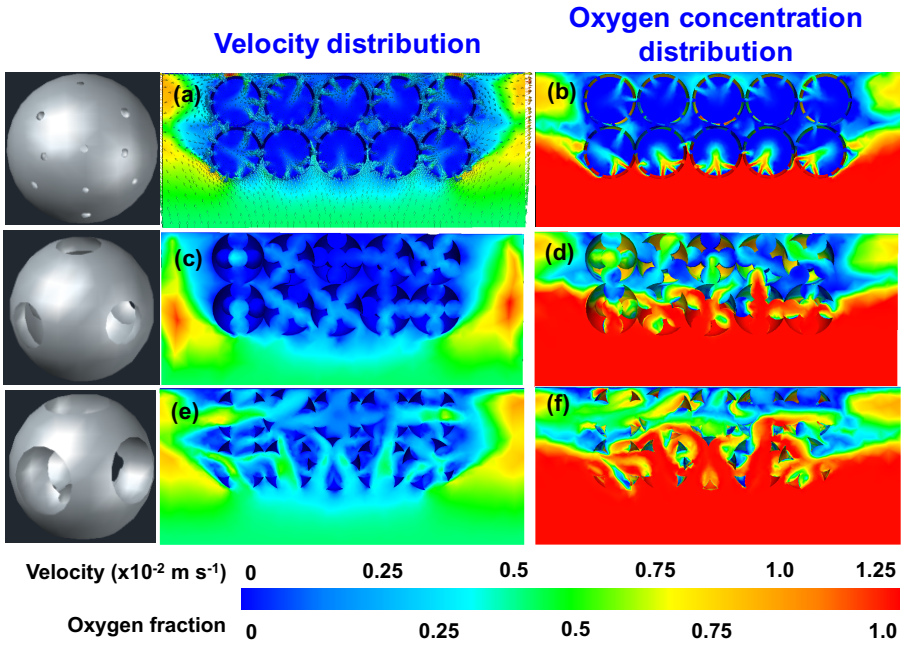

Figure 2.10. Velocity distribution profile in the catalyst layer consisting of (a) hollow carbon particles and porous carbon particles at a pore: particle diameter ratio of (c) 0.3 and (e) 0.5. The corresponding oxygen concentration profile for each type of catalyst is shown in (b), (d), and (f), respectively. Outward appearance of the three-dimensional model of each particle is shown on the left-hand side

Figure 2.10(a) shows the velocity distribution of hollow particles in the packed catalyst. The velocity distribution was inhomogeneous with many stagnant areas, indicated by dark blue. The stagnant areas were particularly concentrated inside the hollows, indicating that the mesopore size was insufficient to allow unhindered flow of the electrolyte into the hollows. Oxygen transport into the hollows would then rely on diffusion only, which is very sluggish compared with convection. As a consequence, the area with stagnant flow had a very low oxygen concentration, indicated by dark blue in **Figure 2.10(b)**.

The absence of convective flow in some areas affected the reaction on the catalyst surface. In such areas, the electrochemical reaction was controlled only by oxygen diffusion. As a consequence, the ORR rate would not exceed the rate of oxygen diffusion to the catalyst surface. In terms of electrochemical kinetics, the current density from the reaction would be equal to the limiting current density, J_{lim}.[21] We are focusing on microscopic-scale diffusion, therefore the surface of the catalyst is regarded as planar. The correlation between J_{lim} and the oxygen concentration is described by Eq. (10).

$$J_{\text{lim}} = nFm_oC_o \tag{10}$$

n, F, m_{o}, and c_{o} denote the number of electrons, Faraday constant, mass transfer coefficient, and oxygen concentration in the bulk solution, respectively. The mass transfer coefficient is defined as the ratio between the diffusivity coefficient and the thickness of the Nernst diffusion layer. Since there was almost no oxygen deployment by convection, the oxygen concentration in the stagnant area tended to be low and decreased over time as the oxygen was consumed by ORR. The decreasing oxygen concentration furthermore resulted in the lower current density (**Figure 2.11**). In the overall system, this is observed as a low ECSA. The limiting current, however, may not be observed in the catalyst polarization measurements, because it occurs locally.

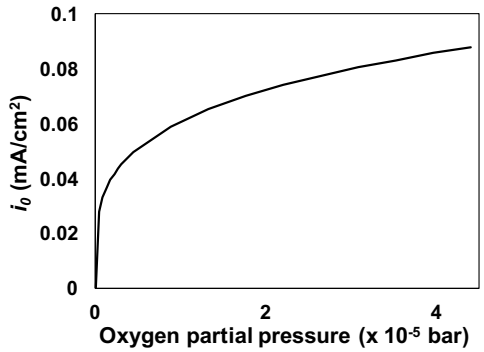

Figure 2.11. Correlation between oxygen partial pressure and limiting current density

Figure 2.10(c) shows the velocity distribution in the packed catalyst with a pore:particle diameter ratio of 0.3. The velocity distribution was much more homogeneous than that in the hollow particles, although many stagnant areas were still present. The pore size was not large enough to create perfect channels inside the structure, therefore the electrolyte flow was obstructed by the catalyst wall in some areas. The sluggish diffusion of oxygen in the absence of convective flow resulted in a low oxygen concentration in that particular area, as seen in **Figure 2.10(d)**.

When particles with larger pores were used as the catalyst, the pores were interconnected, although the particles were randomly packed, as shown in **Figure 2.10(c)**. The interconnected pores created channels that allowed the fluid to pass through the particles with fewer obstacles, resulting in a better velocity distribution. The stagnant area in **Figure 2.10(e)** is smaller than that in **Figure 2.10(c)**, because of the larger pores. As a result of better convective flow, oxygen transfer to the electrode surface was more effective, indicated by smaller blue areas in **Figure 2.10(f)**. In this case, the reaction rate only depends on the activation overpotential, in accordance with the Butler–Volmer equation. Despite the good transport phenomena, excessively large pores in a catalyst may be disadvantageous because the surface area of the catalyst decreases and the catalyst tends to be brittle.

2.4 Conclusion

The electrocatalytic performances of nanostructured Pt/C catalysts were comprehensively evaluated. The effects of the catalyst support morphology (i.e., dense, hollow, and porous) and pore size on the electrocatalytic performance were studied. It was clearly found that the performance of the porous carbon Pt/C catalyst was the best among those of the three types of catalyst, probably because of the presence of interconnected pores, which allowed better oxygen transport to the catalyst surface. Furthermore, good oxygen transport promoted effective charge transfer and consequently increased the active surface area of the catalyst. These phenomena were confirmed by fluid dynamic simulations, which were analyzed in terms of electrochemical kinetics. These results prove the effectiveness of the fluid dynamic approach in qualitatively estimating the electrocatalytic performance by observing hydrodynamic phenomena within the catalyst layer.

2.5 References

[1] Aricò, A.S., et al., *Nanostructured materials for advanced energy conversion and storage devices.* Nature materials, 2005. **4**(5): p. 366-377.

[2] Candelaria, S.L., et al., *Nanostructured carbon for energy storage and conversion.* Nano Energy, 2012. **1**(2): p. 195-220.

[3] Mayrhofer, K., et al., *Measurement of oxygen reduction activities via the rotating disc electrode method: From Pt model surfaces to carbon-supported high surface area catalysts.* Electrochimica Acta, 2008. **53**(7): p. 3181-3188.

[4] Service, R.F., *Fuel cells. Shrinking fuel cells promise power in your pocket.* Science (New York, NY), 2002. **296**(5571): p. 1222.

[5] Stamenkovic, V., et al., *Changing the activity of electrocatalysts for oxygen reduction by tuning the surface electronic structure.* Angewandte Chemie, 2006. **118**(18): p. 2963-2967.

[6] Balgis, R., et al., *Nanostructured design of electrocatalyst support materials for high-performance PEM fuel cell application.* Journal of Power Sources, 2012. **203**: p. 26-33.

[7] Balgis, R., et al., *Self-organized macroporous carbon structure derived from phenolic resin via spray pyrolysis for high-performance electrocatalyst.* ACS applied materials & interfaces, 2013. **5**(22): p. 11944-11950.

[8] Sharma, S. and B.G. Pollet, *Support materials for PEMFC and DMFC electrocatalysts—a review.* Journal of Power Sources, 2012. **208**: p. 96-119.

[9] Shao, Y., et al., *Novel catalyst support materials for PEM fuel cells: current status and future prospects.* Journal of Materials Chemistry, 2009. **19**(1): p. 46-59.

[10] Fang, B., et al., *Hierarchical nanostructured hollow spherical carbon with mesoporous shell as a unique cathode catalyst support in proton exchange membrane fuel cell.* Physical Chemistry Chemical Physics, 2009. **11**(9): p. 1380-1387.

[11] Qiao, Y. and C.M. Li, *Nanostructured catalysts in fuel cells.* Journal of Materials Chemistry, 2011. **21**(12): p. 4027-4036.

[12] Balgis, R., et al., *Rapid In Situ Synthesis of Spherical Microflower Pt/C Catalyst Via Spray‐drying for High Performance Fuel Cell Application.* Fuel Cells, 2012. **12**(4): p. 665-669.

[13] Balgis, R., et al., *Ultrahigh oxygen reduction activity of Pt/nitrogen-doped porous carbon microspheres prepared via spray-drying.* Journal of Power Sources, 2013. **229**: p. 58-64.

[14] Balgis, R., et al., *Aerosol synthesis of self-organized nanostructured hollow and porous carbon particles using a dual polymer system.* Langmuir, 2014. **30**(38): p. 11257-11262.

[15] Zhang, S., et al., *Facile synthesis of hierarchically ordered porous carbon via in situ self-assembly of colloidal polymer and silica spheres and its use as a catalyst support.* Chemistry of Materials, 2010. **22**(11): p. 3433-3440.

[16] Ryu, J., et al., *Hydrothermal preparation of carbon microspheres from mono-saccharides and phenolic compounds.* Carbon, 2010. **48**(7): p. 1990-1998.

[17] Galeano, C., et al., *Toward highly stable electrocatalysts via nanoparticle pore confinement.* Journal of the American Chemical Society, 2012. **134**(50): p. 20457-20465.

[18] Song, S., et al., *Effect of pore morphology of mesoporous carbons on the electrocatalytic activity of Pt nanoparticles for fuel cell reactions.* Applied Catalysis B: Environmental, 2010. **98**(3): p. 132-137.

[19] Balgis, R., et al., *Morphology control of hierarchical porous carbon particles from phenolic resin and polystyrene latex template via aerosol process.* Carbon, 2015. **84**: p. 281-289.

[20] Lowell, S. and J.E. Shields, *Powder surface area and porosity*. Vol. 2. 2013: Springer Science & Business Media.

[21] Bard, A.J. and L.R. Faulkner, *Fundamentals and applications.* Electrochemical Methods, 2001. **2**.

Chapter 3

Effect of Nitrogen Functionalization and Hollow Structure on the Capacitance of Carbon Particles

3.1 Introduction

Electrochemical energy storage systems such as batteries and supercapacitors have been extensively developed in recent decades in response to the demand for renewable and environmentally friendly energy supply systems. Batteries and supercapacitors have different characteristics with respect to their power and energy densities; batteries usually have higher energy densities than supercapacitors, but supercapacitors tend to have higher power densities compared with batteries.[1] However, despite their different characteristics, the development of batteries and supercapacitors is focused on the same objectives: to increase the power densities and energy densities, as well as to extend the cycle life. These objectives are attained in several ways, particularly through the proper selection and fabrication of electrode materials.

Carbonaceous materials have potential as electrodes for energy storage systems because of their excellent electrical conductivity and tunable morphologies, easily yielding the desired nanostructure.[2] Recently, hollow carbon spheres (HCSs) in particular have attracted attention as electrode materials for supercapacitors and batteries because of their high surface area to volume ratio and the unique shell characteristics, which allow effective transport properties.[3]

HCSs are not limited to use as a single material component for batteries and supercapacitor electrodes; they also can be employed as supports to confine an active electrode material for an enhanced overall performance.[4] For example, HCSs are used as shells for metal oxides in supercapacitors to prevent them from agglomeration and reducing direct contact with the electrolyte during charge-discharge.[5] In lithium-sulfur (Li-S) batteries, HCSs are used as confinements for sulfur to prevent the electrode from performance degradation because of a cyclic process of dissolution-redeposition of long-chain lithium polysulfides.[6] In such cases, control of the shell morphology and thickness is necessary not only to create an effective solid-electrolyte contact but also to optimize the solid-state transport of working ions such as Li^+.[7]

Structuring the shell morphology also contributes significantly to an improvement in the capacitance through optimization of the double layer effect. An improved capacitance is particularly important when HCSs are used as a stand-alone material for energy storage devices. The capacitance can be further enhanced by introducing a pseudocapacitive effect, usually by the addition of nitrogen (N) functional groups, preferably pyridinic and pyrrolic types, into the carbon structure.[8] Not only do the nitrogen functional groups improve the overall capacitance, they also enhance the charge-discharge efficiency because of their high electron conductivity.[9, 10]

One of the strategies used to synthesize nanostructured N-doped HCSs is polymerization of a nitrogen-containing carbon source that is stable in solution and free from static hindrance, such as 3-aminophenol, along with subsequent carbonization at a high temperature, between 500 and 1000 °C, depending on the desired degree of carbonization.[11] This route is considered to be more effective than ex-situ doping techniques such as nitridation. Previous studies preferred the utilization of the hydrothermal method over other processes such as chemical vapor deposition for the synthesis of 3-aminophenol-derived HCSs because of the simplicity in operation.[12-14] However, the hydrothermal synthesis route is time-consuming and hence unsuitable for large-scale production.[11] Replacing the hydrothermal polymerization process would significantly reduce the overall synthesis duration of HCSs.

Microwave irradiation is a promising substitute for hydrothermal treatment that has been proven to accelerate the polymerization in the synthesis of polyamides, polyimides, and poly(amide-imide)s, as well as the decomposition of several compounds.[15, 16] The effects of microwave irradiation may vary, depending upon the reaction system. In the typical reactions accelerated by microwave irradiation, the radiation causes a rapid rotation of the dipoles and an increasing number of molecular collisions, which further enhance the reaction rate. Some works also report that microwave-synthesized polymers have a high degree of sphericity.[17]

This study aims to synthesize high-capacitive performance and highly monodisperse HCSs through a synthesis route that is favorable for large-scale production. Microwave irradiation was applied to accelerate the polymerization of 3-aminophenol as a carbon source and formaldehyde, which was followed by a high-temperature carbonization. Hollow structures were formed using polystyrene latex (PSL) as a template. No etching process is required for template removal because PSL thermally decomposes at a temperature of 400 °C.[18, 19] The feasibility of the synthesized HCSs as an energy storage material was evaluated through electrochemical characterization. The adjustment of HCSs shell thickness was very practical,

which further improves the flexibility of the synthesized particles for a broader range of applications.

3.2 Experimental

3.2.1 Synthesis of HCSs

Negatively and positively charged PSL particles were synthesized using a method that has been described elsewhere.[20] An aqueous solution containing 70 mg 3-aminophenol (Sigma Aldrich, St. Louis, MO, USA), 0.3 ml ammonia solution (Kanto Chemical Co. Inc., Tokyo, Japan), 2.5 ml ethanol, PSL particles with controlled charge (ζ-potential = -53.3 mV), and 10 ml ultrapure water was stirred until clear at 30 °C. Four sizes of PSL particles were used separately: 80.4, 135, 375, and 393 nm. The ratio between 3-aminophenol and PSL particles was studied at 1:1, 5:1, 10:1, 15:1, and 20:1. In a separate set of experiments, positively charged PSL particles (ζ-potential = +53.3 mV) were also used. The stirred solution was then heated in a microwave-assisted organic Initiator^{+} (Biotage, Uppsala, Sweden) for typically 30 minutes at 150 °C after the addition of formaldehyde (Kanto Chemical Co. Inc., Tokyo, Japan). To study the effects of microwave irradiation time on particle growth, the experiments were also performed with several heating durations, from 1 second to 20 minutes. The obtained particles were separated from the solution and washed with ultrapure water and ethanol several times to remove the remaining impurities. After being dried at 40 °C, approximately 0.1 gram of the particles was placed into an electric ceramic furnace for carbonization under a nitrogen atmosphere (0.5 L min^{-1}) for 4 hours. The effects of the carbonization temperature on the particle morphology were observed at 550 and 1200 °C to the HCSs prepared with a 3-aminophenol to PSL ratio of 10:1.

3.2.2 Physical characterization

The ζ-potential of a solution containing either 3-aminophenol, PSL particles, or both, was measured using a zetasizer (Zetasizer Nano ZSP, Malvern Instruments Ltd., Malvern, UK). The morphology of the synthesized particles was observed using a field-emission scanning electron microscope (SEM; S-5000, 20 kV, Hitachi High-Tech. Corp., Tokyo, Japan) and transmission electron microscopy (TEM; JEM-2010, 200 kV, JEOL Ltd. Tokyo, Japan). The nitrogen adsorption-desorption ability of the synthesized particles was measured using gas adsorption measurement equipment (BELSORP-max, MicrotracBEL Corp., Osaka, Japan), and the surface area was calculated using the Brunauer-Emmett-Teller (BET) method based on the

N_2 isotherm curve. Fourier-transform infrared (FT-IR) spectroscopy was used to investigate the chemical reactions during the microwave irradiation process (Spectrum one, Perkin Elmer Inc., Waltham, MA, USA). Elemental analysis was carried out using X-ray photoelectron spectroscopy (XPS; PHI Quantera II, Physical Electronics, Chanhassen, MN, USA). Particle size and shell thickness were determined by measuring the diameter of more than 300 randomly selected particles.

3.2.3 Electrode preparation and electrochemical characterization

Positive and negative electrodes were prepared from aluminum foil coated by a 8.1 mg slurry of 91.1 wt% electrode active material, 4.5 wt% acetylene black as a conductive agent, 1.4 wt% carboxymethylcellulose sodium salt as a viscosity controller, and styrene-butadiene rubber (SBR) as a binder. The thickness of the electrode materials was 120 μm while the diameter was 14 mm. An electrochemical cell was formed by assembling 2032 coin-type cells (SS316L; diameter of 20 mm and height of 3.2 mm), filled with electrolyte consisting of 1.4 M triethylmethyl ammonium tetrafluoroborate (TEMA-BF4, Sigma Aldrich, St. Louis, MO, USA) in propylene carbonate after installing a separator between positive and negative electrodes.

Electrochemical characterization was conducted to evaluate the effects of carbon nanostructure on the capacitance and Ohmic resistance of the electrodes. Two-electrode galvanostatic charge and discharge was applied to the electrodes at 3 mA/cm^2 within a voltage window of 0 to 2.5 V using a battery performance evaluation apparatus (BLS 5500-10100m Keisokuki, Instrument Center, Ltd., Osaka, Japan). The capacitance and Ohmic resistance of HCSs were compared with that of N-doped dense and commercial activated carbon (YP-50F, Kuraray Chemical Co. Ltd., Osaka, Japan). Hollow, dense, and activated carbon samples used for the electrochemical characterization are denoted HCS, DCS, and AC, respectively. HCS was prepared with a 3-aminophenol to PSL ratio of 10:1 that underwent calcination at 1200 °C. The DCS sample was prepared using a similar method and under the same calcination temperature to that applied for the synthesis of HCS, except for the exclusion of PSL particles in the synthesis. The durability of HCS was evaluated by applying 1600 charge-discharge cycles at 0.5 A g^{-1}.

Cyclic voltammetry was performed in a potentiostat (HR-301, Hokuto Denko Corp., Tokyo, Japan) using a 3-electrodes configuration. The active material ink was prepared by dispersing HCS (10 mg) in a mixture of ultrapure water (0.95 ml), 2-propanol (0.3 ml; Cica-reagent, Kanto Chemical Co. Inc., Tokyo, Japan), and Nafion® (5 μl; Wako Pure Chemical

Industries Ltd., Osaka, Japan) by ultrasonication. 10 µl of the active material ink was transferred to a polished glassy carbon electrode and allowed to dry. A reversible hydrogen electrode and platinum wire was used as the reference and counter electrode, respectively. The electrolyte was 1 M sodium hydroxide (Kanto Chemical Co. Inc., Tokyo, Japan). The potential sweep was varied by 10, 20, 30, 60, and 100 mV s^{-1} in a potential window between 0 and 0.9 V/RHE.

3.3 Results and Discussion

3.3.1 Formation of carbon shell

The carbon shell formation process was divided into two main steps, i.e., microwave-assisted growth of a cross-linked phenolic shell and calcination in the furnace. The growth of the phenolic shell started immediately after the addition of formaldehyde into the solution of 3-aminophenol, ammonia, and ethanol. Zhao et al. proposed the polymerization mechanisms of 3-aminophenol and formaldehyde based on FT-IR results.[21] Typically, 3-aminophenol and ammonia react with formaldehyde, forming a mixture of addition and condensation compounds such as oligomers. Further reactions cause the oligomers to crosslink, and the degree of crosslinking increases upon heating.

In this study, a surface charge approach was used to explain the growth mechanism of the cross-linked phenolic shell. The changes in the surface charge (ζ-potential) before and after the addition of PSL particles and formaldehyde were evaluated. According to previous studies by our group, the positive ζ-potential of the positively charged PSL particles comes from the amino groups, while the negative one comes from the sulfate group.[20]

Table 3.1. List of ζ-potential (in mV) in the early steps of HCS synthesis

Case	Initial ζ-potential of PSL [mV]	Solution ζ-potential [mV]		
		A	B	C
I	+52.5	-55.5	+10.6	-56.6
II	-47.9	-46.0	-52.7	-52.3

Note:

A. 3-aminophenol and ammonia

B. Solution A after the addition of PSL

C. Solution B after the addition of formaldehyde

Table 3.1 summarizes the ζ-potential of solutions before and after the addition of positively (case I) and negatively (case II) charged PSL particles and formaldehyde. As seen in Table 3.1, the ζ-potential of the ammonia and 3-aminophenol solution, labelled solution A, was negative in both case I and II. In case I, the addition of positively charged PSL particles into solution A increased the ζ-potential to +10.6 mV. However, this value was lower than the initial ζ-potential of PSL particles. This would imply that the surface of PSL particles was partially covered, likely by 3-aminophenol. The presence of N atoms, which are highly electronegative, allowed the amino group of PSL particles to form a hydrogen bond with the hydroxyl groups of 3-aminophenol, as illustrated in **Figure 3.3.1(a)**. According to our previous research, the ζ-potential of phenolic oligomers is highly negative.[22] Therefore, the highly negative ζ-potential in solution C implies that the PSL particle surfaces were fully covered by phenolic oligomers resulting from several addition and condensation reactions between 3-aminophenol and formaldehyde.

Contrary to case I, the ζ-potential of the solution after the addition of negatively charged PSL particles in case II remained negative (Solution B). It is speculated that 3-aminophenol was attached to the surface of the PSL particles through a bond between the amino groups of 3-aminophenol and the sulfate group of PSL particles and the hydroxyl group of 3-aminophenol remained free, as illustrated in **Figure 3.1(b)**. Similar to case I, a negative ζ-potential was also observed in case II after the addition of formaldehyde because 3-aminophenol on the surface of PSL particles transformed into negatively charged oligomers that covered the surface of PSL particles. These results confirmed the reaction mechanisms of carbon shell formation proposed by Zhao et al.[21] The proposed mechanism of shell formation and the chemical bond between 3-aminophenol and PSL particles during the nucleation process are illustrated in **Figure 3.1(c)**.

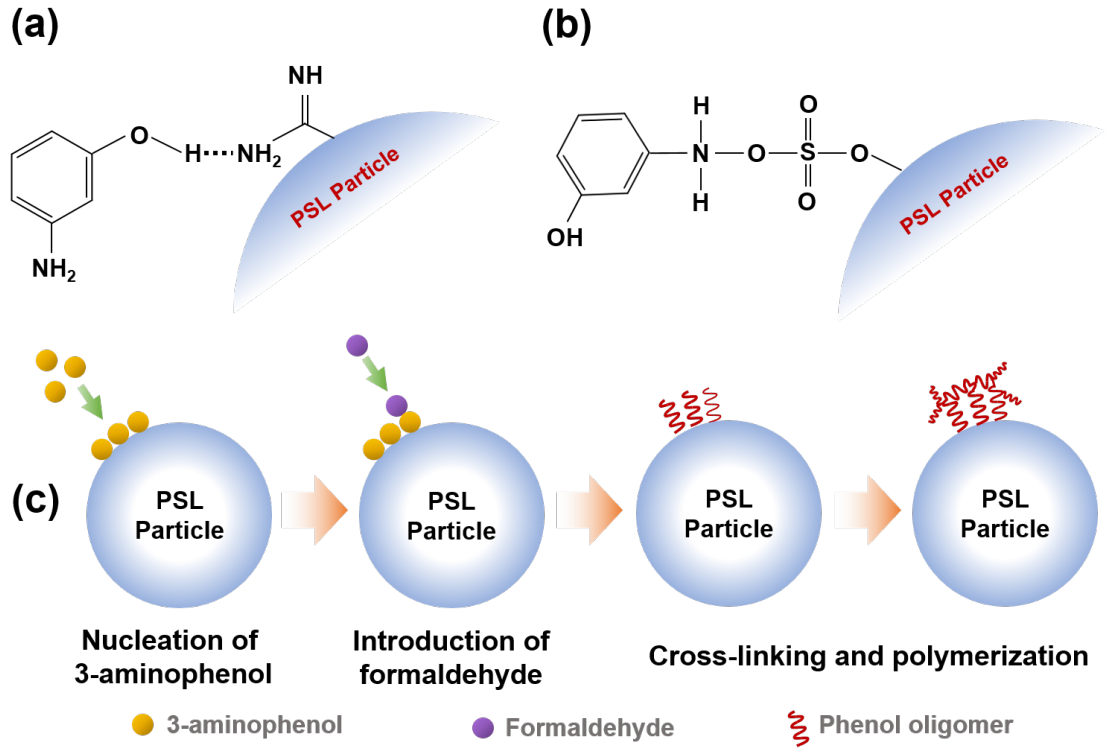

Figure 3.1 Illustration of the chemical bond between (a) 3-aminophenol and positively charged PSL particle, (b) 3-aminophenol and negatively charged PSL particles, and (c) shell growth on the surface of PSL particles

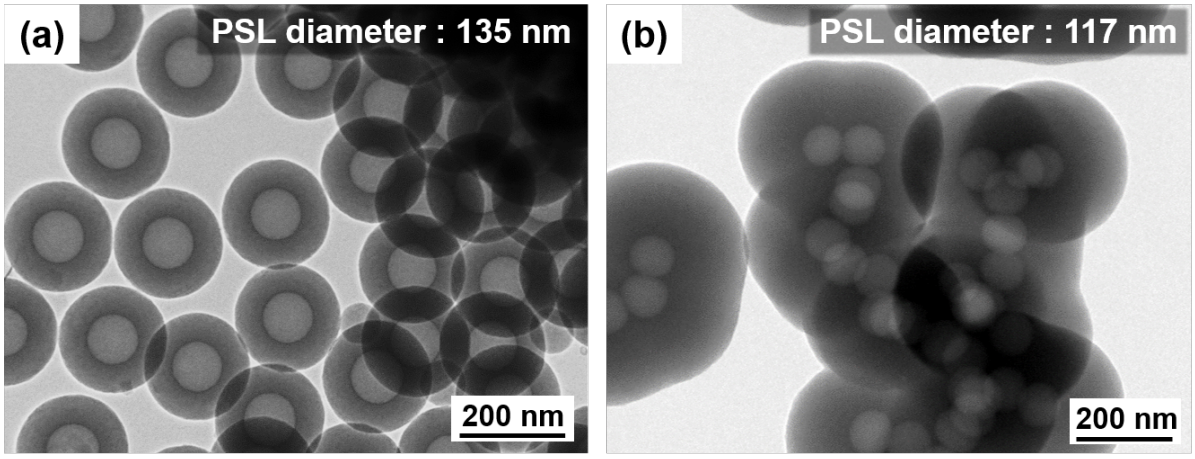

Figure 3.2. TEM images of HCSs prepared using a PSL template with a surface charge of (a) −53.3 mV and (b) 53.4 mV and at a 3-aminophenol to PSL ratio of 10:1

Despite having similar reaction mechanisms for forming the hollow structure, the dispersion and shell thickness of HCSs prepared using a positively charged PSL template were different from those prepared using a negatively charged PSL template. As seen in **Figure 3.2**,

HCSs prepared using the positively charged PSL template tended to have thicker shells compared with those prepared using the negatively charged PSL template. This implies that the electrostatic force between 3-aminophenol monomers and PSL particles from the opposing surface charge attracted more 3-aminophenol monomers to be nucleated on the surface of PSL particles. The aggregated particles indicate that the attractive electrostatic force between the hydroxyl group of 3-aminophenol and the amine group of PSL particles was strong enough to attract many neighboring PSL particles at once during the nucleation. The distance between one PSL particle and another would then decrease; consequently, necking occurred after polymerization.

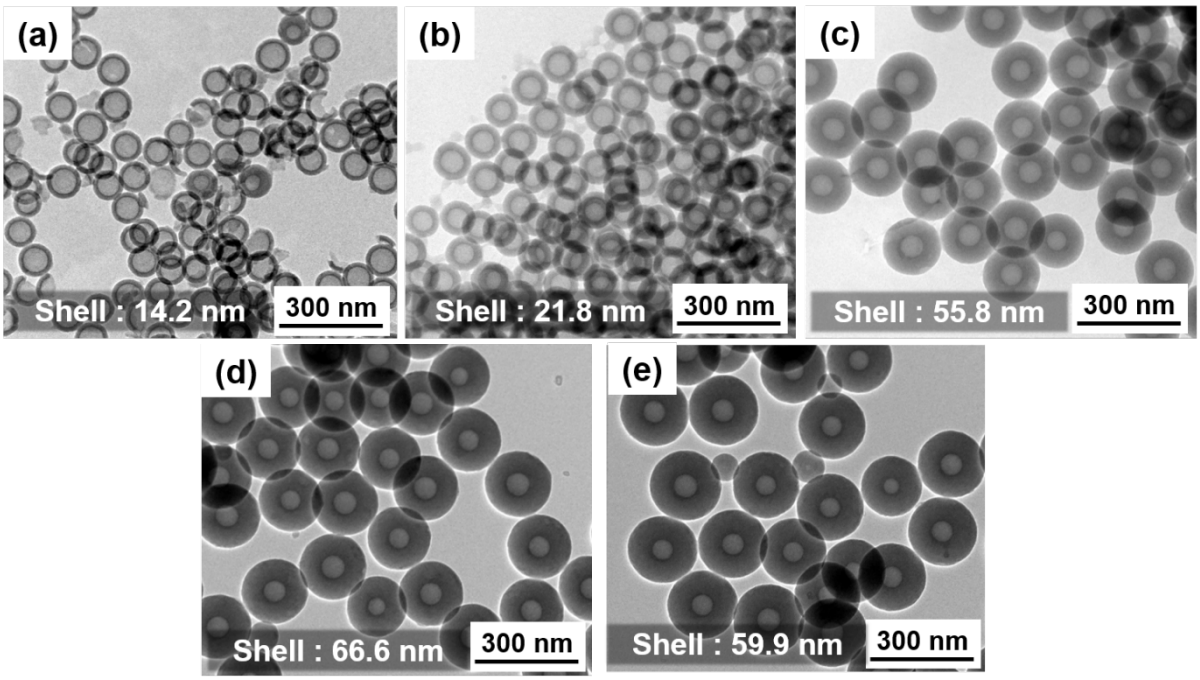

Figure 3.3. TEM images of HCSs prepared at a mass ratio of 3-aminophenol to PSL particles of (a) 1:1, (b) 5:1, (c) 10:1, (d) 15:1, and (e) 20:1. The size of PSL particles was maintained at 63 nm.

Figure 3.3 shows TEM images of HCSs prepared at various 3-aminophenol to PSL mass ratios. At 3-aminophenol to PSL ratios of 1, 5, 10, and 15, all particles were hollow and no dense particles were observed. However, when the ratio of 3-aminophenol to PSL was increased to 20, some dense particles were observed. This phenomena may be explained by a classical thermodynamic consideration of homogeneous and heterogeneous nucleation, with PSL particles as the “foreign bodies” and 3-aminophenol as the nuclei that grows on the surface of the foreign bodies.[23] Following this principle, the nucleation process of 3-aminophenol on

the surface of PSL particles would be determined by the critical energy for heterogeneous nucleation, ΔG_c, as elaborated in Equation (1).[24]

$$\Delta G_c = \Delta G_c^{homo} f(m, x) \quad (1)$$

where ΔG_c^{homo} is the critical energy of homogeneous nucleation, and,

$$x = \frac{R^s kT \ln(1+\sigma)}{2\Omega\gamma_{cf}} \quad (2)$$

R^s, k, and T denote the radius of the foreign body, kinetic constant, and temperature, respectively. Ω and γ_{cf} represent volume per structural unit and step free energy between nuclei and 3-aminophenol solution, respectively. The supersaturation, σ, in Equation (2) is defined as:

$$\sigma = \frac{X_A - X_A^0}{X_A^0} \quad (3)$$

In our system, X_A and X_A^0 represent the actual and equilibrium concentration for the heterogeneous nucleation of 3-aminophenol, respectively. The value of σ may be interpreted as the available driving force for diffusion-controlled heterogeneous nucleation. At 3-aminophenol to PSL ratios of 1, 5, 10, and 15, the driving force was predicted to be sufficient to promote heterogeneous nucleation of 3-aminophenol on the surface of PSL particles.

Meanwhile, at a 3-aminophenol to PSL ratio of 20, the concentration of 3-aminophenol was excessive and the value of X_A^0 was reached. Consequently, the value of σ and x approached 0 and the heterogeneous nucleation of 3-aminophenol was discontinued because of the insufficient driving force. However, the concentration of the remaining 3-aminophenol in the solution was high enough to reach the critical concentration for homogeneous nucleation. The monomers of 3-aminophenol then formed nuclei among themselves, which resulted in dense particles at the end of the nucleation process.

3.3.2 The role of microwave irradiation

The effects of microwave irradiation duration on 3-aminophenol polymerization were observed from the changes in the particle diameter and FT-IR spectra shown in **Figure 3.4**. The particle size was approximately 155 nm after 1 second of microwave irradiation. This was larger than the PSL particles (~77 nm), implying that the nucleation of 3-aminophenol on PSL particles had already occurred and the condensation reaction had started. At this stage, the FT-IR spectra of the particles show weak peaks at 752 and 835 cm^{-1}, which can be assigned to C-H deformation vibration, and at 1089 cm^{-1}, corresponding to C-O-C stretching.[25] A band near 1236 cm^{-1} was also observed, assigned to the stretching of Ar-O-C.[11] The bands at 1436,

1508, and 1618 cm^{-1} correspond to C=C stretching of aromatic rings, while the peak at 2400 cm^{-1} is assigned to N-H stretching of amino groups.[26] The broad bands at 3360 cm^{-1} are possibly the integration of O-H and N-H stretching vibrations.[27]

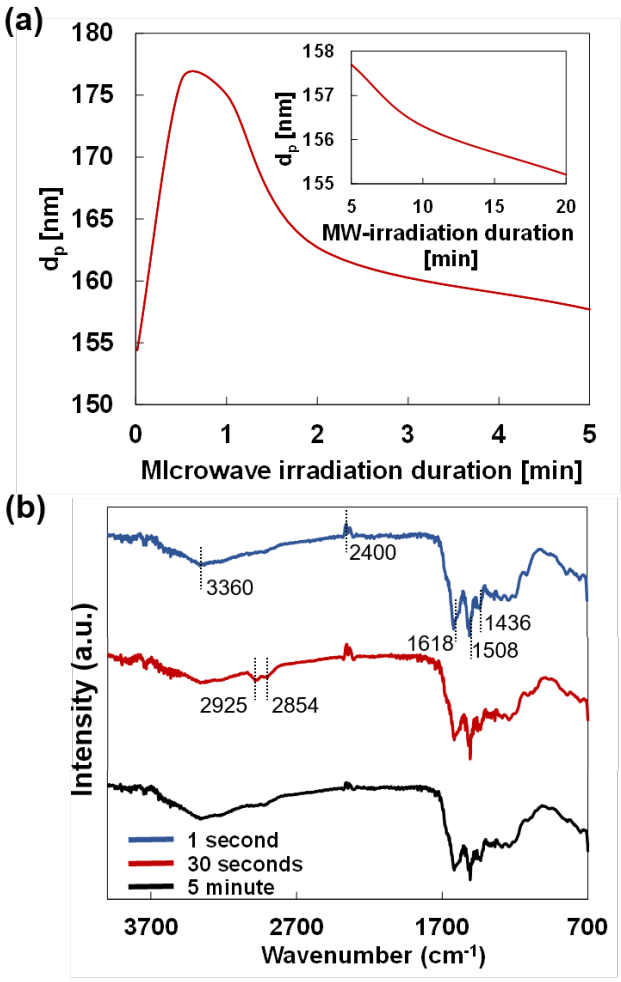

Figure 3.4. (a) Effects of microwave irradiation duration on particle diameter and (b) FT-IR spectra

The particles subsequently grew and reached the maximum size after approximately 30 seconds. The increase in the particle size during this period indicates an on-going cross-linking and polymerization process. The FT-IR spectra show peaks at 2854 and 2925 cm^{-1}, which can be assigned to C-H stretching vibration of $–CH_2–$. This is possibly an indication of dehydration and condensation, which release one molecule of formaldehyde and water.[28] The loss of formaldehyde and water could be the reason for the shrinkage of the particles' sizes from 30 seconds onward, as shown in **Figure 3.4 (a)**. However, the peaks at 2854 and 2925 cm^{-1} disappeared after 5 minutes of microwave irradiation. The FT-IR spectra of the particles after

5 minutes of microwave irradiation is comparable to that resulted from 24-hour hydrothermal heating in a previous work by Zhao et al.[11]

The carbonization process occurred in the electric furnace under nitrogen atmosphere. The total heating duration in the microwave and electric furnace was 4.5 hours, which is more than 50% shorter than that in the hydrothermal process.[11] According to the mass balance calculation, approximately 46.87% and 32.3% of 3-aminophenol was converted to carbon at 550 °C and 1200 °C, respectively. These yields were significantly higher than those of carbon particles that resulted from a spray pyrolysis process of phenolic resin.[29]

3.3.3 Control of shell thickness

Figures **2 (a)** to **(e)** show that the shell thickness of the particles increased as a higher ratio of 3-aminophenol to PSL particles was applied. The increase in the shell thickness occurred because more 3-aminophenol was attached to the surface of PSL particles. According to the heterogeneous nucleation principle, the number of carbon particles, N_c, can be approximated from the number of PSL particles involved in the synthesis, N_{PSL}. It is generally known that the growth of nuclei on the surface of a foreign body depends on distance between the foreign bodies. In the constant cell model, the distance between PSL particles is assumed to be equal. As a consequence of this, nuclei are formed homogeneously on every PSL particle surface and the number of synthesized particles will finally be equal to the number of PSL particles. In actual conditions, however, the PSL particles are distributed randomly despite the applied treatment to homogenize the distribution. As a consequence, the nuclei formation is inhomogeneous and not all PSL particles have nuclei grown on their surface. Therefore, a correction factor of v^* is required to represent the number fraction of PSL particles that have nuclei grown on their surface, as written in Equation (4).[30]

$$N_c \approx v^* N_{PSL} \approx \frac{3v^*}{4\pi}\left(\frac{m}{\rho r^3}\right)_{PSL} \quad (4)$$

where *m, ρ,* and *r* inside the bracket with a subscript PSL denote the mass, density, and radius of PSL particles, respectively. The effect of the 3-aminophenol to PSL ratio on the shell thickness could then be explained by a mass balance principle.

Let us take one particle as the input-output shell balance model. The mass of the carbon shell in one particle, m_{shell}, would be equal to the mass of 3-aminophenol that was converted to one carbon particle, as expressed in Equation (5).

$$m_{shell} = \frac{\alpha m_{ph}}{v^* N_{PSL}} \tag{5}$$

m_{ph} is the mass of 3-aminophenol, while α is the yield (46.87% at 550 °C). m_{shell} is determined by multiplying the volume of the shell by the density of carbon, ρ_c,

$$\frac{\alpha m_{ph}}{v^* N_{PSL}} = \left(\frac{4}{3}\pi r_p^3 - \frac{4}{3}\pi r_h^3\right)\rho_c \tag{6}$$

Because particle radius, r_p, is a summation of the hollow radius, r_h, and shell thickness, r_s, Equation (6) is rearranged to:

$$r_s = \left[\frac{3}{4\pi}\left(\frac{\alpha m_{ph}}{v^* N_{PSL}\rho_c}\right) + r_h^3\right]^{1/3} - r_h \tag{7}$$

A plot of the shell thickness based on the mass balance is shown in **Figure 3.5**. Up to a 3-aminophenol to PSL ratio of 15, the measured shell thicknesses were in accordance with the derivation of mass balance, with a value of v^* estimated to be 0.28. However, the measured shell thickness deviated from the theoretical value at a 3-aminophenol to PSL mass ratio of 20. This deviation may indicate the existence of dense particles because of the excessive concentration of 3-aminophenol. TEM images in **Figure 3.3 (e)** show that the dense particles had small diameters. Consequently, the particles' size distributions became much wider at a 3-aminophenol to PSL ratio of 20.

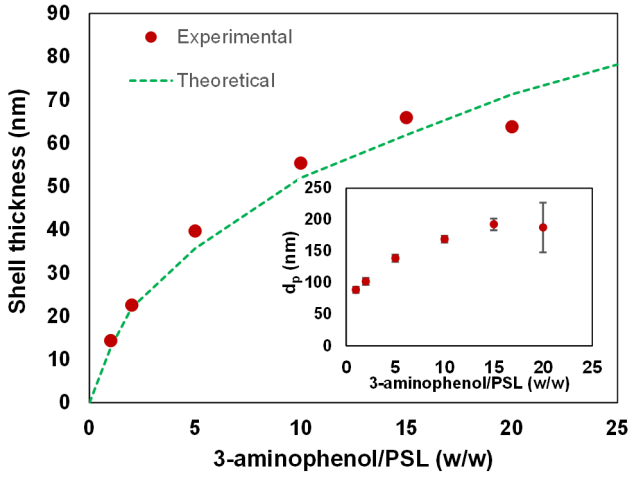

Figure 3.5. Correlation between 3-aminophenol/PSL ratio and shell thickness. Inset is the particle diameters respective to 3-aminophenol/PSL ratio

3.3.4 Effects of PSL particle size

The effects of PSL particle size on the hollow diameter were evaluated at PSL particle sizes of 80.4, 135, 357, and 393 nm. TEM images in **Figure 3.6(a)** to **(d)** show that the hollow diameter increased as larger PSL particles were applied. However, the final hollow diameter was smaller than the PSL size, as shown by the graph presented in **Figure 3.6(e)**, indicating that the hollow shrank after PSL decomposition at 400 °C. The tendency of the pores to shrink is aligned with our previous report, in which the space left by decomposed PSL would shrink during carbonization because of the shrinkage of the solid structure.[29] However, in the current case, the hollow ratio, defined as the ratio between the hollow and PSL diameter, was found to be dependent on the PSL size, i.e., 72.4%, 76.3%, 79.8%, and 81.4% for PSL sizes of 80, 135, 357, and 393 nm, respectively. A higher hollow ratio indicates that the hollow experiences less shrinkage with respect to the initial PSL particle size.

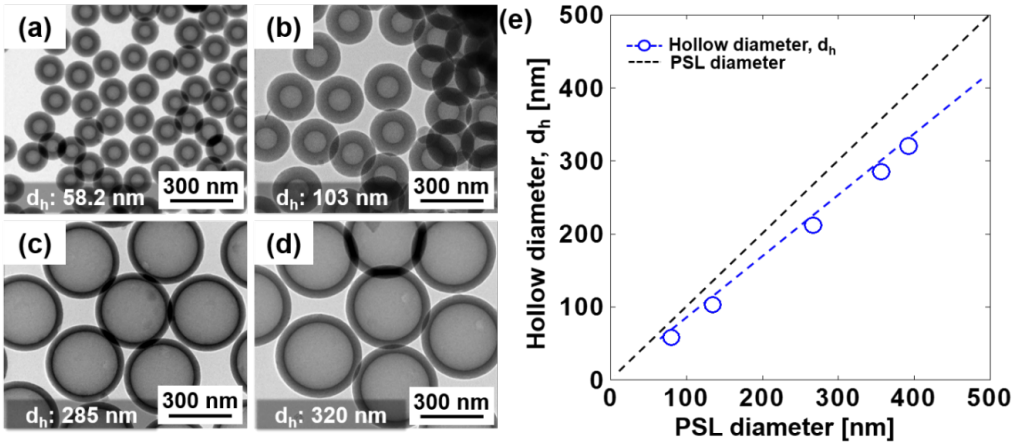

Figure 3.6. HCSs prepared using PSL particles with a size of (a) 80.4, (b) 135, (c) 357, and (d) 393 nm. (e) Correlation between PSL particles and final hollow diameter

The inconstant values of hollow ratio indicates that the shell shrank in the polar (θ) and azimuthal (φ) directions, as illustrated in **Figure 3.7**. Consequently, the particles prepared using large PSL particles experienced less shrinkage because the shrinkage of the hollow in the radial (r) direction was less significant compared with the initial hollow size.

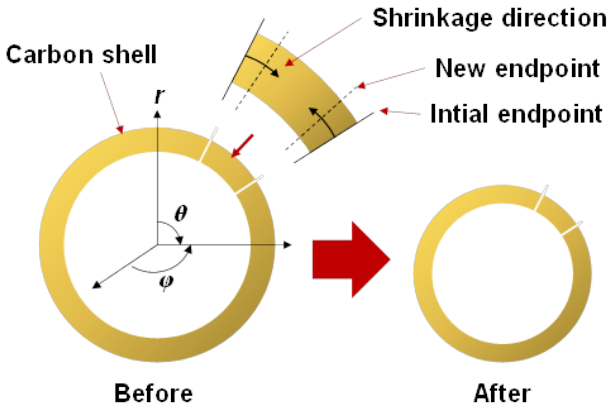

Figure 3.7 Cross-sectional illustration of shell shrinkage during carbonization

3.3.5 Effects of carbonization temperature

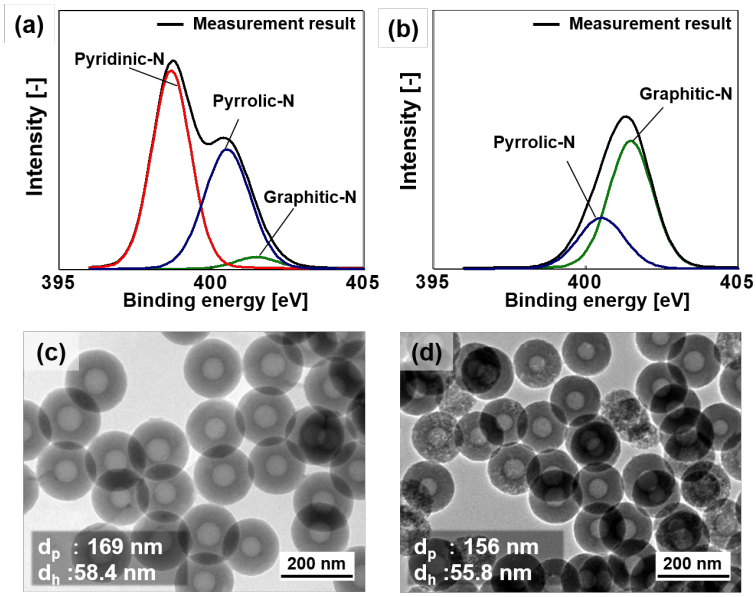

Figure 3.8. XPS spectra and TEM images of HCSs prepared at (a, c) 550 and (b, d) 1200 °C

The effects of calcination temperature on the shell morphology and nitrogen content were evaluated at 550 °C and 1200 °C. As summarized in **Table 3.2**, calcination at 550 °C was found to form micropores with a size of ~0.68 nm, possibly through the release of gasses during carbonization and PSL decomposition. A specific surface area of 365 m^2 g^{-1} was calculated based on the N_2 adsorption-desorption isotherm, which may be attributed to the presence of micropores. The elemental analysis shows that a nitrogen content of 15.62% was observed in

the HCSs. This amount is significantly higher than that in most reported nitrogen-containing carbon particles.[31] Despite the high nitrogen content, the carbon content was still maintained at a high level compared with recently reported HCSs.[32] In the XPS spectra for nitrogen compounds (**Figure 3.8 (a) and (b)**), two major peaks were observed, at ~398 and 400.5 eV, corresponding to pyridinic and pyrrolic nitrogen, respectively.[33] These two types of nitrogen are preferable for increasing the pseudocapacitance. Gaussian fitting of the high-resolution XPS spectra also gave one more peak at ~401.2 eV, which corresponds to quaternary or graphitic nitrogen.

Table 3.2. Elemental composition and specific surface area of HCSs

Calcination temperature [°C]	Elemental composition [%]				Specific surface area [$m^2 g^{-1}$]
	C	H	O	N	
550	74.66	2.72	7.00	15.62	365
1200	95.30	0.19	1.65	2.86	772

Increasing the calcination temperature to 1200 °C caused the particles to further shrink, as shown in the TEM images in **Figure 3.8 (c)** and **(d)**. The average hollow diameter was 4.4% smaller than that of the HCSs calcined at 550 °C. In addition, some mesopores were present in the shell. The N_2 adsorption-desorption test shows that the specific surface area of the HCSs heated at 1200 °C was two times higher than that of HCSs heated at 550 °C, which implies that new micro- and mesopores were formed upon heating. This is confirmed by the pores size distribution curves (**Figure 3.9**) that indicate the formation of pores having a size of approximately 1 nm and the broadening of the mesopores distribution curve after heating at 1200 °C. The increase in the surface area and the reduction in hollow diameter support the previous hypothesis that the shrinkage of the carbon shell was anisotropic in the θ and φ directions.

In addition to increasing the specific surface area, calcination at 1200 °C also significantly reduced the nitrogen content, from 15.62% to 2.86%. The peak of pyridinic nitrogen disappeared in the XPS spectra and the peak of pyrrolic nitrogen became lower than that of quaternary nitrogen. The thermal stability of nitrogen functional groups depends on the

binding energy.[34] Therefore, pyridinic nitrogen, which has the lowest binding energy, experienced the most severe depletion in this study.

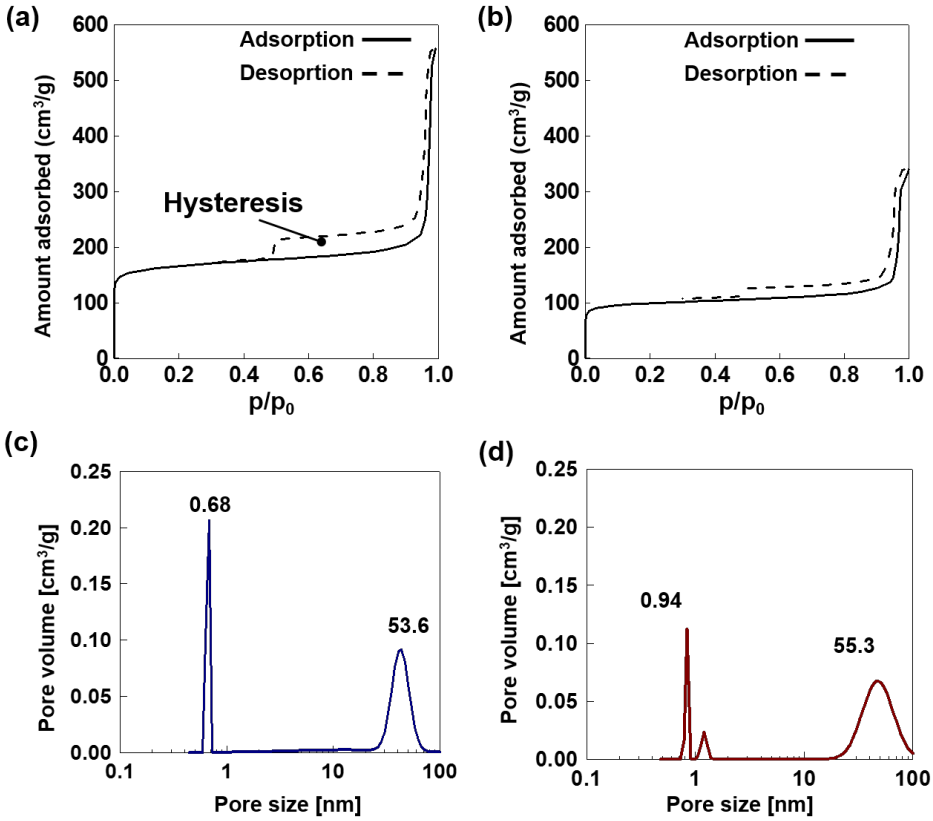

Figure 3.9. N_2 adsorption-desorption isotherm curves of HCSs prepared at (a) 550 and (b) 1200 °C and pores size distribution of HCS prepared at (a) 550 and (d) 1200 °C

3.3.6 Electrochemical performance

The charge discharge curves of HCS, DCS, and AC are provided in **Figure 3.10(a)**, while the corresponding capacitance and Ohmic resistance of each sample are summarized in **Table 3.3**. Considering the importance of having a high capacitance in a small volume for a compact-sized supercapacitor, the capacitance is expressed as volume-specific (C_{vol}, F cm^{-3}). As the most widely used material for supercapacitors, AC delivered a C_{vol} of 13.9 F cm^{-3}. This value was the lowest among the samples. Although the surface area of AC is significantly high, the pore size distribution in AC is rarely optimum because of the poor activation process. Consequently, only certain parts of AC can be optimized for a double-layer capacitor.

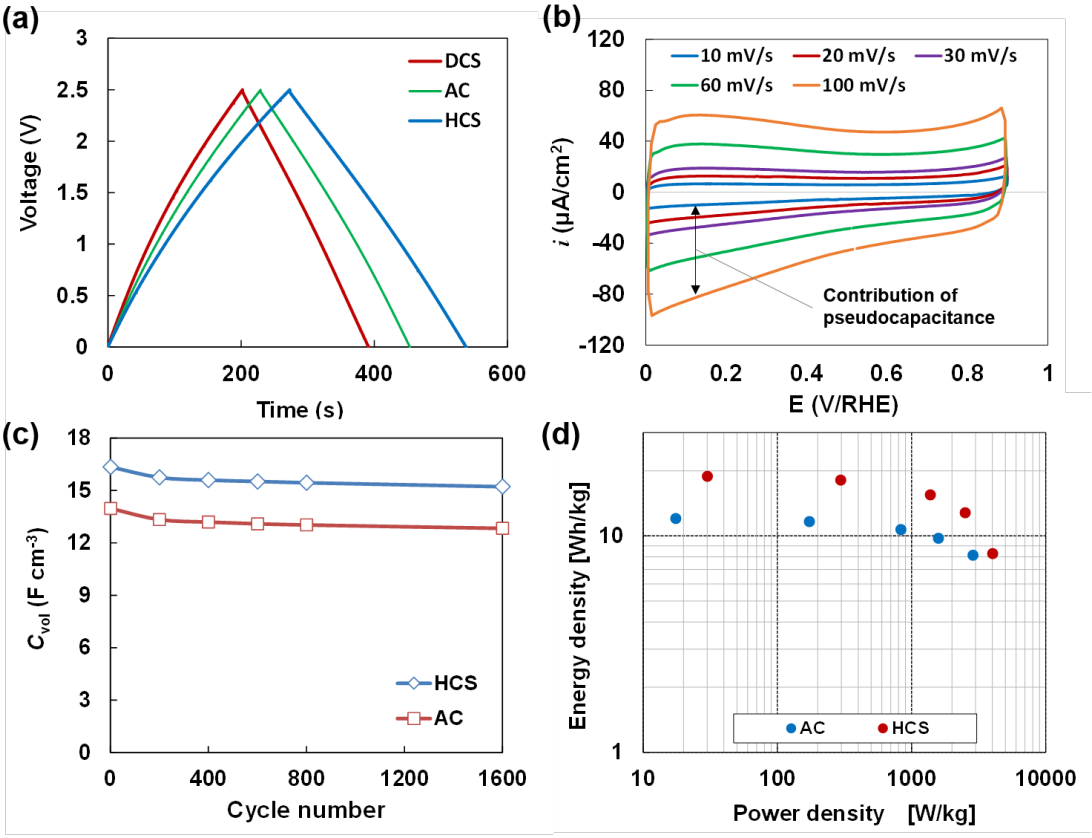

Figure 3.10. (a) Charge-discharge curve at 0.5 A g^{-1}, (b) cyclic voltammetry of HCS in 1M KOH, (c) cyclic performance of HCS and AC, (d) and Ragone plot of HCS and AC

Conversely, the C_{vol} was higher for DCS (14.9 F cm^{-3}) despite having low BET surface area. The fact that DCS had significantly lower surface area than AC implies that the N-doping contributed to improving the capacitance of DCS. The presence of N atoms also increased the electrical conductivity of DCS, indicated by the considerably lower Ohmic resistance than that for AC.

Table 3.3. Summary of the electrochemical performance of AC, DCS, and HCS

Carbon type	BET surface area [m^2 g^{-1}]	Specific capacitance [F cm^{-3}]	Electrode Resistance [Ω]
HCS	**772**	**16.3**	**4.1**
DCS	**551**	**14.9**	**4.0**
AC	**1569**	**13.9**	**6.4**

The N-induced capacitance is thought to be higher when the surface area is increased, and this was confirmed by the C_{vol} exhibited by HCS. Of all carbon electrodes observed in the electrochemical analysis, HCS delivered the highest C_{vol} (16.3 F cm^{-3}), as its BET surface area was 40% higher than that of DCS. The Ohmic resistance of HCS was kept low while the C_{vol} was enhanced, implying that N-doped HCSs are favorable for supercapacitor applications.

The cyclic voltammograms of HCS presented in **Figure 3.10(b)** show a quasi-rectangular shape with humps, indicating that the observed capacitance comes from a combination of the electrical double layer capacitance and Faradaic pseudocapacitance. Since the curves were closer to the rectangular shape, the electrical double layer capacitance is predicted to be dominant. The hollow structure is believed to improve the electrical double layer capacitance, as being confirmed by the wider double layer region of HCS compared to that of DCS (**Figure 3.11**). The hollow structure in HCS likely promoted better intrusion of the electrolyte to the inner parts of the particles, hence allowing an effective contact between the electrolyte and the internal surfaces of the particles. This furthermore enhanced the effective active surface area for the charge storage in the double layer.

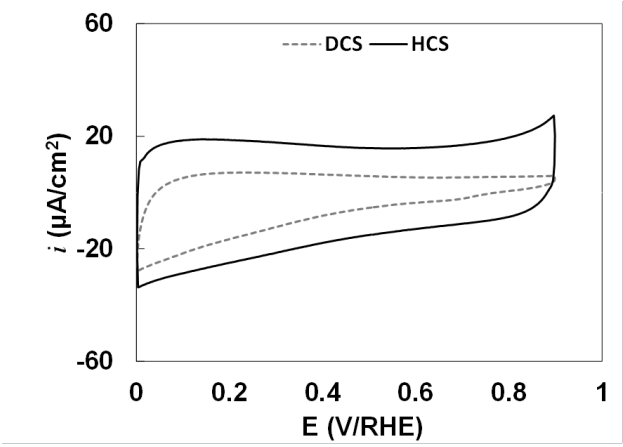

Figure 3.11. Cyclic voltammogram of N-doped dense carbon sphere (DCS) and N-doped hollow carbon spheres (HCS) at 30 mV s^{-1}

The quasi-rectangular shape of the voltammogram was maintained even when a potential sweep as high as 100 mV/s was applied, showing good electrical double layer properties. However, the area under the humps became wider as higher potential sweep was applied, indicating the contribution of the pseudocapacitance that may be expected from N-doping.

HCS was able to maintain 93.1% of its specific capacitance after 1600 charge-discharge cycles, as shown in Figure 6(c). This value was slightly higher than that exhibited by AC, which

was 91%. The power densities (P, W kg^{-1}) and energy densities (E, Wh kg^{-1}) were calculated from the charge-discharge curves by equation (8) and (9) and are depicted in a Ragone plot (Figure 6(d)).

$$E = (C\Delta V^2)/2 \quad (8)$$

$$P = E/t \quad (9)$$

C is mass-specific capacitance (F g^{-1}), ΔV is the potential window of discharge (V), and t is time (s). According to the Ragone plot, HCS was able to deliver higher energy and power densities compared to AC. This would indicate that HCS was able to store higher energy than that AC did, even at the high charge-discharge rates. This particular characteristic is highly expected for supercapacitors.

3.4 Conclusions

High-nitrogen content HCSs with precisely controllable shell thicknesses (14.2–66.6 nm) and particle size (58.2–320 nm) were synthesized by a microwave-assisted polymerization and carbonization process from 3-aminophenol as a carbon source and PSL particles as a template. The growth of the shell on the PSL particles involved the heterogeneous nucleation of 3-aminophenol, which can be explained by the classical heterogeneous nucleation principle. The nitrogen content in the HCSs prepared at 550 °C was 15.62%, higher than that in most reported HCSs. Template size and concentration had a significant role in determining the morphology of the HCSs, including shell thickness and particle size. The shell thickness and particle size could be adjusted by changing the 3-aminophenol/PSL ratio and PSL particle size, respectively. The synthesis was accelerated by the microwave irradiation which shortened the synthesis time by 50% from that required by the hydrothermal synthesis route. The synthesized HCSs took the advantage of N-doping, indicated by their high capacitive performance (about 17.3% higher than that of commercial activated carbon) and a significantly suppressed Ohmic resistance.

3.5 References

[1] Winter, M. and R.J. Brodd, *What are batteries, fuel cells, and supercapacitors?* Chemical reviews, 2004. **104**(10): p. 4245-4270.

[2] Bhattacharjya, D., et al., *High performance supercapacitor prepared from hollow mesoporous carbon capsules with hierarchical nanoarchitecture.* Journal of Power Sources, 2013. **244**: p. 799-805.

[3] Lai, X., J.E. Halpert, and D. Wang, *Recent advances in micro-/nano-structured hollow spheres for energy applications: from simple to complex systems.* Energy & Environmental Science, 2012. **5**(2): p. 5604-5618.

[4] You, B., et al., *Easy synthesis of hollow core, bimodal mesoporous shell carbon nanospheres and their application in supercapacitor.* Chemical Communications, 2011. **47**(45): p. 12364-12366.

[5] He, C., et al., *Carbon-encapsulated Fe3O4 nanoparticles as a high-rate lithium ion battery anode material.* ACS nano, 2013. **7**(5): p. 4459-4469.

[6] Jayaprakash, N., et al., *Porous Hollow Carbon@ Sulfur Composites for High‐Power Lithium–Sulfur Batteries.* Angewandte Chemie, 2011. **123**(26): p. 6026-6030.

[7] Yang, S., et al., *Nanographene‐constructed hollow carbon spheres and their favorable electroactivity with respect to lithium storage.* Advanced Materials, 2010. **22**(7): p. 838-842.

[8] Qie, L., et al., *Nitrogen-Doped Porous Carbon Nanofiber Webs as Anodes for Lithium Ion Batteries with a Superhigh Capacity and Rate Capability.* Advanced Materials, 2012. **24**(15): p. 2047-2050.

[9] Xu, B., et al., *Sustainable nitrogen-doped porous carbon with high surface areas prepared from gelatin for supercapacitors.* Journal of Materials Chemistry, 2012. **22**(36): p. 19088-19093.

[10] Lee, Y.-H., K.-H. Chang, and C.-C. Hu, *Differentiate the pseudocapacitance and double-layer capacitance contributions for nitrogen-doped reduced graphene oxide in acidic and alkaline electrolytes.* Journal of Power Sources, 2013. **227**: p. 300-308.

[11] Zhao, J., et al., *A template-free and surfactant-free method for high-yield synthesis of highly monodisperse 3-aminophenol–formaldehyde resin and carbon nano/microspheres.* Macromolecules, 2012. **46**(1): p. 140-145.

[12] Lei, Z., Z. Chen, and X. Zhao, *Growth of polyaniline on hollow carbon spheres for enhancing electrocapacitance.* The Journal of Physical Chemistry C, 2010. **114**(46): p. 19867-19874.

[13] Su, F., et al., *Hollow carbon spheres with a controllable shell structure.* Journal of Materials Chemistry, 2006. **16**(45): p. 4413-4419.

[14] Zheng, G., et al., *Interconnected hollow carbon nanospheres for stable lithium metal anodes.* Nature nanotechnology, 2014. **9**(8): p. 618-623.

[15] Hoogenboom, R. and U.S. Schubert, *Microwave‐Assisted Polymer Synthesis: Recent Developments in a Rapidly Expanding Field of Research.* Macromolecular Rapid Communications, 2007. **28**(4): p. 368-386.

[16] Langa, F., et al., *Microwave irradiation: more than just a method for accelerating reactions.* Contemporary organic synthesis, 1997. **4**(5): p. 373-386.

[17] Wiesbrock, F., R. Hoogenboom, and U.S. Schubert, *Microwave‐assisted polymer synthesis: state‐of‐the‐art and future perspectives.* Macromolecular Rapid Communications, 2004. **25**(20): p. 1739-1764.

[18] Balgis, R., et al., *Aerosol synthesis of self-organized nanostructured hollow and porous carbon particles using a dual polymer system.* Langmuir, 2014. **30**(38): p. 11257-11262.

[19] Ogi, T., A.B.D. Nandiyanto, and K. Okuyama, *Nanostructuring strategies in functional fine-particle synthesis towards resource and energy saving applications.* Advanced Powder Technology, 2014. **25**(1): p. 3-17.

[20] Nandiyanto, A.B.D., et al., *Size- and charge-controllable polystyrene spheres for templates in the preparation of porous silica particles with tunable internal hole configurations.* Chemical Engineering Journal, 2014. **256**(0): p. 421-430.

[21] Zhao, J., et al., *Facile surfactant-free synthesis and characterization of Fe 3 O 4@ 3-aminophenol–formaldehyde core–shell magnetic microspheres.* Journal of Materials Chemistry A, 2014.

[22] Balgis, R., et al., *Morphology control of hierarchical porous carbon particles from phenolic resin and polystyrene latex template via aerosol process.* Carbon, 2015. **84**(0): p. 281-289.

[23] Zhang, F., et al., *Direct Observations of Three Nucleation/Growth Processes of Charge-Stabilized Dispersion Polymerizations with Varying Water/Methanol Ratios.* The Journal of Physical Chemistry B, 2010. **114**(34): p. 10970-10978.

[24] Fletcher, N., *Size effect in heterogeneous nucleation.* The Journal of Chemical Physics, 1958. **29**(3): p. 572-576.

[25] Rivas, B., et al., *Synthesis, characterization, and properties of poly (2-and 3-aminophenol) and poly (2-and 3-aminophenol)-Cu (II) materials.* Polymer Bulletin (Berlin), 2002. **49**(4): p. 257-264.

[26] Lady, J., R. Adams, and I. Kesse, *A study of thermal degradation and oxidation of polymers by infrared spectroscopy. Part I. Experimental technique and butylated melamine formaldehyde and urea formaldehyde.* Journal of Applied Polymer Science, 1960. **3**(7): p. 65-70.

[27] Merline, D.J., S. Vukusic, and A.A. Abdala, *Melamine formaldehyde: curing studies and reaction mechanism.* Polymer Journal (Tokyo, Japan), 2013. **45**(4): p. 413-419.

[28] Grenier-Loustalot, M.-F., et al., *Phenolic resins: 1. Mechanisms and kinetics of phenol and of the first polycondensates towards formaldehyde in solution.* Polymer, 1994. **35**(14): p. 3046-3054.

[29] Arif, A.F., et al., *Experimental and theoretical approach to evaluation of nanostructured carbon particles derived from phenolic resin via spray pyrolysis.* Chemical Engineering Journal, 2015. **271**(0): p. 79-86.

[30] Nogi, K., M. Naito, and T. Yokoyama, *Nanoparticle technology handbook*. 2012: Elsevier.

[31] Fiset, E., et al., *Comparison of melamine resin and melamine network as precursors for carbon electrodes.* Carbon, 2015. **81**: p. 239-250.

[32] Kim, S.Y., et al., *Nickel oxide encapsulated nitrogen-rich carbon hollow spheres with multiporosity for high-performance pseudocapacitors having extremely robust cycle life.* Energy & Environmental Science, 2015. **8**(1): p. 188-194.

[33] Yu, J., et al., *Simple fabrication of an ordered nitrogen-doped mesoporous carbon with resorcinol–melamine–formaldehyde resin.* Microporous and Mesoporous Materials, 2014. **190**: p. 117-127.

[34] Ghosh, K., et al., *Tailoring the field emission property of nitrogen-doped carbon nanotubes by controlling the graphitic/pyridinic substitution.* Carbon, 2010. **48**(1): p. 191-200.

Chapter 4

Beyond carbon: Magnèli phases titanium oxide (TiO_x) Nanoparticles

4.1 Introduction

Substoichiometric titanium oxides, chemical formula Ti_nO_{2n-1} (n = 4–9), are often referred to as Magnéli phase TiO_x and have attracted much recent attention because of growing demand for conductive materials. Magnéli phase TiO_x was studied for the first time in the 1950s by the group of Arne Magnéli following the construction of a phase diagram of a titanium-oxygen system by De Vries et al.[1] The electrical properties of these materials were then studied by Bartholomew et al., revealing a semiconductor-to-metal transition at certain temperatures and a decrease in conductivity with an increase in oxygen content.[2] Because of the oxygen deficiency, which results in delocalized electrons in the *d* band, some crystallographic shear structures are regularly introduced in the rutile structure and act as a good electron pathway. Therefore, Magnéli phase TiO_x has a high electrical conductivity that is comparable to carbon.[3] However, its advantage over carbon is that it is known to be durable in electrochemically oxidizing environments.[4, 5]

In recent years, several efforts have been devoted to synthesizing Magnéli phase TiO_x, typically by the reduction of rutile titania (TiO_2) under high temperatures between 600 and 1000 °C. According to the titanium-oxygen system phase diagram, this is the simplest pathway to obtain Magnéli phase TiO_x. Commonly employed reducing agents include carbon,[6, 7] zirconium,[8] and hydrogen (H_2) or ammonia.[9, 10] These reduction methods have been proven to effectively synthesize single Magnéli phase TiO_x, often Ti_4O_7 which has the highest conductivity among all Magnéli phases.[11] However, the high reduction temperature promotes sintering, which usually starts at approximately 700 °C or lower for TiO_2 nanoparticles (NPs).[12] Because of heavy sintering, the diameter of the resulting TiO_x particles commonly range from 500 nm to 1 μm, with surface areas of approximately 25 $m^2 g^{-1}$ or lower. Considering that a high specific surface area is important in many applications, improvement in the surface area of the synthesized Magnéli phase TiO_x becomes a challenge. One popular approach to increase the surface area is by reducing the particle sizes to the nano scale. Nano sizes also enable the particles to be effectively packed, hence reducing the contact

resistance between particles. In light of this, Ioroi and his group made several attempts to reduce the TiO_x particles size, e.g., by employing pulsed UV laser irradiation or mechanical grinding.[5, 13] However, the surface areas of the resulting particles were still below 20 $m^2 g^{-1}$, although the particle diameter was reduced to approximately 70 nm. Another synthesis approach carried out by Portehault et al. was a sol-gel method to synthesize monoliths consisting of TiO_x clusters in a carbon matrix, resulting in a surface area as high as 400 $m^2 g^{-1}$.[14] Although the carbon matrix contributed to a high surface area, the proportion of carbon was very high whereas TiO_x NPs, with their absence or minimum presence of a carbon matrix, are favorable for improved durability.

The present work reports a successful synthesis of chain-structured Magnéli phases TiO_x NPs using an induction thermal plasma method. To date, this is the first report on the synthesis of Magnéli phases TiO_x NPs under 30 nm in diameter. The same synthesis methods have previously been used for the synthesis of α"-$Fe_{16}N_2/Al_2O_3$ core-shell[15] and various metal oxide NPs.[16] Conductivity of the synthesized-TiO_x NPs' is analyzed based on the crystal structure. Their electrochemical stability in oxidizing environment is studied to assess the feasibility of the plasma-synthesized TiO_x NPs application as conductive materials in many devices.

4.2 Experimental

Three samples of Magnéli phases TiO_x were synthesized using an RF induction thermal plasma method that has been reported in detail elsewhere.[16] Typically, a precursor suspension was made by dispersing rutile TiO_2 particles with an average diameter ($d_{p,avg}$) of 2 μm (Nisshin Engineering Inc., Tokyo, Japan) into a water-isopropyl alcohol (IPA) mixture. The mass ratio between TiO_2, IPA, and water was 43:43:14, 42:42:16, and 39:39:22 for TiO_x-A, TiO_x-B, and TiO_x-C, respectively. **Figure 4.1** shows a schematic illustration of the experiment. The suspension was then fed into a plasma reactor with argon (Ar) used as both the plasma and carrier gas (**Figure 4.1(a)**). To improve the conductivity, a set of thermal conditioning experiments was performed to the as-synthesized samples (**Figure 4.1(b)**). The sample NPs were first pelletized by applying 50 MPa pressure to 0.5 g of the powder in a pelletizing template. The pellet, having dimensions of 15 mm in diameter and 1 mm in thickness, was then heated under 3% H_2 with an argon balance in a vacuum furnace (μBF, Koyo Thermo Systems Co., Ltd., Nara, Japan) for 1 hour.

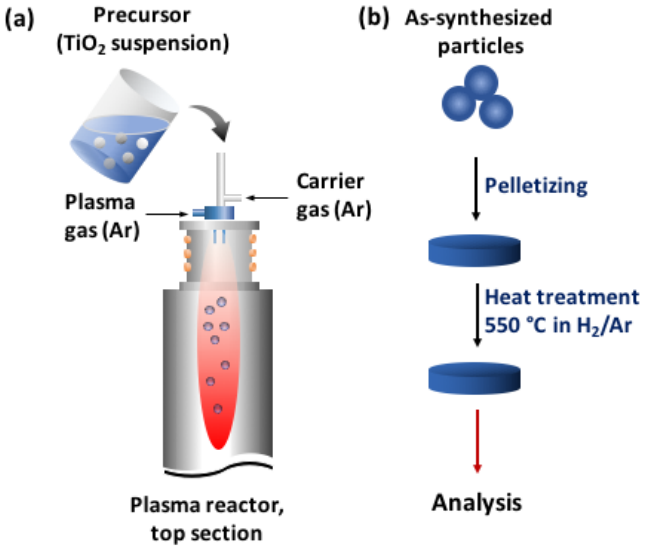

Figure 4.1. Illustration of (a) TiO_x NP preparation using RF induction thermal plasma method, and (b) post-synthesis heat treatment to improve the electrical conductivity.

The morphological structure of the particles was observed using a field-emission scanning electron microscope (SEM; S-5000, 20 kV, Hitachi High-Tech. Corp., Tokyo, Japan) and transmission electron microscope (TEM; JEM-2010, 200 kV, JEOL Ltd., Tokyo, Japan). The crystal structures of all samples were evaluated using X-ray diffraction (XRD; Bruker D2 Phaser, Bruker AXS GmbH, Karlsruhe, Germany), while the oxidation state of the particles was examined using X-ray Adsorption Fine Structure (XAFS; BL5S1, Aichi Synchrotron Radiation Center, Seto, Japan). Anatase TiO_2 and Ti_2O_3 (Sigma Aldrich, St. Louis, MO, USA) were used as the reference for XAFS analysis. Semi-quantitative analysis on the chemical structure composition was performed using Diffrac.Eva 3.0 software (Bruker AXS GmbH, Karlsruhe, Germany) based on the XRD spectral intensities. Based on the N_2 adsorption ability (BELSORP-max, MicrotracBEL Corp., Osaka, Japan), the surface areas of the particles were calculated by the Brunauer-Emmett-Teller (BET) method. The surfaces of the particles were evaluated using Fourier-transform infrared (FT-IR) spectroscopy (Spectrum One, Perkin Elmer Inc., Waltham, MA, USA). The electrical resistivity of the sample before and after heat-treatment was measured using the four-probe method (Loresta-GP, Mitsubishi Chemical Analytech Co., Ltd., Kanagawa, Japan). For better accuracy, the electrical resistivity of each sample was measured three times to three different pellets. The measurement was conducted

within a short period in a controlled ambient, suppressing the effect of pellet inhomogeneity and the difference in the atmospheric conditions.

TiO_x NPs stability in an oxidizing environment was evaluated by electrochemical analytical methods using a potentiostat (HR-301, Hokuto Denko Corp., Tokyo, Japan) in a 3-electrode configuration. Platinum wire and a reversible hydrogen electrode (RHE) was used as the counter and reference electrode, respectively. Cyclic voltammetry and potentiodynamic scan were conducted in 1 M HCl solution (Cica-reagent, Kanto Chemical Co. Inc., Tokyo, Japan) saturated with oxygen with a potential sweep of 50 mV s^{-1}. The potential window for cyclic voltammetry and potentiodynamic scan was 0 to 1.4 V/RHE and 0 to 1.5 V/RHE, respectively. 1.4 V/RHE is the maximum theoretical potential of a fuel cell during start and stop conditions. This potential was chosen as the cyclic voltammetry reverse potential to represent a severe environment that might be imposed to TiO_x NPs in their application as conductive material. The active material ink was prepared by dispersing TiO_x NPs (2.64 mg) in a mixture of ultrapure water (0.95 ml), 2-propanol (0.3 ml; Cica-reagent, Kanto Chemical Co. Inc., Tokyo, Japan), and Nafion® (5 µl; Wako Pure Chemical Industries Ltd., Osaka, Japan) in an ultrasonic bath. The corrosion rate (r) was calculated based on the exchange current density using a derivation of Faraday's equation (Eq. 1). i, a, n, and F is exchange current density, average molecular weight of TiO_x, number of electrons, and Faraday constant, respectively.

$$r = \frac{i\mathrm{M}}{n\mathrm{F}} \qquad (1)$$

4.3 Results and Discussion

Electron microscopy images of the as-synthesized particles are shown in **Figure 4.2**. According to these images, the particles in all three samples had chain-like structures with a high degree of sphericity, as may be expected from a gas-phase synthesis method.[17] Topological measurement on the NPs shows a $d_{p,avg}$ of 20.9 nm, 26.8 nm, and 16.9 nm for TiO_x-A, TiO_x-B, and TiO_x-C, respectively. The size distribution of the NPs was narrow, indicated by a standard deviation of 5.7 nm, 6.9 nm, and 5.0 nm for TiO_x-A, TiO_x-B, TiO_x-C, respectively. Images of high-resolution (HR) TEM analysis show a non-uniform lattice structure in all samples. The distance between the lattices are inhomogeneous, even between one lattice pair and its neighboring pair. Although it is normal for one Magnéli structure to have different distances between the Ti atoms, dependent on the type of Ti atom pairing,[18]

variations in the lattice distance of these samples were random. Some lattice distances are very wide, for example, 4.75 Å, which is not associated to a specific Magnéli phase, or 4.73 Å, which might refer to the [002] crystal of Ti_3O_5 (**Figure 4.2b**). Some other lattice distances may more easily be associated with some Magnéli phases, for example, 2.11 Å, which is associated with the [202] crystal of Ti_2O_3 (**Figure 4.2a**), and 2.48 Å, which possibly corresponds to the [004] crystal of Ti_4O_7 (**Figure 4.2b**). A precise estimation on the crystal structure is, however, difficult to make due to the presence of some dislocations, as indicated by the red boxes in **Figure 4.2**.

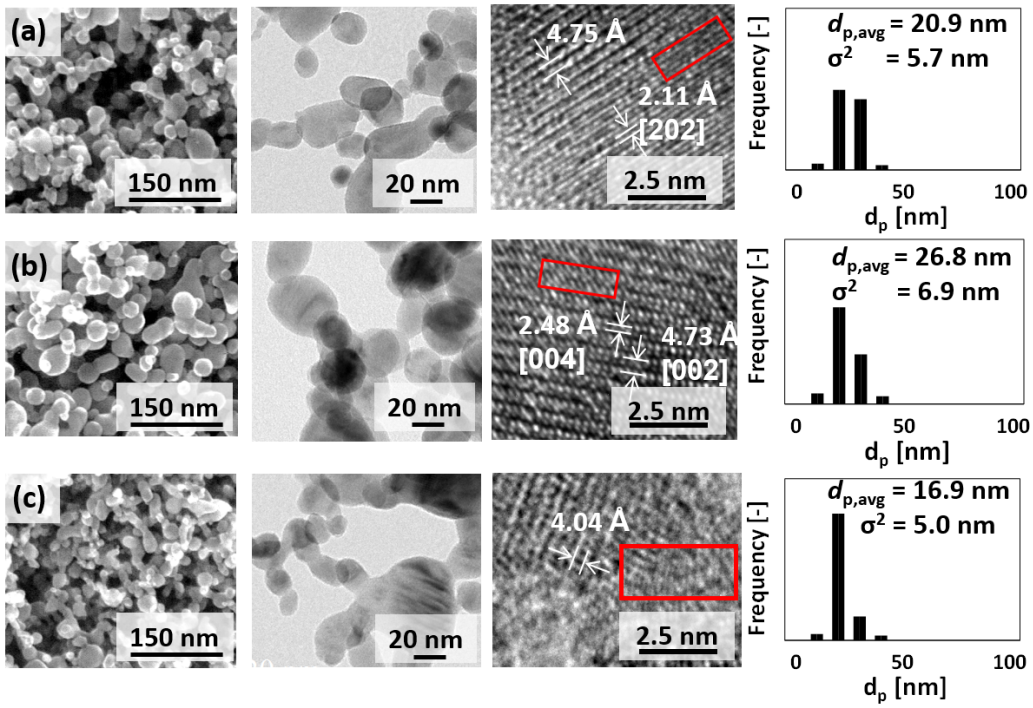

Figure 4.2. SEM and TEM images showing the chain structure and the lattice structure of the NPs, and particle size distribution of (a) TiO_x-A, (b) TiO_x-B, and (c) TiO_x-C. Red boxes in the TEM images indicate discontinuous lattices. Some lattice spaces can be associated with reduced titanium oxides, such as Ti_3O_5 [002] (4.73 Å), Ti_2O_3 [202] (2.11 Å), Ti_4O_7 [004] (2.48 Å)

Confirming the results of the HR-TEM analysis, the XRD spectra of the as-synthesized samples (**Figure 4.3**) show that TiO_x-A, TiO_x-B, and TiO_x-C were mixtures of several Magnéli phases and the other titanium-based species. TiO_x-A mainly consists of Ti_2O_3 and TiO_2, while TiO_x-B includes Ti_3O_5 and Ti_4O_7. In both TiO_x-A and TiO_x-B, some suboxides other than

Magnéli phases were present. Unlike the spectra of the other two samples, where sharp peaks with high intensities are observed, the spectrum of TiO_x-C shows broader peaks of lower intensity. This result agrees with the analysis of the HR-TEM images wherein TiO_x-C contained some amorphous phases. TiO_2, kleberite ($Ti_{0.374}O_{0.5}(OH)_{0.5}$), and $TiH_{0.5}$ are identified from the sharper peaks. The broad peak between 27° and 36° (**1**) is assigned to Ti_3O_5, Ti_4O_7, Ti_8O_{15}, and TiO_2 while **2** is assigned to Ti_3O_5 and TiO_2. Visually, the sample with a greater extent of reduction is indicated by particles that are darker in color.

The different extent of reduction likely corresponds to the content of IPA-derived carbon formed during the synthesis. Precursor of TiO_x-A contained more IPA than that the other precursors did, resulting in the formation of more carbon during the synthesis. Since carbon can reduce TiO_2, sample with the highest carbon content will have higher extent of reduction.

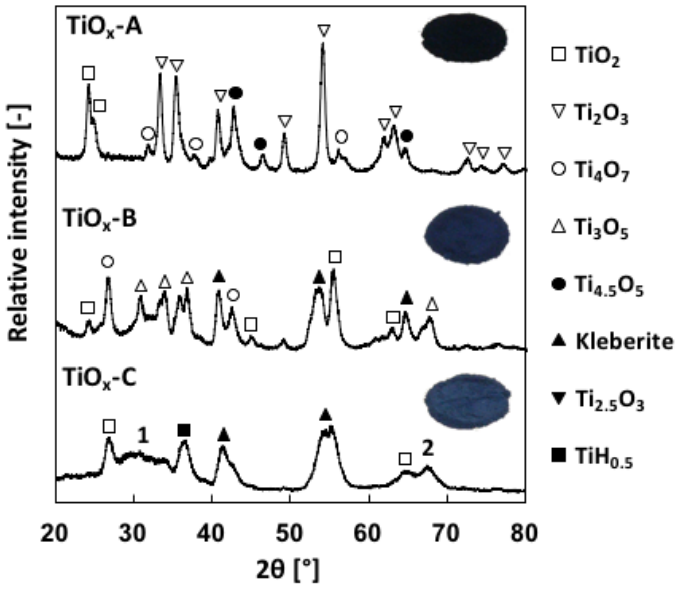

Figure 4.3. XRD spectra and the main peaks assignment of TiO_x-A, TiO_x-B, and TiO_x-C. TiO_x-A shows the greatest extent of reduction, indicated by the domination of the Ti_2O_3 phase. The broad peak indicated by **1** is assigned to Ti_3O_5, Ti_4O_7, Ti_8O_{15}, and TiO_2 while **2** is assigned to Ti_3O_5 and TiO_2. Samples with a greater extent of reduction tend to have darker colors. A complete list of the identified species is provided in the supporting information

Heat treatment conducted at 550 °C improved the quality of the lattice structure. Although the average particle diameters were slightly greater than those of the as-synthesized particles, **Figure 4.4** shows that they were within the margin of error. We can, therefore, say

that the heat treatment did not significantly change the particle size or the morphology. The BET surface areas of heat-treated samples were 52.9, 44.2, and 55.2 $m^2 g^{-1}$ for TiO_x-A, TiO_x-B, and TiO_x-C, respectively.

According to the HR-TEM images, the distances between the lattices of heat-treated NPs were uniform and the lattices were less discontinuous than the non-heat-treated particles. The clear lattice structure indicates increased crystallinity of the particles. Based on a randomized sampling of the HR-TEM images, some of the lattice distances were close to those associated for Ti_4O_7, especially for heat-treated TiO_x-A (2.8 Å for Ti_4O_7 [022]) and TiO_x-C (2.9 Å for Ti_4O_7 [112]).[18] The other identified lattice distances may be associated to Magnéli phases with higher oxygen content, such as Ti_8O_{15} [$10\bar{1}\bar{1}$]. We may, therefore, expect the presence of a new Ti_4O_7 phase and the neighbouring structure in the heat-treated samples. It is interesting that the crystal structure changed at a temperature lower than that usually needed. The presence of residual energies in the as-synthesized NPs due to the involvement of the high synthesis energy in RF thermal induction plasma likely decreased the amount of external energy required to change the crystal structure.

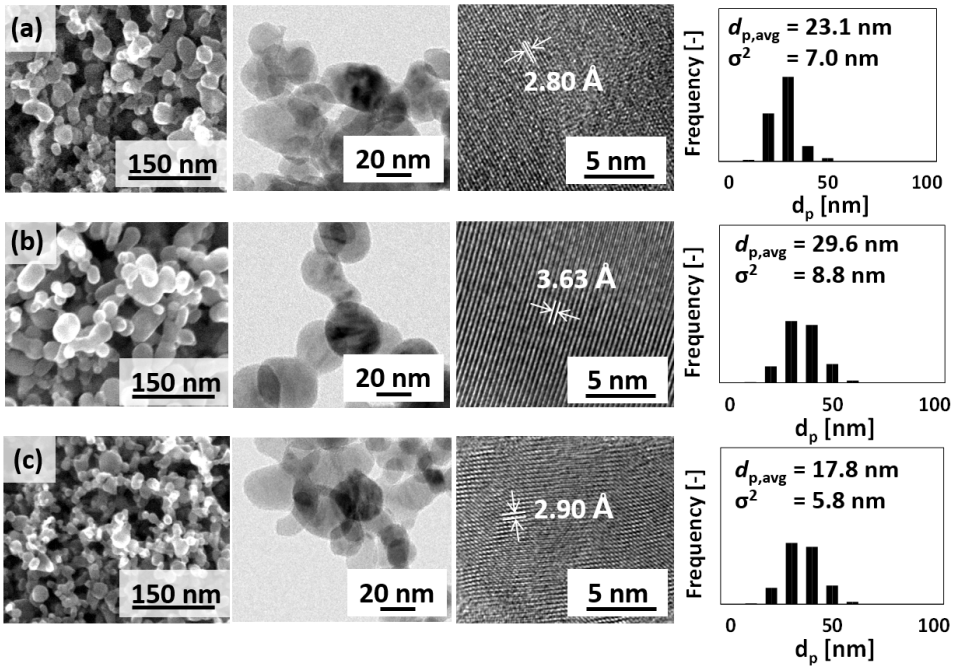

Figure 4.4. SEM, TEM images, and particle size distribution of heat-treated (a) TiO_x-A, (b) TiO_x-B, and (c) TiO_x-C. A clear lattice structure can be observed for the heat-treated samples, showing Ti_4O_7 [022] (2.8 Å), Ti_4O_7 [122] (2.9 Å), and higher oxidation states TiO_x (likely Ti_8O_{15} [$10\bar{1}\bar{1}$] for 3.63 Å).

XAFS analysis was performed to confirm the presence of the Magnéli phase. Fitting the XAFS spectra of as-synthesized and heat-treated samples resulted in the fractions of Ti^{3+} and Ti^{4+} before and after heat treatment, as shown in **Figure 4.6(a)**. The Ti^{4+} fraction in TiO_x-B and TiO_x-C decreased from 49.5% to 44.3% and 66.1% to 62.2%, respectively. In contrast, the Ti^{4+} fraction in TiO_x-A increased from 26.5% to 37.3% after heat-treatment. Although Ti^{3+} and Ti^{4+} may be associated with Ti_2O_3 and TiO_2, respectively, each fraction may not represent the actual concentration of Ti_2O_3 or TiO_2 because some of the Ti^{3+} and Ti^{4+} may partially form the Magnéli phase. It is clear that, among all of the samples studied in this work, TiO_x-A has the lowest total Ti^{4+} fraction which decreases the tendency to form TiO_2 phase.

Interestingly, the Ti^{4+} fraction in TiO_x-A increased after the heat treatment even though it was performed in a non-oxidizing environment. It is predicted that oxygen from the scission of the –OOC functional group on the particles surface was the source of this partial oxidation. The low-wavelength FT-IR spectrum of TiO_x-A confirms, after the heat treatment, a significant decrease in the Ti-O-OC broad peak at 1103 cm^{-1} (**Figure 4.5**). Elemental mapping of TiO_x-A before and after heat treatment also confirms a decreased intensity of carbon element on the particles surface

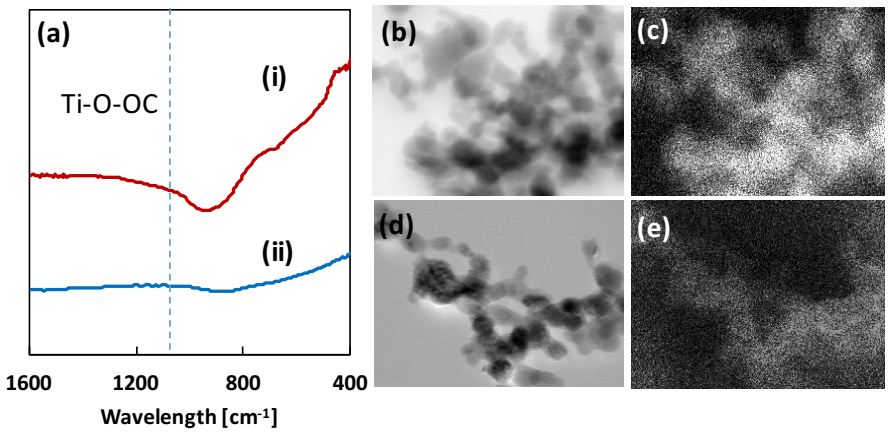

Figure 4.5. (a) FT-IR spectrum of (i) TiO_x-A and (ii) heat-treated TiO_x-A which show a significant decrease in the Ti-O-OC peak intensity at 1103 cm^{-1} after heat treatment. This result is aligned with TEM image and carbon elemental mapping of (b, c) TiO_x-A and (d, e) heat-treated TiO_x-A which show a reduction in the carbon intensity after heat treatment.

In an RF induced thermal plasma process, formation of carbides and other carbon functional groups is highly possible when IPA is present in the precursor. The formation of these groups can be suppressed by the addition of water. Because the precursor of TiO_x-A had

the lowest water content, it is speculated that TiO_x-A was enriched with carbon functional groups on the surface. However, further studies are required to confirm this hypothesis.

Aligned with the results from the TEM analysis, the XRD spectra given in **Figure 4.6(b)** to **(d)** show better crystallinity after heat treatment which eases the identification of the phases. Summary of the phases before and after heat-treatment is provided in **Table 4.1 to 4.3.** The phases that already exist in the as-synthesized TiO_x-A were preserved during heat-treatment with a notable increase in Ti_4O_7 peak intensity at 26.5° and 32°. On the contrary, a strong peak of Ti_4O_7 at 26.5° in TiO_x-B disappeared after heat-treatment. Some new phases such as Ti_8O_{15} and TiH_2 were developed instead. The formation of TiH_2 in TiO_x-B is strongly related to the presence of Ti in the as-synthesized particles, which furthermore reacted with H_2 in the reducing gas. In the heat-treated TiO_x-C, the broad peak between 27° and 36° almost vanished. At the same time, strong TiO_2 peaks appeared.

Table 4.1. Summary of identified phases in TiO_x-A from XRD analysis

Phase	PDF No.	As-synthesized	Heat-treated
TiO_2	04-011-0664	√	√
TiO_2	01-070-2556	√	√
Ti_2O_3	00-010-0063	√	√
$Ti_{2.5}O_3$	04-015-9125	-	√
$Ti_{4.5}O_5$	01-071-6414	√	√
Ti_4O_7	04-005-4521	√	√
Ti_2C	04-007-1462	√	√

Table 4.2. Summary of identified phases in TiO_x-B from XRD analysis

Phase	PDF No.	As-synthesized	Heat-treated
Ti_3O_5	04-008-8183	√	√
$Ti_{2.5}O_3$	04-015-9125	-	√
TiO_2 (rutile)	04-003-0648	√	√
TiO_2 (P3121)	01-070-2556	√	√
TiO_2 (srilankite)	00-021-1236	√	√
Ti	00-055-0345	√	√
Ti_4O_7	04-005-4521	√	-
$TiH_{0.5}$	01-079-6209	√	√
TiH_2	04-007-5214	-	√
Ti_8O_{15}	00-050-0790	-	√
$Ti_{0.374}O_{0.5}(OH)_{0.5}$ (kleberite)	01-076-5388	√	√

Table 4.3. Summary of identified phases in TiO_x-C from XRD analysis

Phase	PDF No.	As-synthesized	Heat-treated
Ti_3O_5	04-008-8183	√	√
$Ti_{4.5}O_5$	01-071-6414	√	√
TiO_2 (rutile)	04-003-0648	√	√
TiO_2 (P3121)	01-070-2556	√	√
TiO_2 (srilankite)	00-021-1236	√	√
Ti_2O_3	00-010-0063	√	√
Ti_4O_7	04-005-4521	√	√
$TiH_{0.5}$	01-079-6209	√	√
TiH_2	04-007-5214	-	√
Ti_8O_{15}	00-050-0790	√	-
TiC_8	00-051-0622	-	√
$Ti_{0.374}O_{0.5}(OH)_{0.5}$ (kleberite)	01-076-5388	√	√

Formation of phases with average intermediate Ti oxidation states (between 3+ and 4+), especially in heat-treated TiO_x-A, may be correlated to the concept of electrons being shared in the Magnéli phase. The average electronic charge of a Magnéli phase depends on the proportion of Ti^{3+} and Ti^{4+} that form the shear structure by sharing electrons. For example, Ti_4O_7 ($Ti^{3.5+}$) consists of two equally populated Ti^{3+} and Ti^{4+}, where the electrons in the *d* band are fully delocalized.[19] The formation of a Magnéli phase therefore suggests a rearrangement of Ti atoms due to the heat treatment. This rearrangement may have involved electron transfer between the *d* bands of the Ti atom and partial delocalization of some *d* electrons. The results show a tendency to preserve and/or to form intermediate phases, especially Ti_4O_7, when both TiO_2 and Ti_2O_3 were present in the as-synthesized particles. The initiator for the electron excitations is predicted to be the photon energy from heat radiation. Delocalization of some electrons would, furthermore, affect the electron conductivity.

Table 4.4 compares the electrical resistivity of the sample before and after heat-treatment, measured using the 4-probe method. The resistivity values of the as-synthesized samples are very high, although some conductive Magnéli phases are identified from XRD. One of the reasons for the high resistivity of the as-synthesized powder may be the random lattice structure and the presence of the amorphous phase. It is speculated that the discontinuities in the lattice structure may have inhibited the electron mobility. According to the empirical formula developed by Goodenough, the critical Ti to Ti interatomic distance that

determines whether the *d* electrons are collective or localized is 3.01 Å.[20] Above this value, the *d* electrons are localized, indicating a semiconductor state. Therefore, the presence of some lattices with spaces of about 4 Å, as observed in **Figure 4.2**, may indicate that the metal-like phase is interrupted with the presence of semiconducting phases. Due to this phase discontinuity, the resistivity values of the as-synthesized samples were close to the resistivity of known semiconductors.

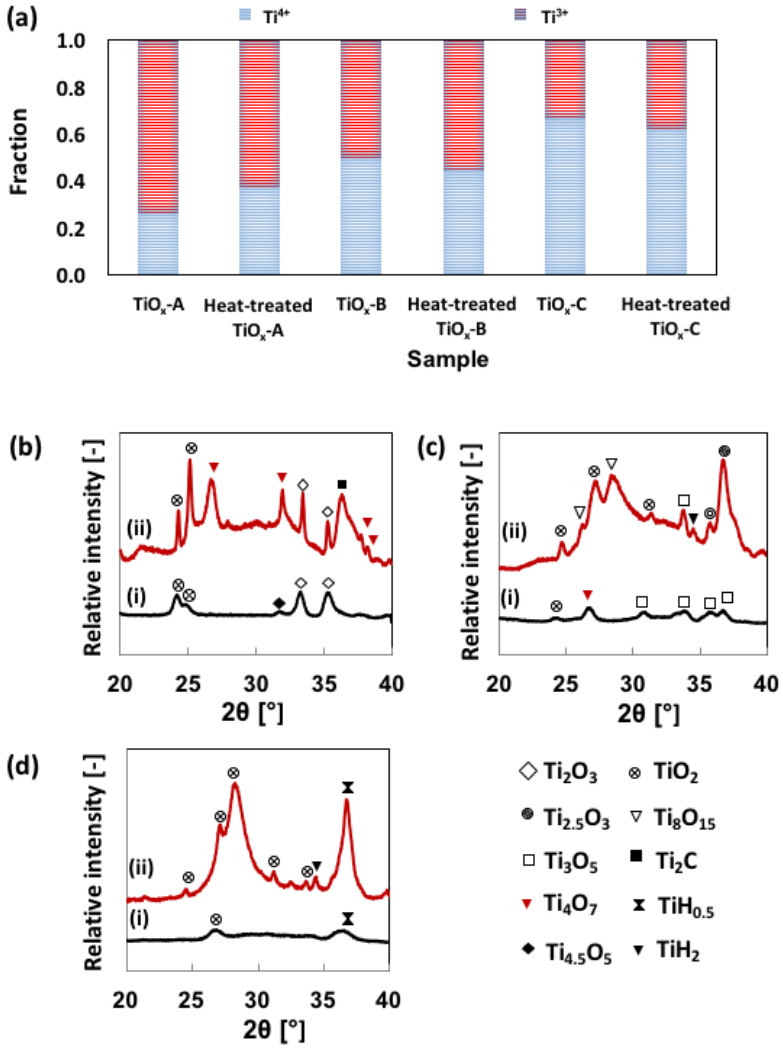

Figure 4.6. (a) Fraction of Ti^{3+} and Ti^{4+} in the samples based on XAFS analysis. The Magnéli phase composition of each sample was determined based on the XRD spectra of (b) TiO_x-A, (c) TiO_x-B, and (d) TiO_x-C. (i) is the spectra of as-synthesized nanoparticles and (ii) is the spectra of heat-treated nanoparticles.

Table 4.4. Electrical resistivity of the samples before and after heat-treatment. The electrical resistivity of the samples significantly decreased after heat treatment. TiO_x-A has the highest electrical conductivity

Sample	Electrical resistivity (Ω.cm)	
	As-synthesized	**Heat-treated**
TiO_x-A	$1.48 \times 10^4 \pm 150$	0.04 ± 0.008
TiO_x-B	$3.91 \times 10^6 \pm 26458$	0.21 ± 0.043
TiO_x-C	$3.65 \times 10^5 \pm 1528$	0.75 ± 0.125

Another possible explanation for the high resistivity of the as-synthesized powder is the presence of insulating surface functional groups that increase the contact resistance between particles. An ideal structure of Ti-O on the surface is commonly difficult to realize because the surface of titanium oxide is easily covered by hydroxyl groups that combine with titanium ions.[21] The source of the OH group is likely the water vapour in the air, which made a contact with the particles during the particles evacuation from the particle collector post-synthesis. Plasma-synthesized particles often contain neither oxides nor hydroxides, provided they are confined in the reactor.[22]

The resistivity values after the heat-treatment significantly decreased. This is believed to be the result of several factors. The first is that the presence of Magnéli phases with Ti valences between +3.3 and +3.7. Formation of Magnéli phase enabled partial to complete delocalization of *d* electrons. The presence of Ti_4O_7, in which *d* electrons are fully delocalized, is believed to contribute to the high electrical conductivity. As previously summarized in **Table 4.1**, TiO_x-A and TiO_x-C preserved their Ti_4O_7 phase with increasing Ti_4O_7 peak intensity for TiO_x-A. It is therefore understandable that heat-treated TiO_x-A had the lowest resistivity among the heat-treated samples. Meanwhile, the increasing semiconducting phases, *i.e.* TiO_2 and Ti_2O_3, resulted in the high resistivity of heat-treated TiO_x-C compared to the other heat-treated samples, although Ti_4O_7 was still present in the heat-treated TiO_x-C. In contrast with the other two samples, TiO_x-B lost its Ti_4O_7 phase after heat-treatment. Kleberite which is insulating was still present after heat-treatment. However, slightly more resistive phases such as Ti_3O_5 and Ti_8O_{15} which were still present helped improving the conductivity. Titanium

hydride formed after heat-treatment of TiO_x-B and TiO_x-C were also expected to lower the electrical resistivity.[23]

In addition to the presence of a conducting crystal structure, the significant reduction in the electrical resistivity of the heat-treated samples is likely the result of a lower contact resistance between particles. As confirmed by the FT-IR analysis in **Figure 4.5 (a)**, the intensity at around 900 cm^{-1} in the spectrum from insulating aromatic hydrocarbons[24] of heat-treated samples was lower than that in the as-synthesized sample.

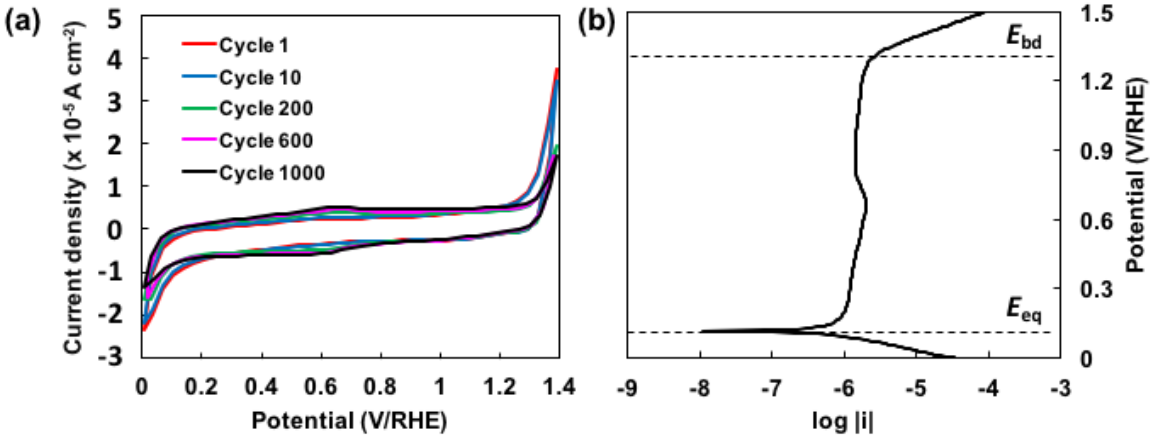

Figure 4.7. (a) Cyclic voltammogram of heat-treated TiO_x-A in oxygen-saturated HCl 1 M solution between 0 and 1.4 V/RHE at a potential sweep of 50 mV/s. The voltammogram shape did not significantly change after 1000 cycles, especially in the pseudocapacitive region. (b) Potentiodynamic curve of heat-treated TiO_x-A in oxygen-saturated HCl 1 M solution between 0 and 1.5 V/RHE. The curve shows a tendency of TiO_x-A to passivate with a high break-down potential.

Figure 4.7(a) shows multiple-cycle cyclic voltammogram of heat-treated TiO_x-A as the representative sample. The cyclic voltammograms show no visible cathodic nor anodic peak within 0 and 1.4 V/RHE which implies that the heat-treated TiO_x-A was relatively inert in a strongly oxidizing environment. The overall shape of the voltammogram was preserved after 1000 cycles, indicating the stability of heat-treated TiO_x-A in a strongly oxidizing environment. TiO_x-A possesses much better stability over potential cycling than Ti_4O_7. Insignificant anodic and cathodic peak at 0.56 V/RHE and 0.66 V/RHE, respectively, appeared after 200 cycles. The precise assignment of these peaks will be a subject for further studies. However, it is predicted that these peaks correspond to the electrochemical reduction of TiO_2

phase which possibly happens between 0.52 to 0.84 V/standard hydrogen electrodes (SHE).[25] It is also worth noting that the voltammogram shape is close to square, indicating a double layer charge storage mechanism. Through further functionalization, it is therefore possible to use these nanoparticles as energy storage materials.

The electrochemical stability of heat-treated TiO_x-A is confirmed by the potentiodynamic curve shown in **Figure 4.7(b)**. The equilibrium potential, E_{eq}, was 0.11 V/RHE, indicated by a substantial decrease of the current density as a response to a small potential elevation. The low E_{eq} would imply that the heat-treated TiO_x-A is easily oxidized under oxygen-rich environment. However, Tafel extrapolation on the anodic curve at 60 mV above E_{eq} shows a very low exchange current density, 5.37 x 10^{-7} A cm^{-2}, which corresponds to a thinning rate of 0.006 mm per year in a continuous exposure to a strongly oxidizing environment. This value is very low that TiO_x-A can be considered as corrosion-resistant material. The corrosion resistivity is attributed to the passivity of heat-treated TiO_x-A, indicated by a relatively stable current density above 0.2 V/RHE. The break down potential, $E_{bd,}$ of the passivity was approximately 1.3 V/RHE, slightly lower than 1.4 V/RHE. However, since the cyclic voltammograms of TiO_x-A show a stable performance within 0 to 1.4 V/RHE up to 1000 cycles, heat-treated TiO_x must have had the ability to re-passivate during the backward potential sweep.

4.4 Conclusions

In summary, this study demonstrated the synthesis of Magnéli phases titanium oxide NPs *via* an RF induction thermal plasma method. Nanoparticles with low electrical resistivity were successfully obtained after applying a post-synthesis heat treatment to the as-synthesized NPs. In particular, this study found an interesting phenomenon in the formation of new crystal structures after the heat treatment and suggested mechanisms for the crystal structure changes based on the evidence from XAFS and XRD analyses. The resistivity values of the heat-treated samples were related with the Magnéli phase content, especially Ti_4O_7, estimated from the XRD spectra. Further investigation of this phenomenon is encouraged for a better understanding of the solid-state transformation of Magnéli phase titanium oxide. The electrochemical characterization shows a remarkable stability of the heat-treated TiO_x-A NPs in a strongly oxidizing environment, which opens a wider opportunity for the application of plasma-synthesized TiO_x NPs.

4.5 References

[1] Andersson, S., et al., *Phase analysis studies on the titanium-oxygen system.* Acta Chemica Scandinavica, 1957. **11**(10): p. 1641-1652.

[2] Bartholomew, R.F. and D. Frankl, *Electrical properties of some titanium oxides.* Physical review, 1969. **187**(3): p. 828.

[3] Harada, S., K. Tanaka, and H. Inui, *Thermoelectric properties and crystallographic shear structures in titanium oxides of the Magneli phases.* Journal of applied physics, 2010. **108**(8): p. 083703.

[4] Smith, J., F. Walsh, and R. Clarke, *Electrodes based on Magnéli phase titanium oxides: the properties and applications of Ebonex® materials.* Journal of applied electrochemistry, 1998. **28**(10): p. 1021-1033.

[5] Ioroi, T., et al., *Stability of corrosion-resistant Magnéli-phase Ti4O7-supported PEMFC catalysts at high potentials.* Journal of the Electrochemical Society, 2008. **155**(4): p. B321-B326.

[6] Zhu, R., et al., *Magnéli phase Ti4O7 powder from carbothermal reduction method: formation, conductivity and optical properties.* Journal of Materials Science: Materials in Electronics, 2013. **24**(12): p. 4853-4856.

[7] Ye, J., et al., *Temperature effect on electrochemical properties of Ti4O7 electrodes prepared by spark plasma sintering.* Journal of Materials Science: Materials in Electronics, 2015. **26**(7): p. 4683-4690.

[8] Kitada, A., et al., *Selective Preparation of Macroporous Monoliths of Conductive Titanium Oxides Ti n O2 n–1 (n= 2, 3, 4, 6).* Journal of the American Chemical Society, 2012. **134**(26): p. 10894-10898.

[9] Tang, C., et al., *Effects of Ti4O7 on Secondary Alkaline Zinc Anode.* Journal of The Electrochemical Society, 2012. **159**(11): p. A1796-A1800.

[10] Krishnan, P., S.G. Advani, and A.K. Prasad, *Magneli phase Ti n O2n− 1 as corrosion-resistant PEM fuel cell catalyst support.* Journal of Solid State Electrochemistry, 2012. **16**(7): p. 2515-2521.

[11] Walsh, F. and R. Wills, *The continuing development of Magnéli phase titanium sub-oxides and Ebonex® electrodes.* Electrochimica Acta, 2010. **55**(22): p. 6342-6351.

[12] Chao, S., V. Petrovsky, and F. Dogan, *Effects of sintering temperature on the microstructure and dielectric properties of titanium dioxide ceramics.* Journal of materials science, 2010. **45**(24): p. 6685-6693.

[13] Ioroi, T., et al., *Formation of electro-conductive titanium oxide fine particles by pulsed UV laser irradiation.* Physical Chemistry Chemical Physics, 2010. **12**(27): p. 7529-7535.

[14] Portehault, D., et al., *Facile general route toward tunable magnéli nanostructures and their use as thermoelectric metal oxide/carbon nanocomposites.* ACS nano, 2011. **5**(11): p. 9052-9061.

[15] Ogi, T., et al., *Facile synthesis of single-phase spherical α "-Fe16N2/Al2O3 core-shell nanoparticles via a gas-phase method.* Journal of applied physics, 2013. **113**(16): p. 164301.

[16] Nakamura, K., *Synthesis of nanoparticles by RF induction thermal plasma*, in *Nanoparticle technology handbook*, M. Hosokawa, Nogi K., Naito M., Yokoyama T., Editor. 2012, Elsevier: Oxford. p. 612-618.

[17] Swihart, M.T., *Vapor-phase synthesis of nanoparticles.* Current Opinion in Colloid & Interface Science, 2003. **8**(1): p. 127-133.

[18] Liborio, L., G. Mallia, and N. Harrison, *Electronic structure of the Ti 4 O 7 Magnéli phase.* Physical Review B, 2009. **79**(24): p. 245133.

[19] Abbate, M., et al., *Changes in the electronic structure of Ti 4 O 7 across the semiconductor–semiconductor-metal transitions.* Physical Review B, 1995. **51**(15): p. 10150.

[20] Goodenough, J.B., *Characterization of d electrons in solids by structure I. Localized vs collective electrons.* Materials Research Bulletin, 1967. **2**(1): p. 37-48.

[21] Iwaki, T., *Studies of the Surface of Rutile Single Crystals by Means of Electrical Conductivity.* Bulletin of the Chemical Society of Japan, 1973. **46**(6): p. 1631-1638.

[22] Zulhijah, R., et al., *α"-Fe16N2 phase formation of plasma-synthesized core–shell type α-Fe nanoparticles under various conditions.* Advanced Powder Technology, 2014. **25**(2): p. 582-590.

[23] Ito, M., et al., *Electrical and thermal properties of titanium hydrides.* Journal of Alloys and Compounds, 2006. **420**(1–2): p. 25-28.

[24] Margoshes, M. and V. Fassel, *The infrared spectra of aromatic compounds: I. The out-of-plane CH bending vibrations in the region 625–900 cm− 1.* Spectrochimica Acta, 1955. **7**: p. 14-24.

[25] Katayama, Y., B. Friedrich, and M. Recycling. *Electrochemical Reduction of Titanium Dioxide Thin Film in LiCl-KCl-CaCl2 Eutectic Melt*. in *PROCEEDINGS-ELECTROCHEMICAL SOCIETY PV*. 2004.

Chapter 5

Summary and Conclusions

Carbon is widely used as an essential part of the electrodes in fuel cells and supercapacitors. It is therefore understandable that engineering the carbon particles is a good approach to improve the performance of fuel cells and supercapacitors. This dissertation encompasses nanostructuration and functionalization of carbon particles as a part of engineering the carbon, and demonstrates the synthesis of a feasible carbon substitute material. Highlights of this dissertation comprises the following points.

1. Morphological structure of carbon catalyst support is tailored using spray pyrolysis method involving polystyrene latex template and phenolic resin as carbon precursor. Most importantly, effects of the carbon particles' morphological structure on the oxygen reduction reaction (ORR) are evaluated following the deposition of platinum nanoparticles. Electrocatalyst with porous carbon support exhibits the highest ORR activity. This study finds that specific surface area is not the only factor affecting the electrocatalyst's performance. A good hydrodynamic profile inside the electrocatalyst layer facilitated by a combination between macro- and mesopores is a critical aspect that should be carefully considered for the optimum ORR activity.
2. As a further development of mesoporous carbon for charge storage devices, synthesis of hollow-structured carbon particles with micro- and mesoporous shell structure using microwave irradiation and a subsequent carbonization is demonstrated. These are nitrogen-functionalized carbon with a nitrogen content up to 15.62%. The combination between nitrogen doping and hollow structure delivers the improvement on the charge storage ability by 17.3%.
3. In response to the carbon corrosion problem, Magneli phases TiO_x is introduced as electrically conductive, stable, and corrosion-resistant material. Synthesis of Magneli phases TiO_x nanoparticles is done by thermal-induced plasma process. After a post-synthesis heat-treatment at 550 °C in 3% hydrogen atmosphere, the nanoparticles exhibit the electrical resistivity values of 0.04 Ω cm^{-1} and a corrosion resistance in oxygen-saturated hydrochloric acid.

Based on these highlights, it is clear that particles with controlled morphological structure and heteroatom doping are indispensable towards high performance fuel cells and

supercapacitors. Moreover, materials selection is another essential factor that cannot be neglected towards highly durable devices and Magneli phases TiO_x demonstrates their potential for this concern. Based on this standpoint, suggestions for the future research include nanostructuration and functionalization of Magneli phases TiO_x.

Acknowledgement

Praise the God almighty for His merciful blessings.

I would like to thank Assoc. Prof. Takashi Ogi for being my supervisor. I also feel grateful for being one of a few students who had the opportunity to work with Prof. Kikuo Okuyama (emeritus), a big name in the world of aerosol research.

A special gratitude to my Ph.D. referees: Prof. Toshinori Tsuru, Prof. Takeshi Shiono, and Prof. Akihiro Yabuki for the constructive critics, suggestions, and insights.

A special appreciation to Prof. Sotiris Pratsinis from ETH Zurich and his group for the rare opportunity to introduce and discuss my research in ETH Zurich. That will definitely be one of my unforgettable experiences. I would also thank Prof. Wendelin Stark from ETH Zurich for his suggestions on my research.

I thank Dr. Hary Devianto, Dr. Isdiriayani Nurdin, and Dr. Ferry Iskandar from Institut Teknologi Bandung for their continuous supports, even long before the commencement of my Ph.D.

A special mention to the Ministry of Education, Culture, Sports, Science, and Technology of Japan for the Ph.D. scholarship and to Hosokawa Micron Powder Foundation for the research fund.

My Indonesian friends: Ghana, Christina, Fitri, Dr. Osi, and Dr. Rizka. My Ph.D. life would have been different without you, guys.

Last but not least, this doctoral degree is dedicated to my father and mother Anton Suhartono and Siti Farida, and my sister Alifia. This dream-chasing journey has taken me to places I have never reached, opened the doors into other worlds and windows into myself.

ADITYA FARHAN ARIF

Higashi-hiroshima, September 2017